GRAPHENE/ZINC OXIDE NANOCOMPOSITE: A VERSATILE PLATFORM FOR ELECTROCHEMICAL-BASED GENOSENSOR

LOW SZE SHIN, BSc (Hons).

Thesis submitted to the University of Nottingham

For the degree of Doctor of Philosophy

2017

Abstract

In this work, a versatile electrochemical biosensing platform was developed based on graphene/zinc oxide (G/ZnO) nanocomposite. For the synthesis of G/ZnO nanocomposite, two facile and green approaches were employed to eradicate the issues associated with conventional methods, which use harsh chemicals and high temperature. The G/ZnO nanocomposite synthesised via low temperature hydrothermal growth method exhibited approximate 58 times improvement in terms of sensitivity as compared to the G/ZnO nanocomposite synthesised via the mechanical stirring method. Therefore, the G/ZnO nanocomposite with higher sensitivity was employed for the following work.

Results from cyclic voltammetry and amperometry showed that the G/ZnO-modified electrode displayed a wide linear range up to 15 mM for the detection of H_2O_2 and sensitivity improvements of 200% in comparison to the control sample. Subsequently, an electrochemical genosensor based on G/ZnO nanocomposite was fabricated for the detection of Avian Influenza H5N1 virus. The G/ZnO-based genosensor displayed its potential in replacing the conventional detection method, with result showing higher sensitivity and efficiency. The G/ZnO-based genosensor was further applied for the detection of Coconut Cadang-Cadang Viroid disease (CCCVd) single stranded RNA (ssRNA). Promising results were obtained with high specificity in discriminating the target from mismatched ssRNA sequences.

Publications – Journal

1. **Sze Shin Low**, Hwei-San Loh, Jian Sheng Boey, Poi Sim Khiew, Wee Siong Chiu, Michelle T. T. Tan, *'Sensitivity Enhancement of Graphene/Zinc Oxide Nanocomposite-based Electrochemical Impedance Genosensor for Single Stranded RNA Detection'*, Biosensors and Bioelectronics, 2017 (in press) (IF: 7.476)

2. **Sze Shin Low**, Michelle T. T. Tan, Hwei-San Loh, Poi Sim Khiew, Wee Siong Chiu, *'Facile hydrothermal growth graphene/ZnO nanocomposite for development of enhanced biosensor'*, Analytica Chimica Acta, Vol. 903, pg. 131 – 141, 2016 (IF: 4.712)

3. **Sze Shin Low**, Joanna Su Yuin Chia, Michelle T. T. Tan, Hwei-San Loh, Poi Sim Khiew, Ajit Singh, Wee Siong Chiu, *'A Proof of Concept: Detection of Avian Influenza H5 Gene by a Graphene-Enhanced Electrochemical Genosensor'*, Journal of Nanoscience and Nanotechnology, Vol. 16, pg. 2438 - 2446, 2016 (IF: 1.338)

4. **Sze Shin Low**, Michelle T. T. Tan, Poi Sim Khiew, Hwei-San Loh, Wee Siong Chiu, *'One Step Green Preparation of Graphene/ZnO Nanocomposite for Electrochemical Sensing'*, Journal of Nanoscience and Nanotechnology, Vol. 16, pg. 1 – 7, 2016 (IF: 1.338)

5. **Sze Shin Low**, Michelle T. T. Tan, Poi Sim Khiew, Hwei-San Loh, Wee Siong Chiu, *'One-Step Green Synthesis of Graphene/ZnO Nanocomposites for Non-Enzymatic Hydrogen Peroxide Sensing'*, Materials and technology, Vol. 49, pg. 837 – 840, 2015 (IF: 0.439)

Conference Participation

- ✓ International Conference on Advanced Materials and Nanotechnology (ICAMN 2016) – **Best Presenter Award**

Acknowledgements

I would like to express my gratitude towards many individuals. Without their help, advice and support, this thesis would not be completed successfully.

Firstly, I would like to thank my supervisors, Dr. Michelle Tan Tien Tien, Prof. Khiew Poi Sim and Prof. Sandy Loh Hwei San, whose guidance, advice and technical expertise provided the foundation of this thesis. Thank you for all the support throughout these years.

I would also like to thank my family, Wai Siong and Nasi Lemak group (Carmen, Ee Leen, Ivan and Wei Keat) for their continuous support and patience during my postgraduate study. Thanks to them who always take me out for good meals, cheer me up and help me to release stress. It means a lot to me for them to be able to understand my situation.

Special thanks to the technical staffs, Mr Andrew, Mr Faizal, Mr Fareez, Mr Jonathan and others for the assistance in various laboratory works. A special mention of thanks too, to Professor Dino Isa for his generous access to equipment in the Shaz Lab.

Last but not least, I thank my fellow office mates – Soon Yee, Yoong Kit, Milor, Adam, June, Jesslyn, Patrick and Maggie for being there throughout this journey, especially Milor who had given me a lot of useful advices.

To all the other individuals whom I forgot to mention, thanks a lot.

Table of Contents

List of Figures

amplicon (mean ± SD (n=3)), error bars were plotted according to the SD of each triplicate, different letters indicate differences among dilution factors as determined by Fisher's protected least significant different (LSD) test at P = 0.05. (B) Plot of current signals against different dilution factors of $H5$ PCR amplicon. 139

List of Tables

Nomenclature

Acronyms

AA	Ascorbic Acid
AC	Alternating Current
AE	Auxiliary Electrode
Ag	Silver
Ag/AgCl	Silver/Silver Chloride Electrode
ANOVA	Analysis of Variance
Au	Gold
BSA	Bovine Serum Albumin
BSEs	Backscattered Electrons
C	Carbon
CCCVd	Coconut Cadang-Cadang Viroid Disease
CCD	Charge Coupled Device
CE	Counter Electrode
CG	Chitosan-Functionalised Graphene
Co_3O_4	Cobalt Oxide
CPE	Constant Phase Element
CRD	Completely Randomised Design
CRT	Cathode Ray Tube
CuO	Copper Oxide
CV	Cyclic Voltammetry
DA	Dopamine
DCA	Direct Current Amperometry
DI	Deionised
DNA	Deoxyribonucleic Acid

dNTPs	Deoxynucleotides
DPV	Differential Pulse Voltammetry
dsDNA	Double Stranded DNA
EDC	1-Ethyl-3-(3-Dimethyl-Aminopropyl) Carbodiimide Hydrochloride
EDS	Energy Dispersive X-ray Spectroscopy
EIS	Electrochemical Impedance Spectroscopy
ELISA	Enzyme-linked Immunosorbent Assay
E_p	Anodic Peak Potential
E_p'	Cathodic Peak Potential
$E_{p1/2}$	Half Peak Potential
ET	Everhart-Thornley
Fe_2O_3	Iron (II) Oxide
Fe_3O_4	Iron (III) Oxide
Fe^{3+}/Fe^{2+}	Iron Ion
$Fe(NO_3)_3 \cdot 9H_2O$	Iron (III) Nitrate
GCE	Glassy Carbon Electrode
GO	Graphene Oxide
GOx / GOD	Glucose Oxidase
GS-SnO$_2$-PAN	Polyaniline Functionalised Graphene/SnO$_2$ Composite
G/ZnO	Graphene/Zinc Oxide
HA	Haemagglutinin
Hb	Haemoglobin
HIgG	Human Immunoglobulin G
HPAI	Highly Pathogenic Avian Influenza

HRP	Horse Radish Peroxidase
HRTEM	High Resolution Transmission Electron Microscopy
HSP	Hansen Solubility Parameter
H_2O_2	Hydrogen Peroxide
i / I_{pa}	Anodic peak current
i' / I_{pc}	Cathodic peak current
ICSD	Inorganic Crystal Structure Database
IPA	Intermittent Pulse Amperometry
ISO	International Organization for Standardization
IUPAC	International Union of Pure and Applied Chemistry
KBH_4	Potassium Borohydride
KCl	Potassium Chloride
$KMnO_4$	Potassium Permanganate
$K_3[Fe(CN)_6]$	Potassium Ferricyanide
LOD	Limit of Detection
LSD	Fisher's Protected Lease Significant Difference
M_{ox}	Oxidised Mediator
M_{red}	Reduced Mediator
MB	Methylene Blue
MBCPE	Magnetic Bar Carbon Paste Electrode
MC	Mitomycin-C
MCA	Multi-Channel Analyser
$MgCl_2$	Magnesium Chloride
MnO_2	Manganese Dioxide
Mn_3O_4	Manganese (III) Oxide
msRNA1	Single-base Mismatched ssRNA Strand

msRNA2	Double-base Mismatched ssRNA Strand
MW	Microwave
NA	Neuraminidase
$NaBH_4$	Sodium Borohydride
NaCl	Sodium Chloride
NaH_2PO_4	Monosodium Phosphate
Na_2HPO_4	Disodium Phosphate
NaOH	Sodium Hydroxide
NCBI	National Center for Biotechnology Information
NHS	*N*-hydroxysuccinimide
NiO	Nickel Oxide
ntRNA	Non-target ssRNA Strand
O	Oxygen
OCP	Open Circuit Potential
OH^-	Hydroxide
PAGE	Polyacrylamide Gel Electrophoresis
PBS	Phosphate Buffer Saline
PBST	Phosphate Buffered Saline Tween-20
PCR	Polymerase Chain Reaction
PDDA	Poly(diallydimethylammonium chloride)
PGE	Pencil Graphite Electrode
PSE / PANHS	1-Pyrenebutyric Acid-*N*-Hydroxysuccinimide Ester
PXa	Poly-xanthurenic acid
RE	Reference Electrode
rGO	Reduced Graphene Oxide
RNA	Ribonucleic Acid

ROS	Reactive Oxygen Species
RPA	Ribonuclease Protection Assay
RT-PCR	Reverse-Transcription Polymerase Chain Reaction
SA	Streptavidin
SCE	Saturated Calomel Electrode
SD	Standard Deviation
SDS	Sodium Dodecyl Sulphates
SEM	Scanning Electron Microscopy
SEs	Secondary Electrons
Si	Silicon
Si(Li)	Silicon Lithium
$SnCl_4$	Tin (IV) Chloride
SnO_2	Tin Dioxide
SPCE	Screen-printed Carbon Electrode
SPR	Surface Plasmon Resonance
SSC	Saline Sodium Citrate
ssDNA	Single-stranded DNA
ssRNA	Single-stranded RNA
TEM	Transmission Electron Microscopy
TiO_2	Titanium Dioxide
TMB	3,3',5,5'-Tetramethylbenzidine
Trp	Tryptophan
UA	Uric Acid
UV	Ultraviolet
V_1	Predetermined Switching Potential
V_2	Initial Potential

WE	Working Electrode	
XRD	X-ray Diffractometry	
$Z_{im}(\omega)$	Imaginary Component	
$Z_{re}(\omega)$	Real Component	
Zn	Zinc	
$Zn(NO_3)_2 \cdot 6H_2O$	Zinc Hexahydrate	
ZnO	Zinc Oxide	
$Zn(OH)_2$	Zinc Hydroxide	
Zn^{2+}	Zinc Ion	
2D	Two Dimensional	
3D	Three Dimensional	

Symbols

E	Potential	V
R	Gas Constant	$Jmol^{-1}K^{-1}$
T	Absolute Temperature	K
F	Faraday constant	$sAmol^{-1}$
n	Number of Exchanged Electrons / electron stoichiometry	-
i_p	Peak current	A
D	diffusion coefficient	cm^2s^{-1}
A	electrode area	cm^2
C	concentration	$molcm^{-3}$
v	scan rate	Vs^{-1}
Z	impedance	Ω
V	voltage	V

I	current	A
j	imaginary component	-
ω	frequency	rads^{-1}
f	Excitation frequency	Hz
R_s	ohmic resistance of the electrolyte solution	Ω
Z_w	Warburg impedance	Ω
C_d	double layer capacitance	F
R_{ct}	electron transfer resistance	Ω
n (Section 3.2.8)	order of reflection	-
λ	wavelength of the X-rays	nm
d	characteristic interplanar spacing	Å
θ	diffraction angle	°
ΔEp	Peak to peak separation	V
N	mol quantity of Methylene Blue	mol
Q	electric charge quantity	C
e	electric charge quantity of one electron	C
NA	Avogadro's number	mol

Chapter 1 Introduction

1.1 Introduction

Early and accurate diagnosis of chronic and life-threatening diseases such as cancer, human immunodeficiency virus (HIV), Diabetes Mellitus and more, at easily-treatable and pre-symptomatic stage, is crucial to forestall crisis condition, improving the survival rate of patients. Most existing diagnostic techniques are inefficient and insensitive, or are only able to identify the disease with the presence of symptoms, in which mostly are in the deadly stages. For example, the current gold standard diagnostic method for necrotizing enterocolitis is X-ray, which has a true positive rate of only 44%, culminating in high mortality rate due to the inability to achieve early and accurate diagnosis [1]. Furthermore, current molecular diagnosis methods rely on well-resourced laboratories, which are very expensive, time-consuming and require skilled personnel (eg. Enzyme-linked immunosorbent assay, ELISA). Besides, some of the current methods such as radioimmunoassay or isotopic labelling, involved the usage of radioactive labels which has potential deleterious biological effects, posing as a safety issue. Therefore, highly sensitive and selective techniques that are able to diagnose diseases at early stages are urgently needed.

A biosensor is a self-contained integrated device which is capable of providing specific quantitative analytical information using a biological recognition element which is retained in direct spatial contact with a transducer element, converting the biological recognition event into a useable

output signal [2]. The first successful presentation of biosensor was performed by Professor Leland C. Clark Jr. in 1962 at a New York Academy of Sciences symposium [3]. The concept of biosensor has intrigued numerous research studies by the scientific communities worldwide as biosensor is able to produce highly accurate, specific and real time signals. The key to success for a biosensor is sensitivity and selectivity, detecting only a specific target at an ultra low level and to maintain this selectivity in the presence of other species.

With remarkable achievements in nanotechnology, nanomaterial-based signal amplifications have great potential of improving both sensitivity and selectivity for biosensors. According to the National Nanotechnology Initiative (NNI), nanotechology is defined as study and technology development at the atomic, molecular, or macromolecular scale, leading to the controlled creation and use of structures, devices and systems with a length scale of 1 to 100 nm. Specifically, nanomaterials offer tenability in terms of performance, solution processability and processing temperature requirements, which makes them very attractive as building blocks for flexible electronic systems. In the fabrication of biosensors, it is well-known that the electrode materials play a critical role in constructing high performance sensing platforms. Moreover, hybridisation among nanomaterials can produce synergic effect among catalytic activity, conductivity and biocompatibility to accelerate the signal transduction, resulting in rapid detection of target. Also, nanomaterials can amplify biorecognition events with specifically designed

sensing system, leading to the development of highly selective biosensing technology.

Over the last decade, great attention has been paid to the inclusion of newly developed nanomaterials such as nanowires, nanotubes, and nanocrystals in sensor devices. The intelligent use of nanomaterials led to clearly enhanced performances with increased sensitivities and lowered detection limits of several orders of magnitudes [4]. In particular, graphene, the two dimensional (2D) material in the carbon family has stimulated much interest since its discovery by Geim via mechanical exfoliation in 2004 [5]. Owing to its intriguing properties such as high mobility of charge carriers, unique transport performance, theoretically high surface area and more, graphene is adaptable to a wide variety of applications, such as supercapacitors [6], biosensors [7], catalysis [8], nanocomposites and hydrogen storage [9]. On the other hand, zinc oxide (ZnO) is an imperative wide band gap semiconductor material with fast redox kinetics. However, ZnO possesses poor conductivity, low mechanical and chemical stability [10]. Therefore, the hybridisation of graphene with ZnO nanoparticles is anticipated to produce synergistic effect in the composite, providing versatile and tailor made properties with performances superior to those of the individual material.

Driven by the intriguing properties of composites, many synthesis routes have been developed to explore the hybridisation between graphene and ZnO, such as solution mixing [11], sol-gel method [12], solvothermal growth [13], microwave irradiation [14] and electrodeposition [15]. However,

most reported methods utilises the Hummer's method, followed by further post chemical processes to produce reduced graphene oxide (rGO), prior to the hybridisation with ZnO. It has been reported that Hummer's method involves the use of harsh acid mixtures at high temperature and requires long processing time to produce graphene oxide (GO). As such, the as-produced GO has abundance of functional groups, such as hydroxyls and epoxides, which may not be totally eradicated through annealing or reduction processes. The resultant rGO was reported to be invariably defective, with electrical conductivity several orders below that of pristine graphene, due to the presence of these remaining residuals and defects. Studies also demonstrated that rGO with defects led to electron deflection and reverse scattering, thereby limiting electron transfer, jeopardising the superior electrical conductivity. In addition, the composite synthesis methods like solution mixing and sol-gel method also undergo a series of chemical reactions that resulted in the presence of functional group in the final product, hindering the composite electrocatalytic activity. Furthermore, other synthesis methods involved high pressure and temperature in the formation of metal oxide from precursor, leading to safety concern.

1.2 Rationale of Current Study

In order to address the aforementioned issues, this research attempts to bridge the gap between highly sensitive and specific detection of diseases with fabrication of sensing platform based on graphene/ZnO nanocomposite (G/ZnO) prepared via a facile and environmental friendly method. This research

ultimately gears towards the development of versatile sensing platform based on G/ZnO, focusing on the synthesis, characterisation and application of G/ZnO nanocomposite in electrochemical biosensor for their enhanced performance.

The specific objectives are as follow:

(i) To explore and establish facile and green approaches to synthesise G/ZnO nanocomposite

Current G/ZnO synthesis method requires improvement in terms of safety, environmental friendliness and most importantly, the quality of the final product. The synthesis method for G/ZnO nanocomposite will be explored and studied in detail, whereby the key parameters are investigated and optimised. Two different types of synthesis method will be explored to develop a more suitable approach for the preparation of G/ZnO nanocomposite.

(ii) To evaluate the electrochemical properties of G/ZnO nanocomposite for its suitability for biosensing application

Hydrogen peroxide (H_2O_2) is a common by-product of many biological reactions, therefore it is typically used as a basic analyte in most of the biosensing applications. The as-prepared G/ZnO nanocomposite will be used to develop non-enzymatic H_2O_2 sensor and the electrochemical performance of the developed sensor will be characterised via cyclic voltammetry (CV) and amperometry.

(iii) **To evaluate the performance of developed biosensing platforms for the detection of key biological molecules.**

The ultimate goal of the research is to have a G/ZnO electrode sensing platform that is highly sensitive and selective for the detection of biological molecules especially deoxyribonucleic acid (DNA) and ribonucleic acid (RNA), which are key to identify diseases at early and pre-symptomatic stage. The functionalisation of the as-synthesised G/ZnO nanocomposite with a bio-linker, PSE will be studied and optimised. The performance of the developed biosensors will be characterised via various electrochemical analysis techniques. The sensitivity and specificity, as well as limit of detection of the biosensors will be determined to evaluate the performance of the G/ZnO biosensor.

1.3 Outline of Thesis / Thesis Organisation

The general outline of this report is presented as follow:

Chapter 1, *Introduction* presents the problems associated with current diagnostics techniques and how nanotechnology can be integrated to create powerful methods that could revolutionise many aspects of disease diagnosis. The objectives of this research and the methods used to achieve them are presented.

Chapter 2, *Literature Review: Graphene/Metal Oxide-Based Electrochemical Biosensor* covers the development of biosensor, past research done on the synthesis of graphene/metal oxide composites, surface

functionalisation method and recent development in graphene/metal oxide composite-based biosensors.

Chapter 3, *Synthesis of Graphene/Zinc Oxide Nanocomposite for Application in Non-enzymatic Hydrogen Peroxide Sensing* outlines the first synthesis approach taken, where the as-synthesised graphene was mixed with ZnO nanocomposite via mechanical stirring. The results of varying the key parameters in the synthesis process are studied and discussed. The chapter ends with a basic application of the as-synthesised G/ZnO in the detection of hydrogen peroxide.

Chapter 4, *Synthesis of Graphene/Zinc Oxide Nanocomposite via Low Temperature Hydrothermal Growth* reports on the improved synthesis method employed by subjecting the as-synthesised graphene and ZnO precursor to low temperature hydrothermal growth. The electrochemical performance of the as-synthesised G/ZnO nanocomposite is evaluated via detection of hydrogen peroxide, which could be explored further for future biosensing application.

Chapter 5, *Proof of Concept Detection of Avian Influenza H5 Gene by Graphene/Zinc Oxide Nanocomposite-Enhanced Electrochemical Genosensor* reports a conceptual exploration of Avian Influenza *H5* gene detection based on screen printed carbon electrodes modified with the G/ZnO nanocomposite synthesised via low temperature hydrothermal growth, which was in turn functionalised with a bi-linker, PSE and HRP-conjugated antifluorescein antibody.

Chapter 6, *Sensitivity Enhancement of Graphene/Zinc Oxide Nanocomposite-based Electrochemical Impedance Genosensor for Single Stranded RNA Detection* further explores the potentiality of G/ZnO nanocomposite as electrode material by fabricating an electrochemical impedance genosensor for the detection of Coconut Cadang-Cadang Viroid Disease single stranded RNA.

Chapter 7, *Conclusion and Future Direction* summarises the work done and findings thus far. This report ends with the future direction that this project can be headed towards as outlined in the final chapter.

Chapter 2 Literature Review: Graphene/Metal Oxide-Based Electrochemical Biosensor

2.1 Overview

The history of biosensors started in the year 1962 with the first successful presentation of enzyme electrodes by Professor Leland C. Clark Jr. at a New York Academy of Sciences symposium. The first biosensor described in the published paper was termed "enzyme electrode" where the enzyme glucose oxidase was entrapped in a dialysis membrane over an oxygen probe [16]. Since then, scientific communities have been intrigued in exploring the biosensor field, where some of the important events in the history of biosensor development are detailed in Table 2.1.

Table 2.1: Defining events in the history of biosensor development (adopted from Setford and Newman [3]).

Date (year)	Event
1956	Invention of oxygen electrode
1962	First presentation of a biosensor
1969	Development of the first potentiometric biosensor
1970	Invention of ion-selective field-effect transistor
1972	Development of the first commercialised biosensor
1975	Development of the first micro-based biosensor and immunosensor
1976	First bedside artificial pancreas
1980	First fibre optic pH sensor for *in vivo* blood gases
1982	First fibre optic-based biosensor for glucose
1983	First surface plasmon resonance (SPR) immunosensor
1984	First mediated amperometric biosensor

Following the defining historical events, the development of biosensor continues to be an extremely dynamic and growing area for scientific research. Interdisciplinary experiment communities from different backgrounds, such as Material Science, Chemistry, Physics, Biotechnology and more work together to develop biosensing devices with higher reliability and sensitivity for use in wide variety of applications.

Nanotechnology is the scientific area dealing with materials with size smaller than 100 nm. With the rapid advancement and remarkable achievements in nanotechnology and nanoscience, nanomaterials has become the most exciting forefront fields in biosensors fabrication. The integration of nanomaterials into biosensing systems is one of the popular research topics, opening up the possibility for vast variety of applications. The engagement of nanomaterials into sensing devices or sensor platforms generates novel interfaces that enable detection of target molecules with enhanced sensitivity and lowered detection limits.

The huge interest in nanomaterials is driven by their many desirable properties. Significant progress has been achieved in synthesis methods to prepare nanomaterials of desired properties, such as controllable size, shape, surface charge and physiochemical characteristics. Usage of nanomaterials in biosensors fabrication allows designing of novel sensing systems and enhancing the performance of the detection assay, revolutionising the fields of chemical and biological analysis.

In this chapter, a brief review of graphene/metal oxide composite-based biosensors will be presented. This review is essential as the synergistic effect between graphene and metal oxide will be exploited in the fabrication of biosensors. This chapter also presents the background into the fundamentals of biosensor, synthesis route for graphene/metal oxide composite and functionalisation method in biosensors.

2.2 Fundamental of Biosensor and Electrochemical Biosensor

Biosensor can be defined as an analytical device that converts a biological response into a quantifiable and processable signal [17]. According to the International Union of Pure and Applied Chemistry (IUPAC) definition, "A biosensor is a self-contained integrated device which is capable of providing specific quantitative or semi-quantitative analytical information using a biological recognition element (biochemical receptor) which is retained in direct spatial contact with a transducer element."[2].

A biosensor harnesses the exquisite specificity and sensitivity of biological compound in conjunction with physiochemical transducers to offer powerful analytical tool. The potential application of biosensor embraces virtually analytical task in all aspect, ranging from medical diagnostics, drug discovery, food safety, process control, environmental monitoring to defence and security system [18].

A typical biosensor can be considered as the combination between biological and physiochemical components (Figure 2.1) [19]. The biological components refer to biological molecules capable of recognising and interacting with specific analyte, such as antibody, enzyme, nucleic acid and more. The physiochemical components usually refer to transducers, which convert the bioreceptor-analyte interaction into signals. The signal generated from the specific biological event is collected at electrode interface, then amplified, processed and finally displayed.
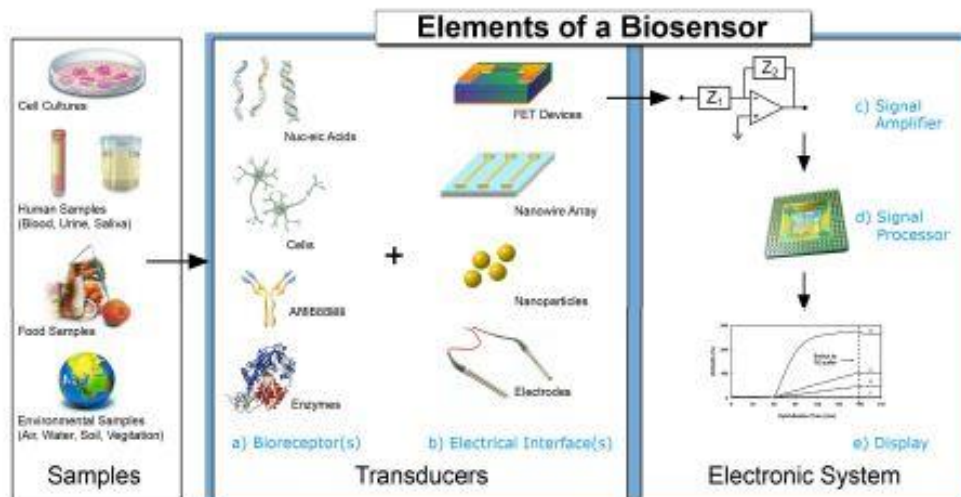
Figure 2.1: Typical elements in a biosensor, which consist of bioreceptor, interface architecture and electronic system [19].

Over the past three decades we have witnessed a tremendous amount of activity in the area of biosensors. Growth in the field of biosensors has been phenomenal as displayed in Figure 2.2. The principal journal in the field, *Biosensors and Bioelectronics* was launched in year 1985 by Elsevier, and thereafter has led to an uprising trend in this research area [18]. The interest of the scientific community towards the fabrication of biosensor is reflected in the exponential rise in the number of publications between years 1985 to 2016, as revealed in the Web of knowledge search using the keyword "biosensor".
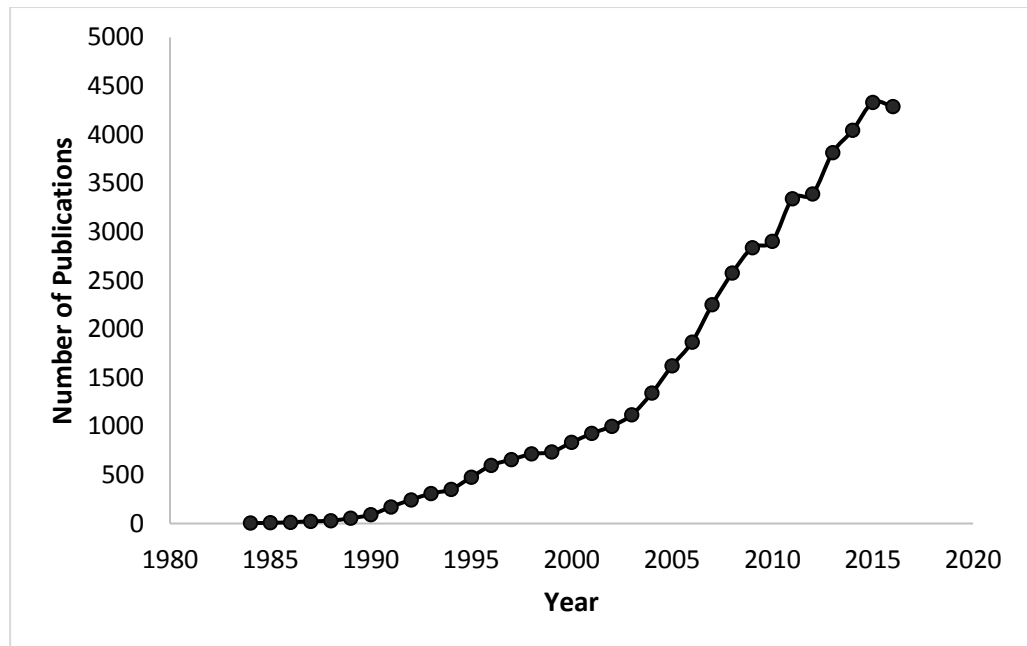
Figure 2.2: Publication trend obtained using the keyword "Biosensor" from the year 1984 to 2016, using the Web of Knowledge. There exist an upward trend and thus a rising interest in biosensor fabrication resulting in an exponential rise in publications.

Biosensors consist of many advantages, therefore attracted the interest of scientific community. The main advantages of biosensors are listed as below [20]:

1. Biosensors are highly sensitive, enabling detection of target molecule at a concentration of picomolar

2. The detection mechanisms of biosensors are highly specific due to the bioreceptor-analyte interaction

3. Biosensors enable real time, continuous detection of target molecule, providing insights into binding and dissociation mechanism, as well as affinity values

4. Response time for biosensors is short

5. Miniaturised biosensors are portable, enabling on-site testing

Due to the advantages of biosensors, they have many potential applications in different areas, generally categorised into medical, research, food, environment and military (Figure 2.3). In the medical field, biosensors can be applied for drug discovery, disease diagnosis, pharmaceutical use and more. In food and environment field, biosensors can be employed for product monitoring, pollution monitoring and quality control. Biosensors could also be applied in the research and military field.
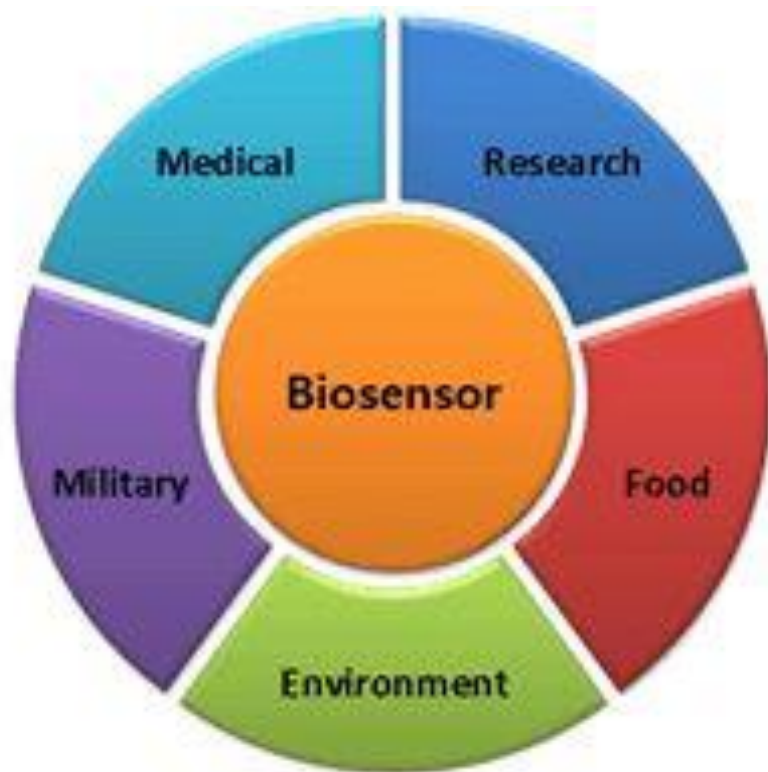
Figure 2.3: Schematic diagram displaying the potential applications of biosensors in different areas, generally categorised into medical, research, food, environment and military.

2.2.1 Classification of Biosensor

Biosensors generally can be classified through two ways, based on the biological specificity-conferring mechanism or the mode of physiochemical signal transduction. According to transducing element, biosensors can be categorised into four main types, optical, thermometric, piezoelectric and electrochemical biosensor (Figure 2.4).
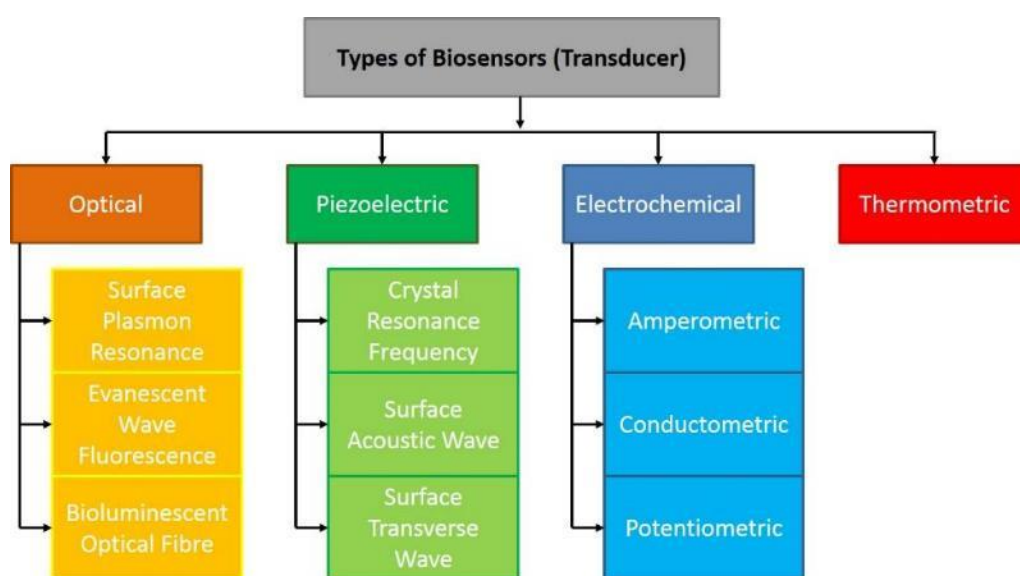
Figure 2.4: Classification of main biosensor type based on the basic principles of signal transduction.

2.2.1.1 Optical Biosensor

Optical biosensors are one of the most common reported class of biosensors. The optical detection is achieved through the interaction of the optical field with a biorecognition element as displayed in Figure 2.5. In general, optical biosensing can be divided into two modes, label-free and label based. In label-free mode, the optical signal is generated directly via the interaction between the sample and transducer. In the latter case, the sensing involved the

use of a label and the optical signal is then produced through a colorimetric, fluorescent or luminescent method. The widely used optical biosensor systems include surface plasmon resonance (SPR), evanescent wave fluorescence, bioluminescent optical fibre, as well as interferometric, ellipsometric and reflectometric interference spectroscopy [21].
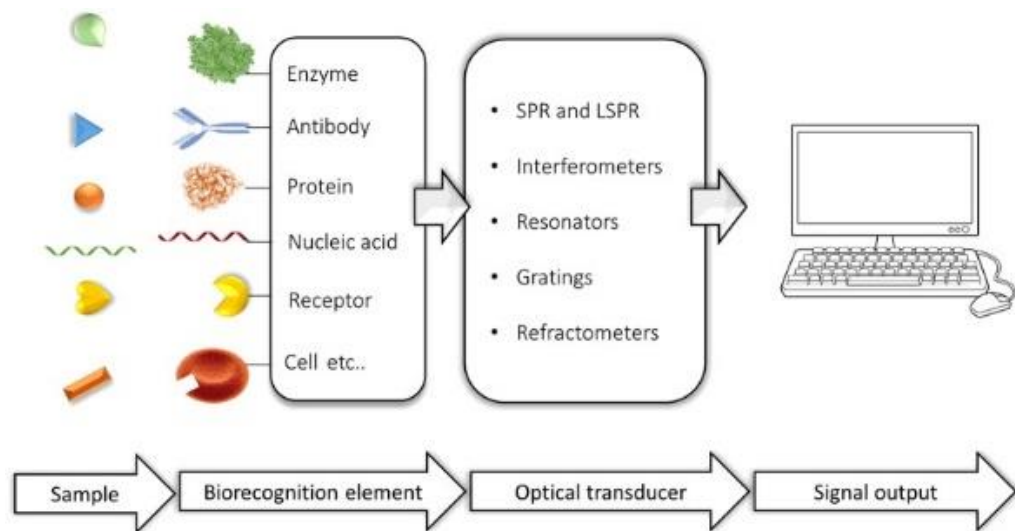
Figure 2.5: Schematic diagram illustrating the elements of an optical biosensor [21].

2.2.1.2 Thermometric Biosensor

Thermometric biosensor works based on the fundamental property of biological reactions, which is the absorption or evolution of heat [22]. The change in the temperature within the reaction medium is monitored to calculate the extent of reaction or structural dynamics of biomolecules in the dissolved state. The total heat evolution or absorption is proportional to the molar enthalpy and the total number of product molecules generated from the biochemical reaction [23].

2.2.1.3 Piezoelectric Biosensor

When an anisotropic (lacking symmetry) crystal such as quartz crystal is stressed, the piezoelectricity property of the crystal will cause an electric field to develop [24]. Similarly, when the crystal is subjected to an electric field, it will undergo a mechanical deformation. The crystal will oscillate with applied frequency under an alternating voltage, where the natural frequency of the crystal is related to the mass and elastic constants of the crystal. Piezoelectric transducers deliver mechanical and electrical forces to a biological medium in the form of progressive or standing acoustic waves and the deformation is recorded as shown in Figure 2.6.
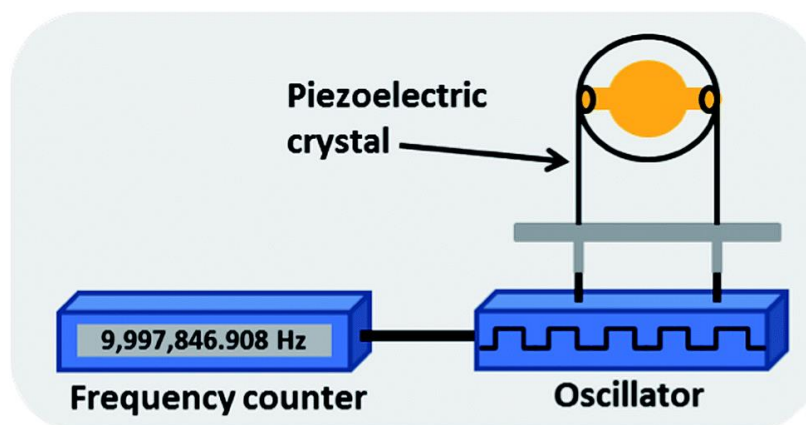
Figure 2.6: Experimental setup of a piezoelectric quartz crystal based biosensor where the change in resonating frequency is measured [25].

2.2.1.4 Electrochemical Biosensor

Electrochemical biosensors are molecular sensing devices which couple biological recognition element to electrochemical transducer. The biosensors operate by converting the biological recognition event to electrical signal proportional to the analyte concentration. Electrochemical devices have

always been the focus of attention in biosensor development, emerging as the most commonly used biosensors in monitoring and diagnosis test in clinical analysis.

Based on the operating principle, electrochemical biosensors can employ three types of transducers to convert the chemical information into signal (Figure 2.7):

(i)   Amperometric - Amperometric biosensor measures the current resulting from the electrochemical oxidation or reduction of an electroactive species at a fixed bias potential [26]. It can provides information on the quantity of the analyte as the relationship between the concentration of the analyte and the current generated is linear. Determination of analyte concentration is essential for a wide range of applications, such as high-throughput drug screening, disease diagnosis, quality control and more. Therefore, amperometric biosensors are one of the most widespread class of biosensors.

(ii)   Potentiometric - A potentiometric biosensor measures the difference in potential between the working and reference electrode or between two reference electrodes across an ion-selective membrane at zero current flow [27]. The electrode potential generated at the membrane electrode surface in equilibrium is proportional to the logarithm of the analyte concentration. The basis of potentiometric monitoring is based on the concentration dependence of the potential (E), at reversible redox electrodes according to the Nernst equation (Equation 2.1) [28]:

$$E = E_0 + \frac{RT}{nF} \, ln \, [\frac{Ox}{Red}] \qquad\qquad \text{Equation 2.1}$$

where E_0 is the standard redox potential, R is the gas constant, T is the absolute temperature, F is the Faraday constant, n is the number of exchanged electrons.

(iii)   Conductometric - A conductometric biosensor measures the changes in the electrical conductivity or impedance of the solution [29]. During the course of a biochemical reaction, there will be changes in the ions or electrons of the solution, thereby affecting the overall resistivity. The expression of impedance is shown in Equation 2.2 [30]:

$$Z^2 = R^2 + \frac{1}{(2fC)^2} \qquad \qquad \text{Equation 2.2}$$

The inverse value of resistance is called conductance and thus the name conductometric is applied.
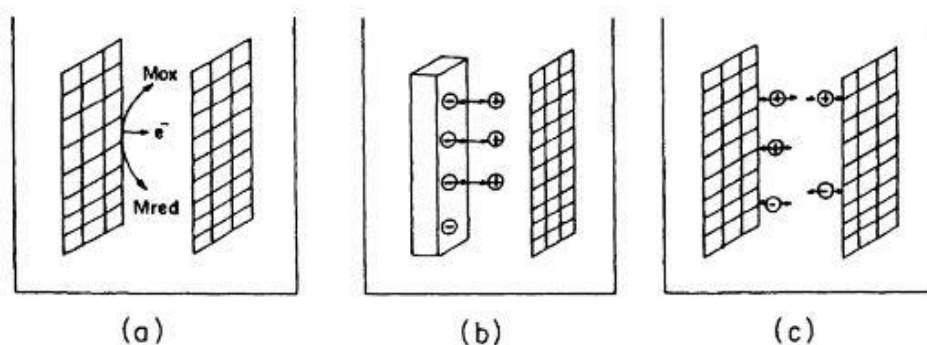
Figure 2.7: Schematic diagram displaying the principle of (a) amperometric, (b) potentiometric and (c) conductimetric biosensors, where M_{red} is reduced mediator, M_{ox} is oxidised mediator [28].

Electrochemical biosensors have played an important role in the development of biosensor towards more simplified testing. They are generally more amenable to miniaturisation, have compatible instrumental sensitivity and can even operate in turbid media [31]. Inexpensive electrodes can be easily

integrated to perform rapid measurements in miniaturised easy-to-use portable electrochemical devices. The high sensitivity, specificity, simplicity and inherent miniaturisation of modern electrochemical bioassays enable them to be the most attractive system among all biosensor types.

2.3 The Graphene Family

The rapid advancement in nanotechnology has demonstrated their potentials to be employed in many applications, including biosensing application. The integration of nanomaterials into biosensors led to enhanced sensing performances with improved detection sensitivity and lower detection limit [4]. The applications of nanomaterials in biosensors enable the fabrication of high performance sensing platforms for the detection of target molecules. The huge interest in applying nanomaterials is due to the ability to tailor the size, structure and hence the properties of nanomaterials, offering excellent prospects for novel sensor design with enhanced performance.

Nanomaterial is defined as "material with any external dimension in the nanoscale or having internal structure or surface structure in the nanoscale", where nanoscale is defined as the size range from approximately 1 to 100 nm by the International Organization for Standardization (ISO) [32]. In particular, graphene, a two dimensional (2D) material consisting of a single atomic layer of carbon arranged in a honeycomb lattice, has intrigued enormous scientific activities due to its extraordinary properties. Ever since Geim and Novoselov [5] successfully isolated graphene from graphite in year 2004, this 2D carbon crystal has been highly anticipated to provide unique and ground breaking

endeavour for various applications. It is the thinnest and strongest material ever known, possessing outstanding optical, mechanical properties together with superior electrical and thermal conductivities due to its sp^2-hybridised carbon and electronic configuration [33].

There are several materials associated with graphene, which are obtained through different synthesis routes. These include graphite oxide, graphene oxide and reduced graphene oxide (rGO), which could be referred as members of the "graphene family". The classification of the graphene family members and the possible routes from one to another is shown in Figure 2.8. "Top-down" synthesis routes run from top left to bottom right, they generally start with bulk material such as graphite or graphite oxide. Stepwise structural decomposition was carried out via exfoliation route (route 2 and route 4), resulting in graphene or graphene oxide. In contrast, "bottom-up" synthesis routes run from bottom right to top left as the materials are assembled layer by layer. For instance, graphene can be synthesised via chemical vapour deposition (CVD) of methane or thermal decomposition of silicon carbide (SiC).

There has been an exaggerated use of acronyms in the literatures all referring to the same material, with examples being CRGO, GO, rGO, GR, G, GNS, EG, GNP, CCG, ERGNO, ERGO, CRGNO and many more. This phenomena possesses a high risk of confusion, as the acronym "GO" may refer to graphite oxide or graphene oxide. In this context, the "graphene family" is classified into five members, which are graphite, graphite oxide, graphene, graphene oxide

and reduced graphene oxide (rGO), with their respective definition as listed in

Table 2.2.
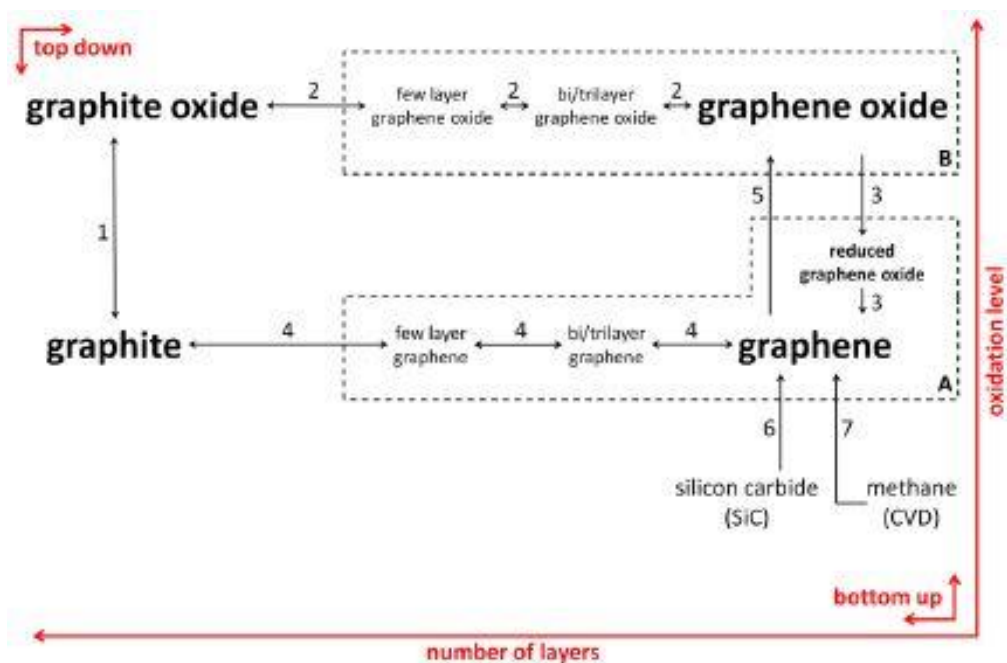
Figure 2.8: Classification of the members of "graphene family". Routes: (1) Oxidation of graphite to graphite oxide via Hummers, Staudenmeier or Brodie method; (2) Step-wise exfoliation of graphite oxide to graphene oxide via sonication; (3) Reduction of graphene oxide by chemical reactions, thermal annealing or electrodeposition; (4) Mechanical exfoliation of graphite to graphene; (5) Oxidation of graphene to graphene oxide; (6) Thermal decomposition of SiC wafer; (7) Growth of graphene films by chemical vapor deposition.

Table 2.2: Classification of the members of "graphene family".

Material	Definition
Graphite	An allotropic form of the element carbon consisting of layers of hexagonally arranged carbon atoms in a planar condensed ring system. The layers are stacked parallel to each other in a three-dimensional crystalline long range order.
Graphite oxide	An heterogeneous material prepared by the oxidation of graphite. It can be described as an assembly of many layers of graphene oxide.
Graphene	One layer of a polycyclic aromatic hydrocarbon network, with all carbon atoms hexagonally arranged in a planar condensed ring system. It has a metallic character and consists solely of carbon and hydrogen.
Graphene oxide	Structurally similar to graphene, except that it has various oxygen groups and is partially aromatic. The C:O ratio is between 2 and 3.
Reduced graphene oxide (rGO)	Structurally similar to graphene oxide, except that it has an oxygen fraction around or below 10%.

2.4 Synthesis of Graphene/Metal Oxide Composite

In view of the excellent properties of graphene, it is recognised as one of the most promising materials in research areas. Graphene has a high specific area of 2630 m^2g^{-1} that can be exploited as superior platform for the development of nanocomposites [34]. Hence, the production of graphene/metal oxide composites has been expected to provide groundbreaking endeavour in a wide variety of application. The hybridisation between graphene and metal oxide nanoparticles could result in versatile and tailor-made properties with performances superior to those of individual graphene or oxide nanomaterials due to the synergetic effect between them.

2.4.1 Solution Mixing

Solution mixing is an efficient and direct method that has been widely used in the preparation of graphene/metal oxide composites. A variety of graphene/metal oxide composites were synthesised by precipitating the mixed solution of metal salts with graphene oxide (GO), followed by reduction of GO (Figure 2.9) [35]. For example, graphene/SnO_2 composites was synthesised by hydrolysis of $SnCl_4$ with NaOH, which was then mixed with graphene dispersion in ethylene glycol [36]. Similarly, Peng and colleagues [11] sonicated GO and zinc acetate dehydrate in diethylene glycol to synthesise rGO (reduced graphene oxide)/ZnO. The synthesis of graphene/Fe_3O_4 composites via precipitation of Fe^{3+}/Fe^{2+} ions and GO in alkaline solution followed by reduction with hydrazine hydrate or oxidation with KBH_4 was reported in a few studies [37-40]. Independently, rGO/SnO_2 composite was prepared by subjecting tin (II) acetate and GO mixture to supercritical methanol medium [41].
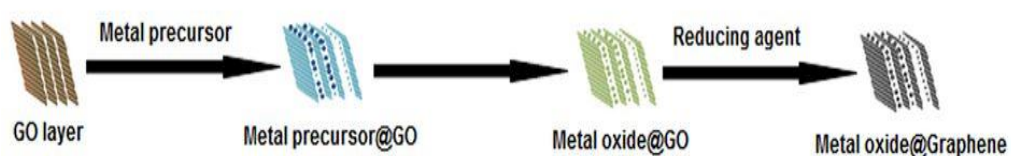
Figure 2.9: Schematic representation of the synthesis of graphene/metal oxide composites via solution mixing [35].

2.4.2 Sol-Gel Method

The sol-gel process is a low cost and versatile technique that typically uses metal alkoxides or chloride as precursors to undergo a series of hydrolysis and polycondensation reactions for the synthesis of graphene/metal oxide

nanocomposite (Figure 2.10) [42]. In general, the sol-gel process involves the transition of a solution system from a liquid "sol" (mostly colloidal) into a solid "gel" phase in different forms for different applications. The sol-gel method has been applied in the synthesis of many materials, most commonly reported are graphene/TiO2 [43-47], graphene/ZnO [12, 48-50] and graphene/Fe$_3$O$_4$ [51, 52]. Noteworthily, Azarang and colleagues [53] synthesised rGO/ZnO via sol-gel method by utilising an environmental friendly polymerisation agent, starch, which expands during calcination to terminate the growth of ZnO nanoparticles. Although the sol-gel process is a cost effective technique, it has the drawback of requiring crystallisation and post-annealing steps to convert the product from amorphour phase into defined crystals [35].
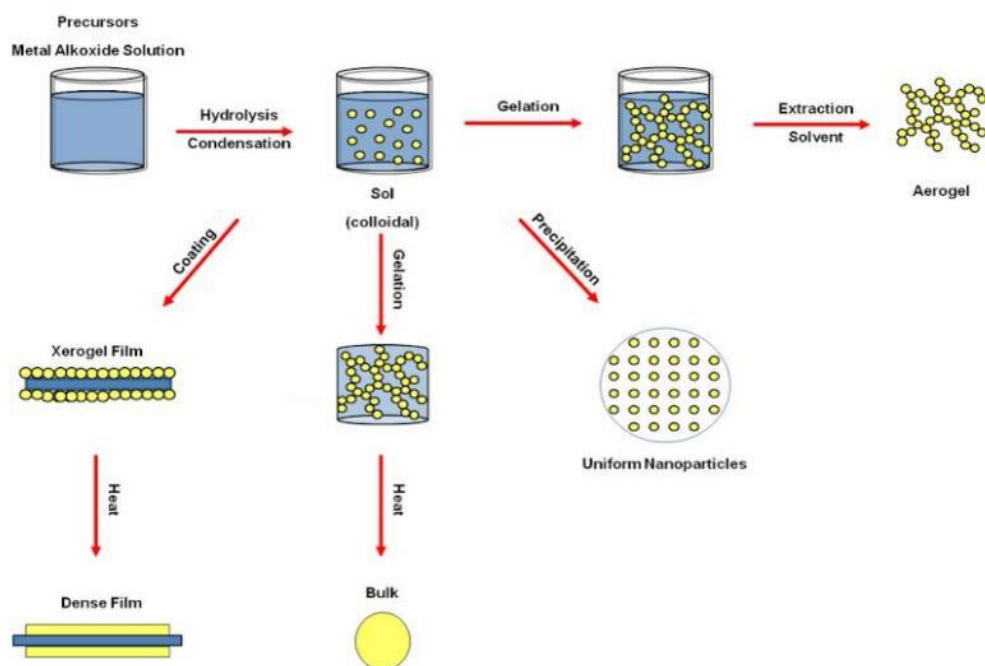
Figure 2.10: Schematic diagram represents the sol-gel process which involves the transition of "sol" into "gel" [42].

2.4.3 Hydrothermal/Solvothermal Method

The hydrothermal and solvothermal approaches are among the most commonly used strategies for the preparation of graphene/metal oxide nanocomposites [54]. It is a powerful process that is generally carried out in autoclave under high vapour pressure and high temperature. There are several advantages of using this method, it could remove the oxygen-containing groups in the material via dehydration, accelerate heterolytic bond cleavage and also the properties of the final product can be tuned by adjusting the pressure and temperature of the reaction. However, the requirement of high temperature and long reaction times are the major drawbacks of the method upon comparing with other energy efficient method.

The difference between hydrothermal and solvothermal process is the solvent used in the reaction, if water is used, the process is termed as "hydrothermal synthesis", otherwise, it is generally termed as "solvothermal synthesis". For hydrothermal process, the reaction is performed below the supercritical temperature of water (374 °C) and the morphology of the materials could be controlled by manipulating the kinetic control and chemical concentration [55]. Wu and colleagues [56] sonicated the TiO_2 and GO suspension to achieve homogeneous mixing, which was transferred to a Teflon-lined autoclave at 180 °C for 12 hours to prepare graphene/TiO_2 composite. Similar approach was performed on graphene/TiO_2 [57-79] , graphene/ZnO [13, 80-92], graphene/NiO [93-96], graphene/MnO_2 [97-106], graphene/Fe_2O_3

[107-116], graphene/SnO_2 [117-128], graphene/Mn_3O_4 [129-131], graphene/Fe_3O_4 [132-136] and graphene/CuO [137].

Indepedently, Ezeigwe and colleagues performed solvothermal process at a low temperature of 90 °C for the synthesis of graphene/ZnO [138] and graphene/MnO_2 [139] composites. Liu and colleagues [140] performed a one-step microwave hydrothermal method for the synthesis of graphene/SnO_2 composite. The GO and SnO_2 precursor ($SnCl_2 \cdot 2H_2O$) were mixed and transferred to Teflon vessel, which was then heated up in a microwave for 30 minutes (1000 W, 200 °C, 20 bar). The TEM and HRTEM (Figure 2.11) characterisations on the as-synthesised graphene/SnO_2 composite showed that the graphene sheet is covered by ultrafine SnO_2 nanoparticles while the interplanar distance of 0.33 nm identified the SnO_2 nanoparticles.
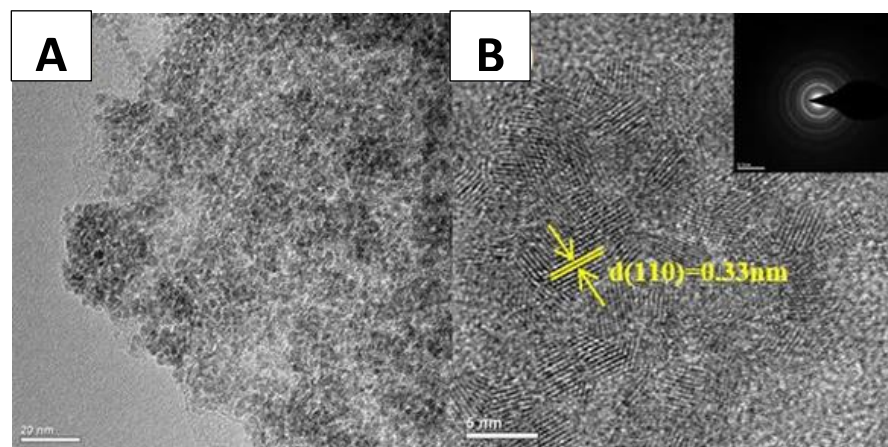
Figure 2.11: (A) TEM and (B) HRTEM images of graphene/SnO_2 composite [140].

2.4.4 Microwave Irradiation

Microwave irradiation is a rapid and powerful technique offering simple, fast, clean, efficient and economical method for the production of nanomaterials with high purity and uniformity [141]. It is widely used as a green and facile technique in the synthesis of graphene/metal oxide composite. In this approach, microwave irradiation is applied to trigger chemical reactions, the microwave radiation passes through the wall of the container and heats the reactant together with the solvent [55]. The benefit of using microwave irradiation technique is that uniform heating can be achieved and the solvent can be heated above the actual boiling point, facilitating the nucleation of nanoparticles and shortening the required synthesis time (Figure 2.12) [142]. The drawback of this method will be the end product, which is in solid state, might not be desirable for further processing [54].
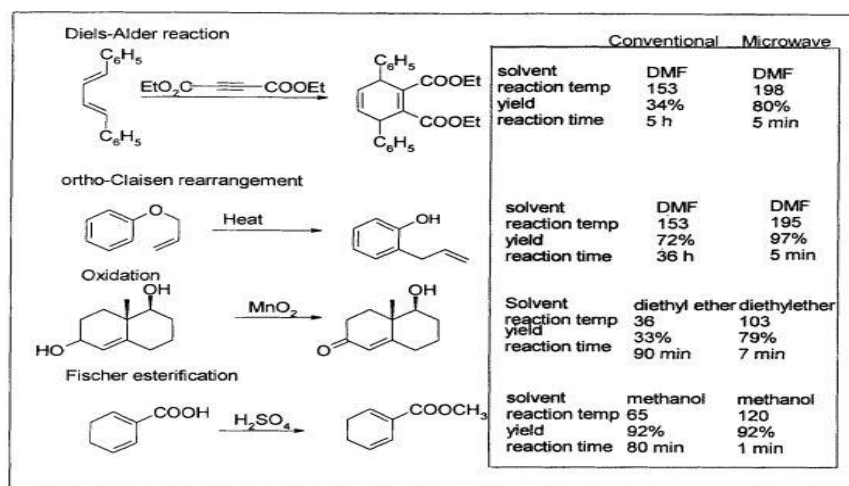
Figure 2.12: Schematic diagram showing comparison for the chemical reactions carried out through conventional heating and microwave irradiation method [142].

As a typical example, Liu et al. [143] synthesised rGO/Fe_2O_3 composite by microwave (MW) assisted method using GO and $Fe(NO_3)_3 \cdot 9H_2O$ as precursors, and urea as the reducing agent. The solution was sealed and heated at 150 °C with maximum microwave irradiation power of 100 W for 10 minutes. The resulting material showed uniform distribution of Fe_2O_3 nanoparticles (diameters of 4-8 nm), demonstrating excellent cycle performance as electrode material for sodium ion batteries. She and colleagues [144] also reported on the synthesis of rGO/Mn_3O_4 composite using MW assisted method (Figure 2.13). GO was mixed with $KMnO_4$ and ethylene glycol before subjecting to microwave irradiation power of 800 W for 2.5 minutes to prepare rGO/Mn_3O_4 for application as high performance supercapacitor. Other materials were also synthesised through MW assisted method, for instance, graphene/CuO [145] and graphene/Co_3O_4 [146].
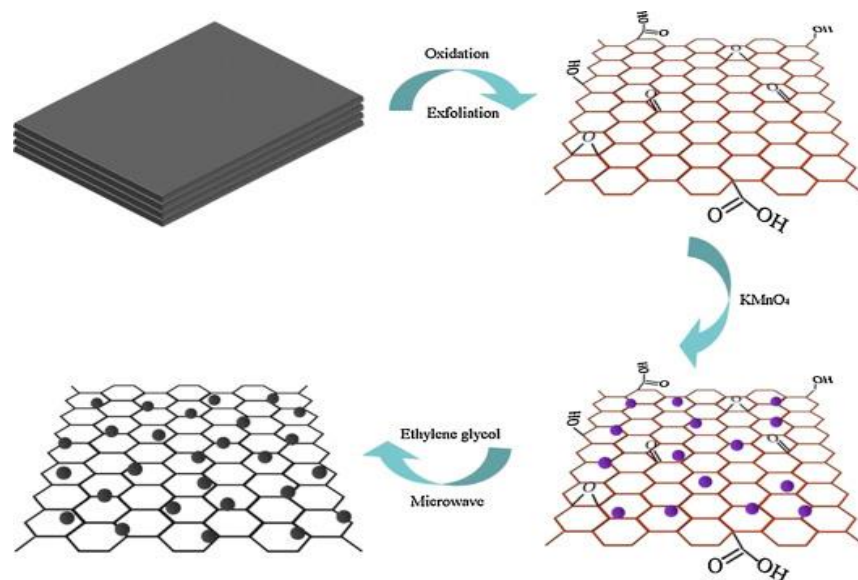
Figure 2.13: Schematic diagram showing the synthesis of rGO/Mn₃O₄ composite with MW assisted method [144].

2.4.5 Other Synthetic Methods

There are several other techniques that have also been explored for the synthesis of different graphene/metal oxide composites, such as electrodeposition, atomic layer deposition, self-assembly, photo assisted reduction, ultrasonication, physical absorption and more. Each method has its advantages and disadvantages which are summarised in Table 2.3.

Table 2.3: Comparison of the advantages and disadvantages of the major synthesis methods for graphene/metal oxide composite.

Methods	Advantages	Disadvantages	References
Solution Mixing	1. Simple reaction set up. 2. Degree of reduction controlled by choice of reducing agent 3. Low power consumption 4. Possible large-scale production	1. Purification of final product from reducing agent	[11, 35-41]
Sol-Gel	1. Cost effective 2. Low temperature required	1. Final product requires post-processing	[12, 43-53]
Hydrothermal/ Solvothermal Synthesis	1. Simple reaction set up	1. High temperature and pressure required	[13, 55-137]

	2. Tunable degree of reduction	2. Long reaction time	
	3. Impurity free final product	3. High energy consuming	
Microwave Irradiation	1. Green approach	1. Final product in solid state difficult for further processing	[143-146]
	2. Rapid reaction time		
	3. Little amount of by-products	2. Potentially high risk	

2.5 Immobilisation Techniques

For sensing purposes, bio-specific entity has to be immobilised onto nanomaterials through different strategies, which are categorised as covalent binding and noncovalent interaction. The immobilisation of biomolecules onto graphene/metal oxide composite-based sensing devices is a critical factor in determining the performance of the sensor. The chosen immobilisation method must retain the stability and activity of the bound biological receptor.

2.5.1 Covalent Binding

Covalent binding is the strategy to attach biomolecules covalently to nanomaterials. This technique has an advantage in terms of stability and reproducibility of the surface functionalisation. The disadvantage of this technique would be the uncontrolled anchoring of the biomolecule which can affect the domain responsible for recognition event or potential loss in the activity of the immobilised biomolecules [147].

A primary example of covalent binding is the avidin-biotin complex. Biotin (Vitamin H) is a low molecular weight cofactor that binds specifically to avidin or streptavidin. For example, Li et al. [148] fabricated a sandwich-type electrochemical immunosensor based on the biotin-streptavidin specific recognition. Polyaniline functionalised graphene/SnO_2 composite (GS-SnO_2-PAN) was applied to modify the electrode and the human immunoglobulin G (HIgG) was bound onto the modified electrode. Subsequently, the B-Ab_2 solution and streptavidin (SA) were added to the surface of the electrode. Finally, the conjugated biotin (B-Fe_3O_4@APTES) was bound onto the electrode via biotin-streptavidin specific recognition.

Other than streptavidin-biotin complex, Zhang et al. [149] covalently attached glucose oxidase (GO_x) onto Fe_3O_4/chitosan-functionalised graphene (CG) composite for the purpose of glucose detection. The active carboxyl groups on the chitosan formed covalent bond with GOx and thereby fabricating the glucose sensor based on Fe_3O_4/CG composite.

2.5.2 Noncovalent Interaction

Noncovalent interactions primarily involve hydrophobic, van der Waals, electrostatic forces, pi-pi interaction, entrapment in polymers and physical adsorption of molecules on the graphene surface. The noncovalent interactions are very important for most applications because the extended pi system of graphenic nanostructures are not interrupted, indicating the important properties such as electrical conductivity or mechanical strength are not affected [150]. In addition, the mild and nonpermanent characteristic of

noncovalent interactions offers high flexibility in applications, preserving all specific properties of both nanomaterials and biomolecules.

Liu et al. [79] immobilised tyrosinase onto graphene/TiO_2 composite via entrapment with the polymer, Nafion for the detection of catechol. Similarly, glucose oxidase (GO_x) was immobilised onto graphene/MnO_2 composite via Nafion in the fabrication of amperometric glucose biosensor [104]. Zhang and colleagues [151] immobilised GO_x onto rGO/MnO_2/Au composites with the aid of poly(diallydimethylammonium chloride) (PDDA) to generate a glucose biosensor with high sensitivity and low detection limit (Figure 2.14).
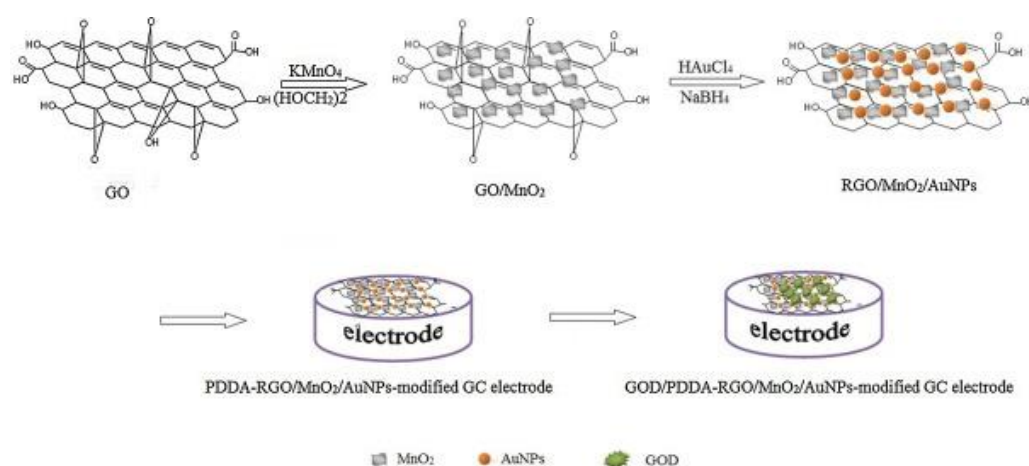
Figure 2.14: Schematic diagram showing the fabrication of PDDA-rGO/MnO₂/Au composite-based sensing platform with glucose oxidase (GOD) being immobilised on the platform [151].

Figure 2.15 illustrates the π-π interaction of a planar pyrene molecule on a graphene substrate. Jahanbani and Benvidi [152] applied 1-pyrenebutyric acid-N-hydroxysuccinimide ester (PANHS) as a linker between single stranded DNA (ssDNA) probe and Fe_3O_4/rGO composite. The rGO displayed π-π

interaction with the pyrene molecule in PANHS for noncovalent binding of ssDNA probe onto sensing platform.
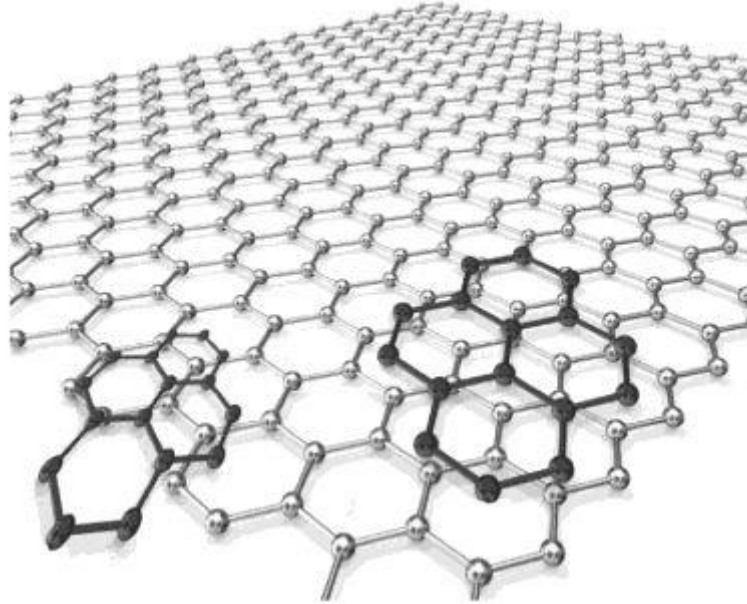
Figure 2.15: The π-π interaction of a planar pyrene molecule on the surface of graphene [153].

2.6 Graphene/Metal Oxide Composite for Biosensing

Recent advancements in the field of nanotechnology and nanoscience have opened the gates for the tremendous achievements in biosensing with nanomaterial-based electrochemical signal amplifications. The application of nanomaterial in the field of biosensing has great potential in improving both sensitivity and selectivity. Furthermore, nanomaterials can also produce synergistic effect among each other to accelerate the signal transduction and amplify biorecognition events with specifically designed signal tags, leading to highly sensitive biosensing. The applications of graphene/metal oxide

composite-based electrochemical biosensor in recent years are discussed in the following sections.

2.6.1 Detection of Biomolecules

The study of electrochemical behaviour of bioactive molecules has become one of the most rapidly developing scientific fields. The detection of biomolecules including hydrogen peroxide, glucose, dopamine, ascorbic acid, uric acid, cholesterol, acetaminophen and tryptophan are performed via electrochemical biosensors modified with different graphene/metal oxide composites as detailed in Table 2.4.

Hydrogen peroxide (H_2O_2) is a small molecule that has been widely applied in the pharmaceutical, clinical, environmental, food manufacturing and chemical industries due to its strong oxidising and reducing properties [154]. H_2O_2 also plays a crucial role as a signalling molecule in living organisms, regulating diverse biological processes. In addition, H_2O_2 is a byproduct generated from various classic biochemical reactions catalysed by enzymes, thereby monitoring the concentration level of H_2O_2 is of practical significance.

Feng et al. [105] prepared MnO_2/graphene composite via hydrothermal synthesis route for nonezymatic detection of H_2O_2. Wu and colleagues [106] also used similar method to synthesise MnO_2/rGO composite and manged to achieve wider linear range of detection. MnO_2/rGO composite was also employed as flexible electrode for the tracking of H_2O_2 secretion in live cells macrophages, demonstrating the potential in point-of-care testing devices [155]. Furthermore, the MnO_2/graphene composites are hybridised with other

materials to improve the sensor performance, such as rGO/MnO$_2$/Au [151], MnO$_2$/Fullerene/graphene [156] and Mn$_3$O$_4$-MnO$_2$/graphene [157]. Electrochemical biosensor for nonenzymatic detection of H$_2$O$_2$ was also synthesised based on SnO$_2$-rGO [126], graphene/ZnO [158, 159] and rGO/Fe$_2$O$_3$ [160]. On the other hand, Sharma and Mobin [161] synthesised a cytocompatible CuO/graphene nanosphere composite as peroxidase mimic for detection of H$_2$O$_2$ and free cholesterol. H$_2$O$_2$ produced during the oxidation of free cholesterol in the presence of cholesterol oxidase was detected with limit of detection (LOD) of 6.88 μM.

Glucose is a type of monosaccharide that is categorised as relatively small molecules. It is an important metabolic material in the human body, the index of variation in glucose concentration can be used as a direct indication of body health. Therefore, quantification of the glucose concentration plays an important role in clinical diagnostic areas. In particular, electrochemical biosensor based on CuO composite is favourable in the application of glucose sensing due to the high catalytic activity to glucose oxidation and good durability of CuO [145]. For instance, CuO/graphene composites are synthesised and used in nonenzymatic detection of glucose with excellent LOD [145, 162-165]. Lu et al. [94] functionalised nickel oxide hollow sphere with Nafion to form electrostatic interaction with rGO, and the resulting NiO-rGO composite was applied for glucose biosensing. Similarly, Yang and colleagues [131] synthesised Mn$_3$O$_4$/nitrogen-doped graphene composite for nonenzymatic glucose sensor with a good sensitivity of 101.1 uAmM^{-1}.

Li and colleagues [166] studied the direct electron transfer of glucose oxidase (GO_x) via rGO/ZnO/Ag composite-modified glassy carbon electrode. The Michaelis-Menten constant of the adsorbed GO_x obtained was 0.25 mM, implying remarkable affinity of the GO_x for glucose. Zhang et al. [149] also fabricated multifunctional glucose biosensor modified with Fe3O4/chitosan/graphene composite. Other materials such as MnO_2/graphene [104] , rGO/MnO_2/Au [151] and Ag-Graphene-TiO_2 [167] were also employed in enzymatic glucose biosensors with comparable performances.

Dopamine (3,4-dihydroxyphenyl ethylamine, DA), ascorbic acid (AA) and uric acid (UA) normally coexist together. They are the important molecules for physiological processes in human metabolism where DA is an important neurotransmitter in the central nervous system of the mammals, AA is a constituent of the cell with momentous biological functions and UA is the principal final products of purine metabolism in the human body [168]. The detection of DA by electrochemical biosensor has been demonstrated in a few studies [38, 92, 128, 135, 136, 169]. Notably, Liu et al. [170] simultaneously detect DA, acetaminophen and tryptophan through NiO-CuO/graphene composite-modified biosensor. On the other hand, Xie and colleagues [168] demonstrated simultaneous electrochemical determination of DA, AA and UA. Other works have also been reported on the detection of AA [108] and UA [91, 171] respectively.

Table 2.4: Performances of graphene/metal oxide-based biosensors for the detection of small molecules.

Analyte	Material	Detection Range (μM)	Limit of Detection (μM)	Sensitivity (μA mM^{-1} cm^2)	Reference
	SnO_2-rGO	0.5–800	0.478	-	[126]
	MnO_2/rGO	100–45400	10	59	[155]
	MnO_2/graphene	10–90; 200–900	2	-	[105]
Hydrogen Peroxide (H_2O_2)	rGO/MnO_2/Au	5–500	0.6	1132.8	[151]
	Graphene/ZnO	1000–15000	7.4357	3.2580 μAmM^{-1}	[159]
	rGO/Fe_2O_3	50-9000	6.0	-	[160]
	MnO_2/rGO	0.25–2245	0.071	-	[106]
	CuO/graphene	10–100	6.8		[161]
	MnO_2/Fullerene/graphene	2.0–8440	0.8	206.3	[156]

Non-enzymatic

Mn$_3$O$_4$-MnO$_2$/graphene	1–200	0.16	1443	[157]
Graphene/ZnO	1000–15000	-	0.055 uAmM^{-1}	[158]
CuO/polypyrrole/rGO	100-10000	0.03	-	[162]
CuO/rGO	1–6000	0.50	207.3	[163]
NiO-rGO-Nafion	0.6246–1050000.	0.03	2721	[94]
Glucose CuO/graphene	100–10500	0.008	1298.6	[145]
Mn$_3$O$_4$/graphene	2.5–529.5	1	101.1 uAmM^{-1}	[131]
CuO@graphene	0.5-6.5	0.05	-	[164]
Cu$_2$O/rGO	-	0.1	-	[165]
Fe$_3$O$_4$@graphene/Nafion	0.02–130	0.007	-	[135]
NiO-CuO/graphene	0.5–20	0.17	9.4055	[170]
Dopamine (DA) Graphene/ZnO	3-330	1.08	-	[172]
Fe$_3$O$_4$/graphene	0.01-100.55	0.007	3150	[38]

	ZnO-rGO	0.1-100 ; 200-1800	0.063	-	[92]
	Graphene/SnO$_2$	1-20	1	-	[168]
	Fe$_3$O$_4$-rGO	0.02–5.80	0.0065	-	[136]
	Graphene/SnO$_2$	0–50	1	-	[128]
	SnO$_2$/rGO	0.08-30	0.006	-	[169]
Acetaminophen	NiO-CuO/graphene	4–100; 100–400	1.33	618 ; 382	[170]
Tryptophan (Trp)	NiO-CuO/graphene	0.3–40	0.1	1123.8	[170]
Ascorbic acid (AA)	Graphene/ZnO	50–2350	3.71	-	[172]
	Graphene/SnO$_2$	100-1000	100	-	[168]
	Fe$_2$O$_3$/graphene	570–3970	0.543	-	[108]
Uric acid (UA)	Graphene/ZnO	1-70	0.33	-	[172]

		SnO$_2$/graphene	0.1–200	0.28	-	[171]
		rGO/ZnO	1-800	0.312	-	[91]
		Graphene/SnO$_2$	3–21	3	-	[168]
Enzymatic	Glucose	Fe$_3$O$_4$/chitosan/graphene	Up to 26000	16	5.658 mAcm^{-2}M^{-1}	[149]
		rGO/MnO$_2$/Au	15–845	1.8	83.7	[151]
		MnO$_2$/graphene	40-2000	10	3300	[104]
		rGO/ZnO/Ag	100-12000	10.6	-	[166]
		Ag-Graphene-TiO$_2$	-	-	12.2	[167]
	Cholesterol	CuO/graphene	100–800	78	-	[161]

2.6.2 Genosensor

ZnO is a semiconducting material that exhibits high surface area to volume ratio, high biocompatibility, high stability, biomimetic, less toxicity and good electron transferring feature, making it an attractive nanomaterial in the application of genosensing [173]. Kumar and coworkers [173] categorised graphene, carbon nanotubes, ZnO and gold as the "Elite Group of Nanomaterials", manifesting their attractive properties and amazing performance in electrochemical biosensing. In view of the remarkable properties of elite nanomaterials, Yang and colleagues [174] synthesised rGO/ZnO composites via co-electrodeposition and study the effect of morphology towards electrochemical performance. The variations in ZnO nanostructures were investigated using scanning electron microscopy (SEM), energy dispersive X-ray spectroscopy (EDS), X-ray powder diffractometry (XRD) and Raman spectroscopy (Figure 2.16). An electrochemical DNA sensor based on rGO-ZnO with nanowalls morphology was fabricated and upon differential pulse voltammetry (DPV) analysis, the proposed sensor displayed a low limit of detection (2.43×10^{-15} M).
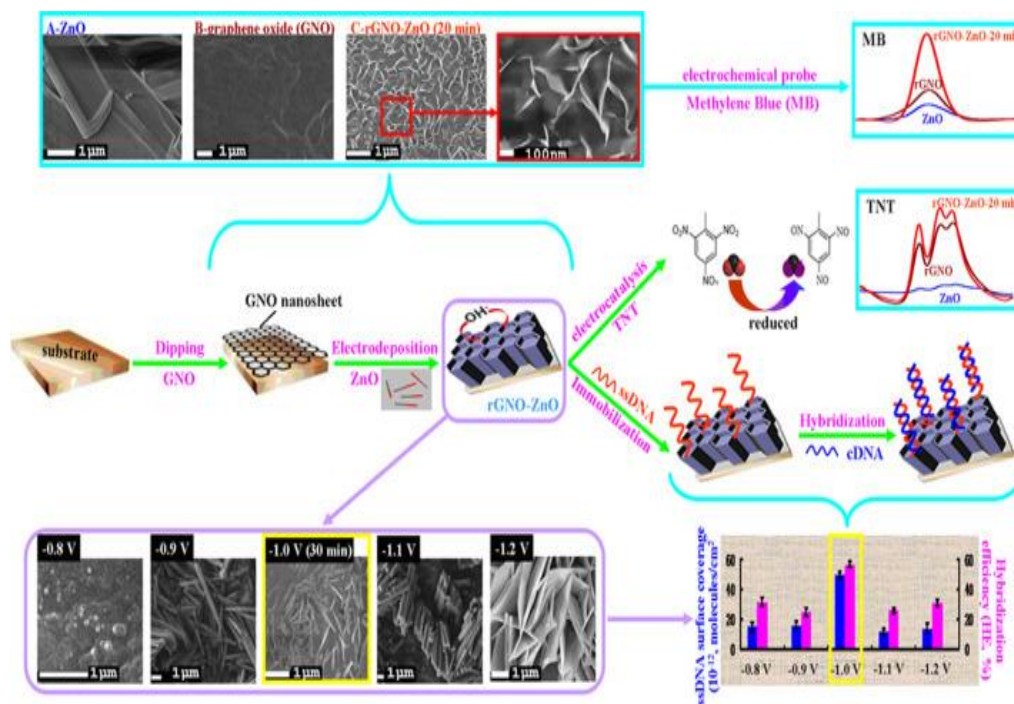
Figure 2.16: Schematic diagram representing the synthesis and electrochemical studies based on rGO/ZnO composite [174]. SEM results revealed that the rGO/ZnO composite deposited at -1.0 V showed homogenous distribution of ZnO with no agglomeration and the DPV tests showed good electrochemical performance.

The working principle of an electrochemical DNA biosensor can be based on the current signal generated by the oxidation of guanine and adenine. Kuralay et al. [175] reported on the interaction of anticancer drug (Mitomycin-C, MC) with DNA using TiO_2/graphene-modified pencil graphite electrode (PGE). MC bound to the DNA by shielding the oxidisable groups of DNA bases, resulting in decrease in the oxidation signals of guanine and adenine. The TiO_2/graphene-modified PGE exhibited a good linear range of 5 mgL^{-1} to 500 mgL^{-1} with detection limit of 1.25 mgL^{-1}. On the other hand, Ensafi et al. [176] reported on the detection of cytotoxic drug (furazolidone) using TiO_2/rGO-

modified electrochemical DNA biosensor. The proposed sensor displayed a good detection limit of 0.55 and 0.43 $pmolL^{-1}$ based on guanine and adenine signals, respectively. A chitosan-functionalised graphene/TiO_2 composite was applied to modify the carbon ionic liquid electrode for the detection of transgenic soybean sequence of MON89788 [177]. Methylene blue (MB) was used as a hybridisation indicator to investigate the hybridisation event between different ssDNA sequences. The electrochemical responses of MB was greatly increased due to the synergistic effects between TiO_2 nanorods and graphene, resulting in a good detection limit of 7.21×10^{-13} $molL^{-1}$.

A novel label-free electrochemical DNA biosensor based on a modified magnetic bar carbon paste (MBCPE) electrode with Fe_3O_4-rGO nanocomposite was reported as displayed in Figure 2.17 [152]. The bi-linker 1-pyrenebutyric acid-N-hydroxysuccinimide ester (PANHS) was applied to MBCPE/Fe_3O_4-rGO for the immobilisation of single stranded DNA probe. Cyclic voltammetry (CV) and electrochemical impedance spectroscopy (EIS) were used to characterise the electrochemical performance of the proposed sensor. Upon EIS measurement, different concentrations of complementary DNA strands were added to the MBCPE/FE_3O_4-rGO/PANHS/ssDNA electrode and a remarkable low detection limit was obtained (2.8×10^{-19} $molL^{-1}$). On the other hand, Zhang and coworkers [178] developed indicator-free electrochemical genosensor originated from the self-signal of poly-xanthurenic acid (PXa) enhance by Fe_3O_4/rGO composite. The pi-pi stacking and hydrogen bonding between Fe_3O_4/rGO composite and the aromatic ring of PXa promoted the

electropolymerisation efficiency, alongside with an increase in the electrochemical response of PXa, serving as a powerful tool in electrochemical genosensing. Chen and colleagues [179] also fabricate an electrochemical DNA biosensor based on three dimensional nitrogen-doped graphene and Fe_3O_4 nanoparticles. DPV was used to study the DNA hybridisation event with methylene blue as electrochemical indicator. Under optimal conditions, the proposed biosensor exhibited detection limit of 3.63×10^{-15} M with a linear range of 1×10^{-14} to 1×10^{-6} M.
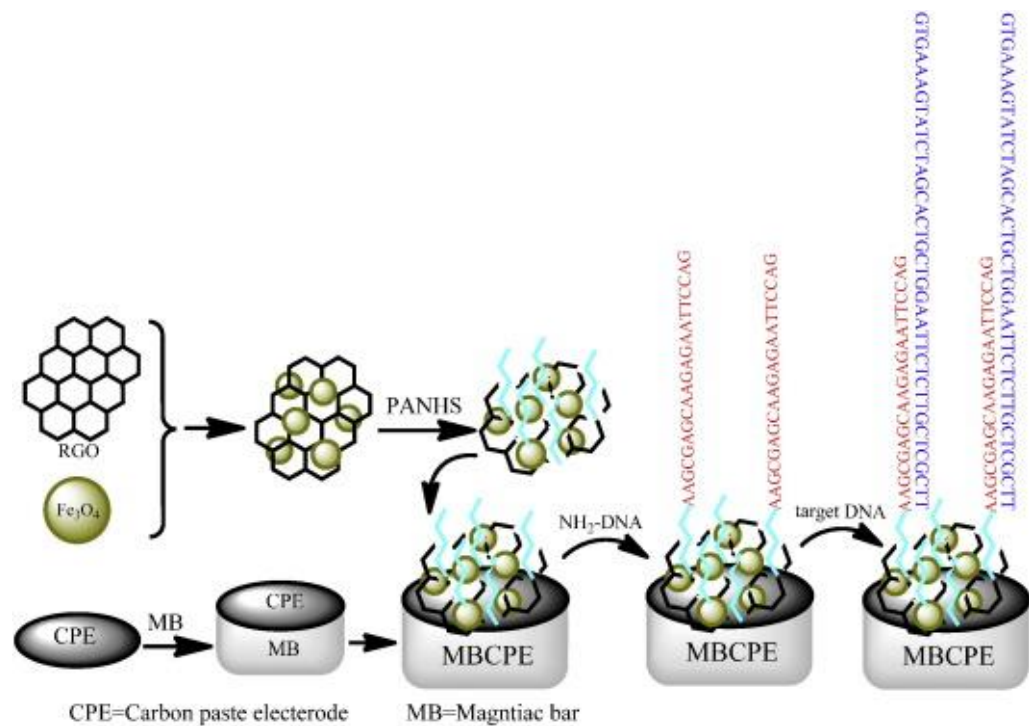
Figure 2.17: Schematic representation of the modified electrochemical biosensor based on MBCPE/Fe$_3$O$_4$-rGO/PANHS platform [152]. Reduced graphene oxide (RGO) was mixed with Fe$_3$O$_4$ to obtain Fe$_3$O$_4$-RGO composite, which was then functionalised with PANHS. The Fe$_3$O$_4$-RGO/PANHS composite was drop casted onto MBCPE to fabricate

MPCPE/Fe$_3$O$_4$-RGO electrode. The DNA probe was immobilised onto the electrode surface where target DNA was added for hybridisation.

2.7 Chapter Summary

This chapter presents the groundwork behind the motivation of this project, which is the development and establishment of a better, more efficient synthesis method for graphene/metal oxide composite that is safer and more environmental friendly, at the same time preserving the pristine nature of both graphene and metal oxide. Having discussed past research as well as the principles governing the main approaches in the synthesis of graphene/metal oxide composite, there is a necessity to improve the synthesis process in order to achieve efficient and safer production of graphene/metal oxide composite. A more detailed explanation of the proposed methodology in the synthesis of graphene/ZnO nanocomposite will be discussed in Chapter 4 and Chapter 5. This chapter also covers various functionalisation approaches that have been studied, demonstrating the pros and cons of each method for the functionalised graphene/metal oxide composite. The application of graphene/metal oxide composite in biosensing, particularly in the detection of biomolecules and DNA are discussed. The high sensitivity of graphene/metal oxide composite towards the detection of biomolecules such as H$_2$O$_2$ and glucose enables various sensing application of the composite. The applications of graphene/ZnO nanocomposite in the biosensing field will be discussed in Chapter 4 onwards. In the next chapter, various characterisation methods for

characterising the as-produced graphene/ZnO nanocomposite will be presented.

Chapter 3 Synthesis of Graphene/Zinc Oxide Nanocomposite for Application in Non-enzymatic Hydrogen Peroxide Sensing

3.1 Overview

The development of sensitive and precise detection method for hydrogen peroxide (H_2O_2) is vital and highly appreciable for biological, biomedicine, food security and environmental protection. Owing to its strong oxidising and reducing properties, H_2O_2 is an essential mediator in environmental, medical, food and industrial analyses. In living systems, H_2O_2 is the by-product of most electrochemical response of enzymatic processes, therefore, its detection is of special interest for tracking of biological targets such as glucose and lactose [180]. In addition, H_2O_2 can also generate reactive oxygen species (ROS), which in excess can lead to different kinds of diseases, for example Parkinson's, Alzheimer's, atherosclerosis, heart attack and more [181].

Numerous methods have been applied for the detection of H_2O_2, such as fluorometry [182, 183], chemiluminescence [184, 185], spectrophotometry [186] and titrimetry [187]. Nevertheless, these techniques are generally time and cost consuming. As an alternative, electrochemical technique has attracted much attention among the scientific community for its low cost, ease of miniaturisation, rapid response, high sensitivity and selectivity performance. Enzyme-based biosensors were fabricated to detect the reduction of H_2O_2 but

applications were limited by the relatively high cost, complication in enzyme immobilisation and crucial demands on environmental conditions [188].

With the development of nanoscience and nanotechnology, a solution was proposed using nonenzymatic artificial biosensor. Nanoparticles play an important role in improving the sensor performance, due to their high surface area to volume ratio, suitable biocompatibility, enhanced catalytic activity and good stability. In particular, zinc oxide (ZnO) is an imperative wide band gap semiconductor material and has great potential application in H_2O_2 sensing. Besides, ZnO is also popular in the field of biosensing because it is biocompatible, biodegradable, biosafe as it can be dissolved into mineral ions within a few hours [189].

On the other hand, two dimensional (2D) graphene sheet has intrigued enormous scientific activities due to its extraordinary properties since its discovery by Novoselov and colleagues in 2004 [5]. It is the thinnest and strongest material ever known, possessing outstanding optical, mechanical properties together with superior electrical and thermal conductivities due to its sp^2-hybridised carbon and electronic configuration [33].

Hybridisation of different materials enables the generation of composites with versatile and tailored-made properties, demonstrating desirable combinations that outperform the individual components [190]. Taking into account of the remarkable properties of graphene and ZnO, the generation of graphene/ZnO (G/ZnO) nanocomposite is hence anticipated to provide enhanced performances, like improved photocatalytic performance

[191], peculiar thermal stability [192] and outstanding electrochemical properties [193]. In fact, many researchers have attempted to synthesise and hybridise graphene with ZnO, hoping to generate composites with special features for sensing purpose. For instance, Kavitha and coworkers [194] demonstrated *in situ* generation of ZnO nanoparticles from zinc benzoate dihydrazinate complex onto graphene at 200 °C for the fabrication of electrochemical glucose biosensor. On the other hand, Palanisamy and coworkers [195] prepared the composite from electrochemically reduced graphene oxide and ZnO via electrodeposition for the purpose of fabricating enzyme-based biosensors. Similar attempt was performed by Xie and colleagues [184] by dropping chemically reduced graphene oxide and hydrothermally grown ZnO onto a glassy carbon electrode (GCE). The GCE was then dipped into gold nanoparticles solution and finally the enzyme, haemoglobin (Hb) was dropped onto the GCE surface for the fabrication of H_2O_2 biosensor.

Hitherto, most of the attempts in the synthesis of G/ZnO nanocomposite involved the *in situ* growth of ZnO and the reduction of graphene oxide. However, in most cases, the precursor; graphite or graphene oxide, was not completely reduced via chemical reaction, culminating in the presence of oxygenated functional group on the graphene surface. Moreover, chemically reduced graphene oxide faces the problem of contamination from excessive reducing agents, thereby affecting the purity of the composites [196]. Furthermore, the common method in preparing graphene is hazardous, as it

involves the usage of harsh chemicals such as fuming nitric acid and potassium permanganate or highly toxic reducing agents like hydrazine, dimethylhydrazine, hydroquinone and sodium borohydride ($NaBH_4$) [197]. In addition, the synthesis techniques mentioned are multi-step and time consuming. Thus, it is necessary to develop a reproducible, scalable framework for more environmental friendly synthesis method for G/ZnO nanocomposite. This chapter reports on a facile and green method for the preparation of G/ZnO nanocomposite and its characterisations. Furthermore, the electrochemical performance of the G/ZnO nanocomposite was investigated to demonstrate its feasibility for H_2O_2 sensing applications.

3.2   Experimental Details

3.2.1   Materials

Graphite flakes (99% carbon purity) were purchased from Bay Carbon (Michigan, USA). Ethanol was purchased from Merck. Zinc oxide (ZnO) nanoparticle powder (<100 nm, 99 % purity), uric acid, fructose, L-cysteine and phosphate buffer saline (PBS) pellet were purchased from Sigma Aldrich (St. Louis, USA). Hydrogen peroxide (H_2O_2, 30 %) was purchased from R&M Chemical. All the chemicals and reagent were used as received without any further purification. The deionised (DI) water (R ≥ 18.2 MΩcm) used in all experiments was produced by the Millipore system.

3.2.2 Preparation of Graphene Flakes

Graphene flakes were prepared via a single step approach by sonicating raw graphite in mixtures of ethanol and water [198]. Mixture of ethanol and deionised water (in the ratio of 2 to 3) was added into a beaker containing graphite and mixed well. The mixture was subjected to sonication using Elmasonic E30H (Germany) with a working frequency of 50/60 Hz for 3 hours to achieve exfoliation of graphite into graphene. The sonicated mixture was then centrifuged at 2500 rpm for 30 minutes to remove unexfoliated graphite flakes. The mixture was washed with ethanol and DI water repeatedly, followed by drying at 80 ^oC overnight to evaporate any ethanol residual.

3.2.3 Synthesis of Graphene/Zinc Oxide Nanocomposite

Overall, the procedures for the synthesis of G/ZnO nanocomposite are illustrated in Figure 3.1. Hybridisation of graphene and ZnO was prepared as follows: appropriate amount of the as-synthesised graphene, ZnO powders were dispersed in ethanol separately via sonication. The graphene and ZnO dispersions were mixed together and ultrasonicated for 15 minutes to achieve even mixing. The mixture was then stirred using mechanical mixing with the aid of magnetic stirrer. Next, the mixture was transferred for centrifugation at 2000 rpm for 30 minutes to remove any unbound particle and washed with ethanol and DI water. Lastly, the sediment was dried at 80 ^oC overnight to collect G/ZnO nanocomposite.
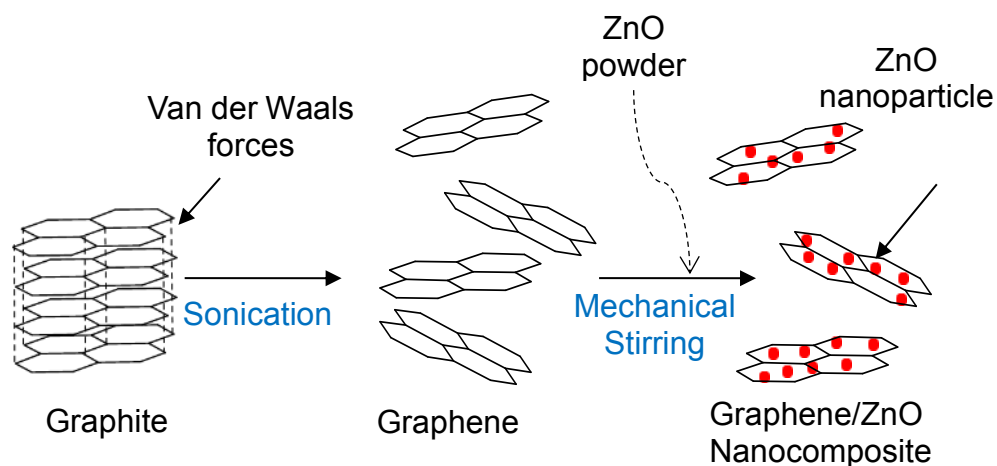
Figure 3.1: Schematic diagram of the synthesis of G/ZnO nanocomposite.

3.2.4 Instrumentation and Characterisation

The morphology of the sample was observed through scanning electron microscope (SEM) (FEI Quanta-400 FESEM, 20 kV) and transmission electron microscope (TEM) (JEOL JEM-2100 F). Energy dispersive X-ray spectroscopy (EDS) (Oxford Instruments X-Max, 20 mm^2 detector) was performed in conjunction with SEM to identify the elements present in the samples. The samples were deposited from ethanol dispersion onto silicon wafers (1 cm x 1 cm) and allowed to dry at ambient condition before subjecting to SEM and EDX analyses. X-ray diffraction (XRD) was used to characterise the crystallographic structures of the as-synthesised samples. The XRD analysis was performed on a diffractometer (X'pert Pro Powder, PANalytical) using a scan rate of 0.02 θs^{-1} in a 2θ range of 10-80° with Cu Kα radiation at λ = 1.5406 Å.

The electrochemical performances of the samples in connection with cyclic voltammetry (CV) were analysed using AUTOLAB PGSTAT302N at room temperature. The planar screen printed carbon electrode (SPCE) was fabricated

(ScrintTechnology, Penang, Malaysia) based on the design described by Chan et al. [199]. The disposable miniature SPCE consisted of a three-electrode configuration (19 mm x 40 mm), comprising of a round-ended carbon electrode (4 mm in diameter) serving as working electrode, carbon counter electrode and pseudo Ag/AgCl as the reference electrode, printed on a polycarbonate support as shown in Figure 3.2. A ring-shaped insulating layer around the round-ended working electrode (10 mm x 10 mm) with a capacity of 100 μL was incorporated onto the SPCE as an electrochemical cell (reservoir). The as-synthesised material dispersion was pipetted onto the surface of the working electrode of SPCE and air-dried. The SPCE was then washed with deionised (DI) water repeatedly to remove unbound material and air-dried. The material-modified electrode was then used in the electrochemical measurements. Cyclic voltammograms were recorded from -0.4 V to 0.4 V at a scan rate of 50 mV/s. Amperometry was used for the quantitative analysis of H_2O_2 [200].
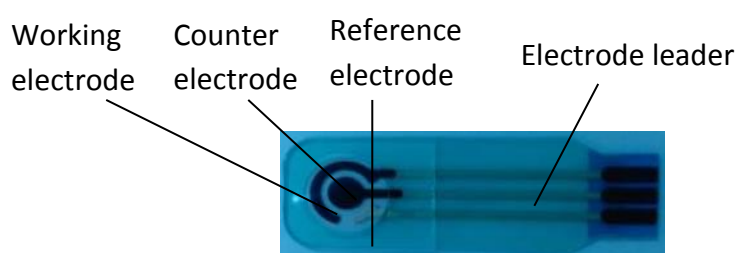
Figure 3.2: Screen printed carbon electrode (SPCE) detailing working, counter and reference electrode.

3.3 Results and Discussions

3.3.1 Optimisation of Experimental Conditions

3.3.1.1 Effect of Material Ratio

The effect of different material weight ratio towards the synthesis of G/ZnO nanocomposite was investigated. Table 3.1 shows detailed information of the different ratios of graphene to ZnO which were used in the preparation of G/ZnO nanocomposite. In order to examine the effect of different weight ratios, SEM was used to analyse the samples from different ratios that were drop casted onto silicon substrate.

Table 3.1: Variation of weight ratios of graphene to ZnO used in the preparation of G/ZnO nanocomposites.

Weight ratio of Graphene : ZnO	Mass of graphene (mg)	Mass of ZnO (mg)
1 : 0.1	100	10
1 : 0.5	100	50
1 : 1	100	100
1 : 5	100	500
1 : 10	100	1000

It can be observed from the SEM images in Figure 3.3 that higher weight ratio resulted in more ZnO nanoparticles being deposited onto graphene sheets. In Figure 3.3A, where 10 mg of ZnO mixed with 100 mg of graphene, resulted in limited amount of ZnO nanoparticles being deposited on the graphene

sheets. As the ratio of ZnO nanoparticles increases, it can be seen that more ZnO nanoparticles were deposited onto graphene sheets as shown in Figure 3.3B and Figure 3.3C. Further increment of ZnO nanoparticles resulted in agglomeration as shown in Figure 3.3D and Figure 3.3E. A similar morphology was reported by Gayathri and colleagues where increment of ZnO amount resulted in ZnO nanoparticle agglomeration [201]. Therefore, the weight ratio of 1:1 is chosen as the optimum ratio for the synthesis of G/ZnO nanocomposite.
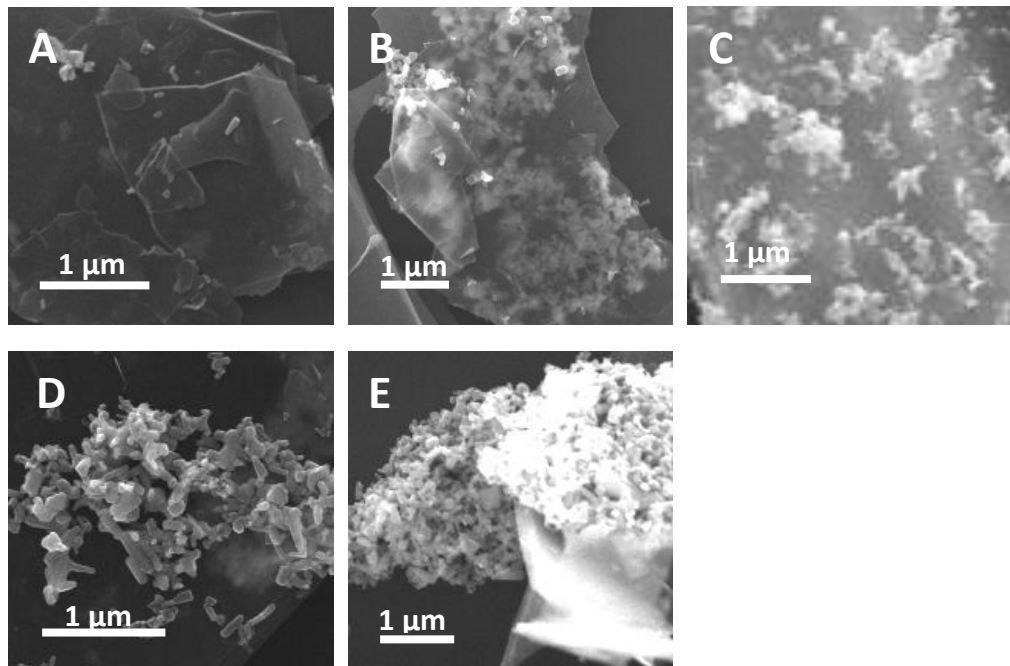
Figure 3.3: SEM images of G/ZnO nanocomposites synthesised in different weight ratios from (A) 1:0.1, (B) 1:0.5, (C) 1:1, (D) 1:5 and (E) 1:10.

3.3.1.2 Effect of Mixing Duration

The mechanical mixing duration was varied for the synthesis of G/ZnO nanocomposite. SEM analyses of samples mixed for 4 hours, 8 hours and 16 hours were performed as shown in Figure 3.4. It was observed that longer

mixing duration led to agglomeration of ZnO nanoparticle on the surface of graphene sheet as shown in Figure 3.4B (8 hours) and Figure 3.4C (16 hours). The result could be postulated to be due to the gradual change of the ZnO nanoparticles from soft agglomeration to hard agglomeration as suggested by Ishikawa and colleagues [202]. On the other hand, SEM analysis showed that at mixing duration of 4 hours, the ZnO nanoparticles were homogeneously distributed on the graphene sheets (Figure 3.4A). Therefore, the timepoint at 4 hours is chosen as the optimum mixing duration for the synthesis of G/ZnO nanocomposite.
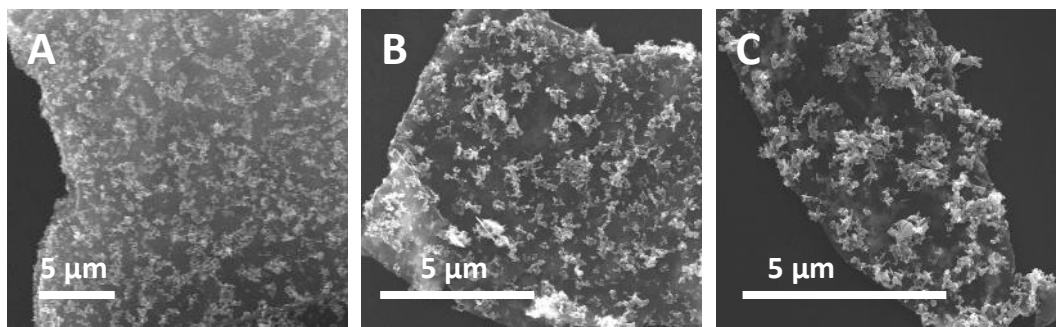
Figure 3.4: SEM images of the as-synthesised G/ZnO nanocomposites mixed for 4 hours (A), 8 hours (B) and 16 hours (C), respectively.

3.3.2 Characterisation of Graphene/Zinc Oxide Nanocomposite

In order to characterise and investigate the quality and exfoliation behaviour of graphite obtained in ethanol, the sonicated product was deposited onto silicon substrate which was then mounted onto carbon double sided tape for SEM and TEM analyses.

Graphene was successfully exfoliated from graphite under sonication in proper water-ethanol ratio, leading to the formation of few layer graphene

sheets, as clearly depicted in Figure 3.5A and Figure 3.5B. These images displayed that the as-exfoliated few layered graphene sheets are few micrometers in lateral size and the high transparency of the images attest to the few layer nature of the samples. In some cases, dark lines are observed which represent the folding or scrolling of the sheet edges, providing clear signature for the number of graphene layers [203]. The result obtained was in agreement with other findings in the production of solubilised graphene through liquid phase exfoliation of graphite as reviewed by Cui and colleagues [204].

Yi and colleagues [205] were the first to propose the idea of combining two mediocre solvents into a good solvent for exfoliating graphite by applying the principle of "like dissolves like" derived from the concept of Hansen solubility parameters (HSP) [206]. According to the dispersive, polar and hydrogen bonding parameters in the HSP theory, the HSP distance plays an important role in determining the efficiency of the exfoliation of inorganic graphene analogues. Hansen [206] stated that the lower the HSP distance, the higher the compatibility of the solvent system to bulk graphite. In the current work, the solvent mixture at a 40% ethanol/water ratio that had been previously optimised by Chia and colleagues [198] was adopted. Notably, this mixture used for the exfoliation of graphite is superior in terms of environmental friendliness and yield as compared with exfoliation using other chemicals. The utilisation of the optimum ratio mixture together with the shear waves generated by the collapse of the cavitation bubbles induced by

sonication shortened the synthesis duration and produced yield as high as 1 mg/ml.
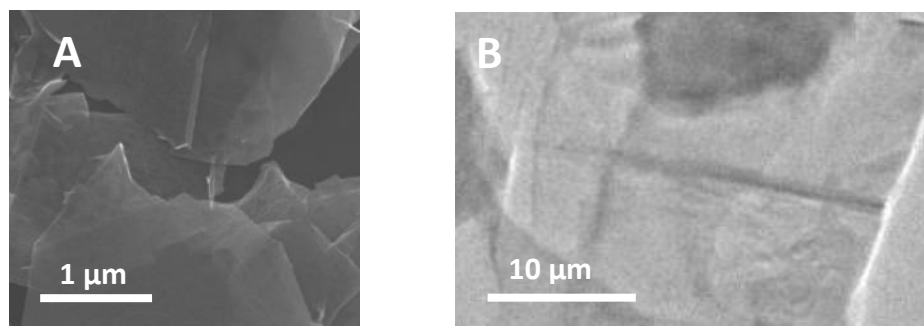
Figure 3.5: SEM (A) and TEM (B) images of the as-exfoliated graphene.

The detailed morphology of the G/ZnO nanocomposite structure was also studied through SEM and TEM and the micrographs are shown in Figure 3.6A and Figure 3.6B, respectively. Both SEM and TEM images clearly indicate that the nanocomposite composed of well spread two dimensional graphene sheets decorated with ZnO nanoparticles. The transparent nature of the graphene implies that it is fully exfoliated into single or few layer sheets, with ZnO nanoparticles observed to be confined in the graphene sheet. The quasi-spheric ZnO particles exhibited a narrow size distribution of around 20-40 nm and prevent the restacking of the hydrophobic graphene sheets. These nanosized ZnO particles were uniformly anchored on graphene and it should be stressed that no ZnO nanoparticles were observed outside of the graphene sheets, suggesting a successful hybridisation of G/ZnO nanocomposite.

To further confirm the chemical composition of the as-synthesized product, the compound was investigated by energy dispersive X-ray spectrometry (EDS) along with the SEM analysis. Figure 3.6C shows that the

product composed of carbon, zinc and oxygen, revealing the presence of zinc and oxygen component on the graphene sheet. In addition, the EDS spectrum showed no other elements besides the peak corresponding to silicon (Si) arose from the SEM specimen being drop casted onto silicon wafers, thereby confirming the chemical purity of the nanocomposite.
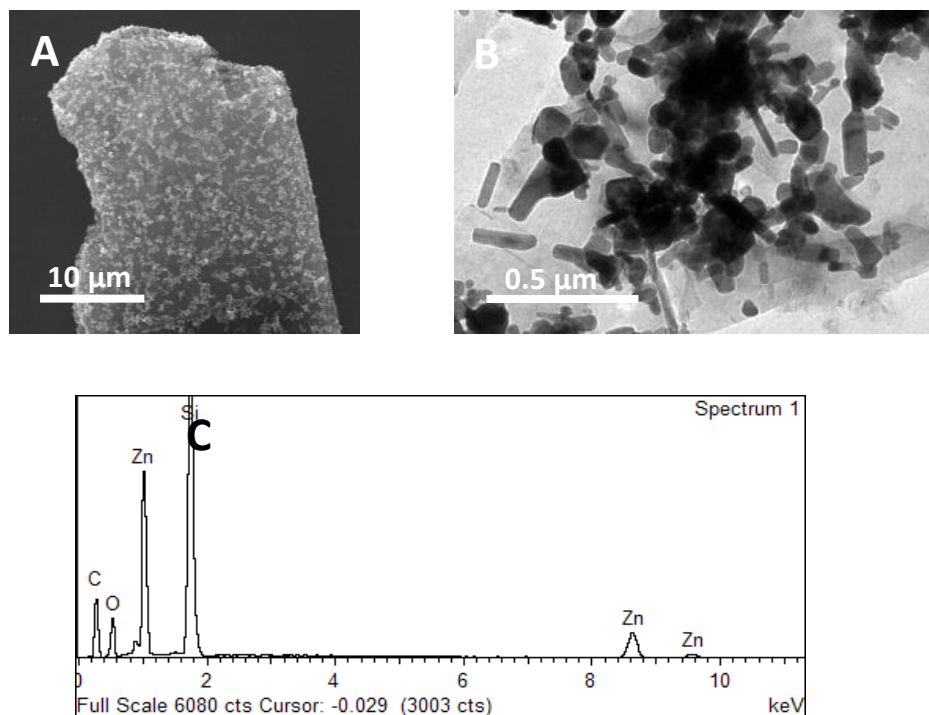
Figure 3.6: SEM (A) and TEM (B) images as well as EDS analysis (C) of the as-synthesised G/ZnO nanocomposite.

The XRD patterns of graphite, graphene and G/ZnO nanocomposite are shown in Figure 3.7. The two diffraction peaks observed in graphite, graphene and G/ZnO nanocomposite samples at 26.6° and 54.7° respectively, are attributed to the graphitic reflection of (002) plane (ICSD No. 98-005-2916). These results clearly indicate that the crystalline structure of the graphene was intact and its pristine nature was preserved, even after the formation of G/ZnO

nanocomposite. The XRD patterns of G/ZnO nanocomposite showed peaks at

2θ = 31.9°, 34.5°, 36.4°, 47.6°, 56.7°, 62.9°, 66.5°, 68.0° and 69.18°, which can

be indexed to ZnO crystal planes of (002), (202), (501), (640), (660), (901), (931),

(1000) and (941), corresponding to the wurtzite hexagonal structure of ZnO

(ICSD No. 98-006-5172) The diffraction peaks obtained are similar to that of

pure zinc oxide, indicating a successful synthesis of the nanocomposite with no

impurity.
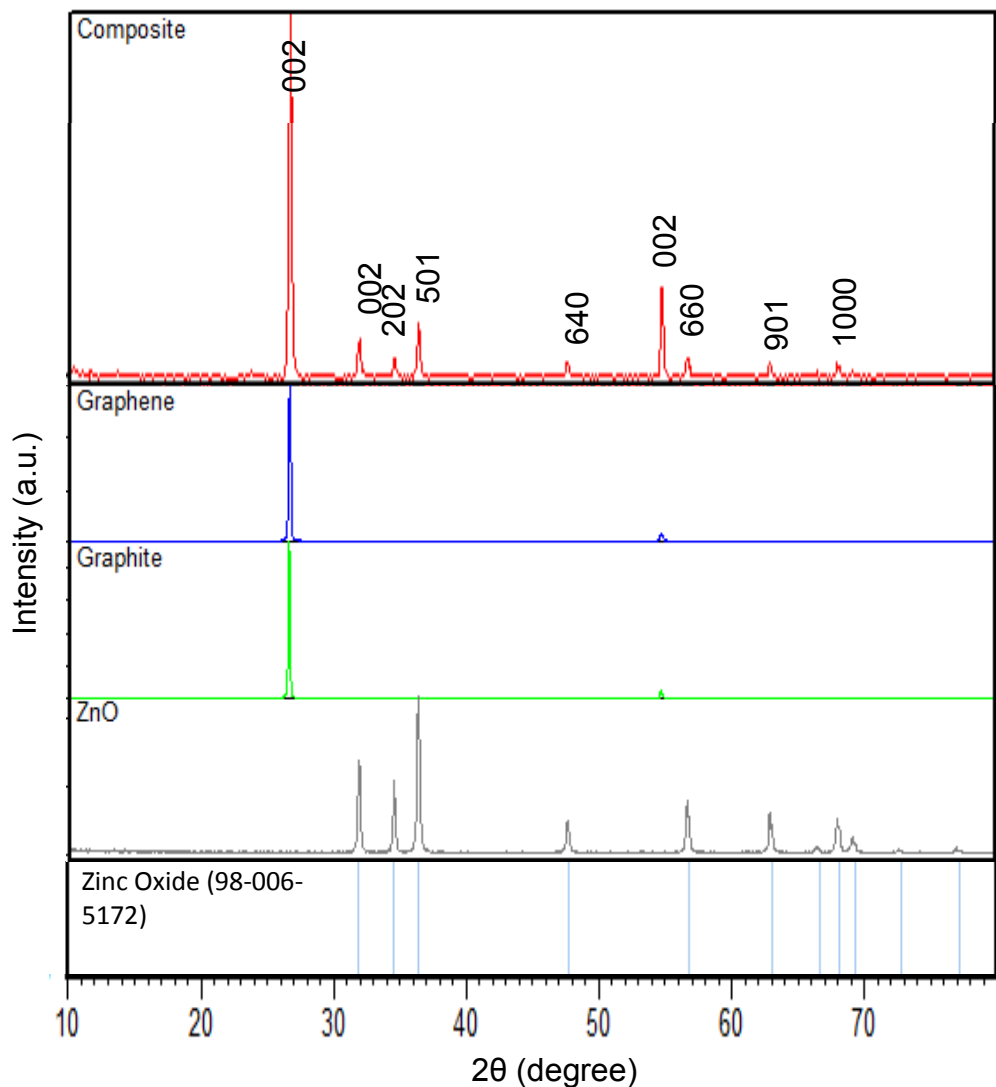
Figure 3.7: XRD patterns of graphite, graphene, ZnO and G/ZnO

nanocomposites in comparison with the standard reference pattern.

3.3.3   Electrochemical Analyses of Graphene/Zinc Oxide Nanocomposite

To discern the role of individual components and possible synergy between them, the amperometric response of the electrode modified with graphene, ZnO and G/ZnO nanocomposites, respectively, were studied as shown in Figure 3.8.

Figure 3.8 shows a significant increase in peak current of almost 3.5 times in the CV response of the G/ZnO nanocomposite-modified SPCE (curve d) as compared to CV response of bare SPCE (without modification, curve a). In addition, Figure 3.8 also affirms that the hybridisation of graphene and ZnO nanoparticles possessed enhanced properties as the G/ZnO nanocomposite-modified SPCE (curve d) showed a greater increment in terms of electrochemical performance than their individual counterparts (curve b & c). This indicates the presence of synergistic effect between graphene and ZnO nanoparticles, in which the carbon-based material acts as a good electron conductor and when coupled with a metal oxide, the charge transfer between the materials is improved, thereby achieving enhanced catalytic properties.
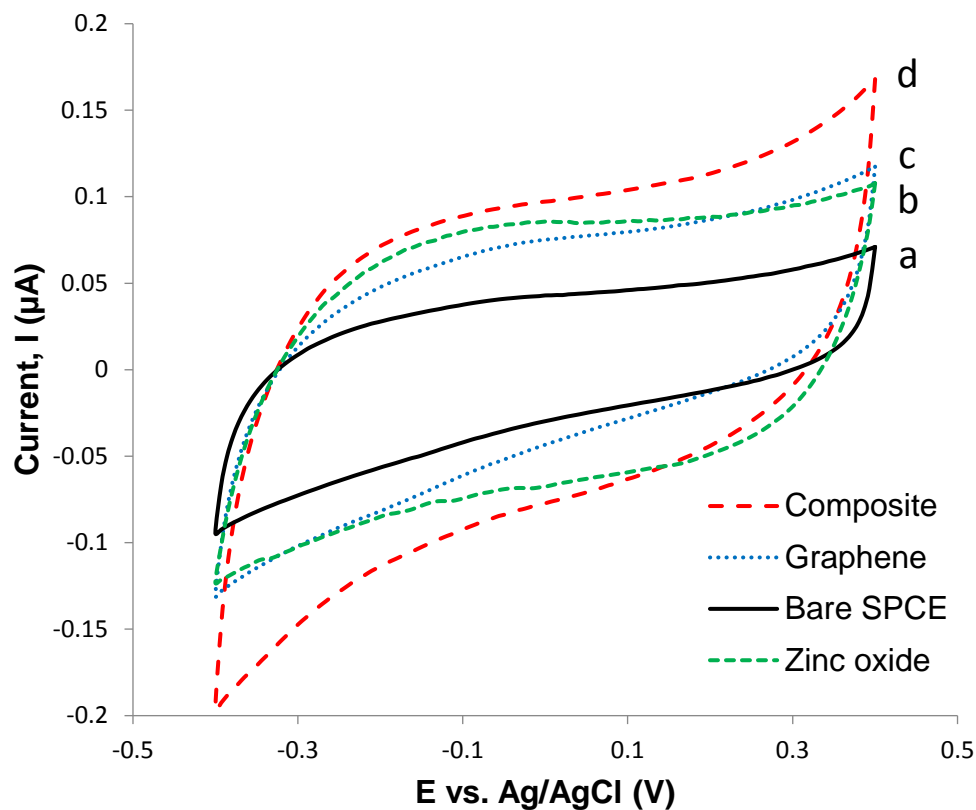
Figure 3.8: Cyclic voltammograms of bare SPCE (a), ZnO- (b), graphene- (c) and G/ZnO nanocomposite- (d) modified SPCE in blank PBS buffer.

3.3.3.1 Effect of Hydrogen Peroxide Concentration

Hydrogen peroxide (H_2O_2) was generally employed as model reaction for experiments as it is the by-product of most enzymatic processes and thus, assessing the sensitivity of sensor towards the detection of H_2O_2 would be of notable value. The CV responses of G/ZnO nanocomposite-modified SPCE in different concentrations of H_2O_2 were investigated.

As shown in Figure 3.9, the cathodic peak current (I_{pc}) increased gradually upon increasing the concentration of H_2O_2 from blank, 1 µM, 2 µM, 3 µM, 4 µM, 5 µM, 6 µM, 7 µM and 8 µM (curves a-i). This non-enzymatic H_2O_2

sensor assesses the maximum catalytic current to ascertain its sensing capability as the redox peaks for H_2O_2 occur at very high switching potentials [207]. The linear relationship between cathodic peak current and H_2O_2 concentration can be rationalised by considering the availability of the amount of H_2O_2 molecules present in the PBS buffer. Higher H_2O_2 concentration consists of more H_2O_2 molecules involving in the redox reaction, it also meant that more electrons were involved in the electron transfer process, thereby resulting in a higher cathodic peak. The linear regression equation is I (μA) = 0.015C (μM) + 0.1493, R^2 = 0.9816 as displayed in Figure 3.9 inset.

Overall, the enhanced sensing performance of G/ZnO nanocomposite can be plausibly attributed to the synergistic influence between graphene sheets and ZnO nanoparticles. The high electrocatalytic activity can also be ascribed to the large surface area-to-volume ratio of the graphene and also the porous nature together with the typical flower-like microstructure of the ZnO nanoparticles, providing more catalytic sites for efficient diffusion of analytes [195].
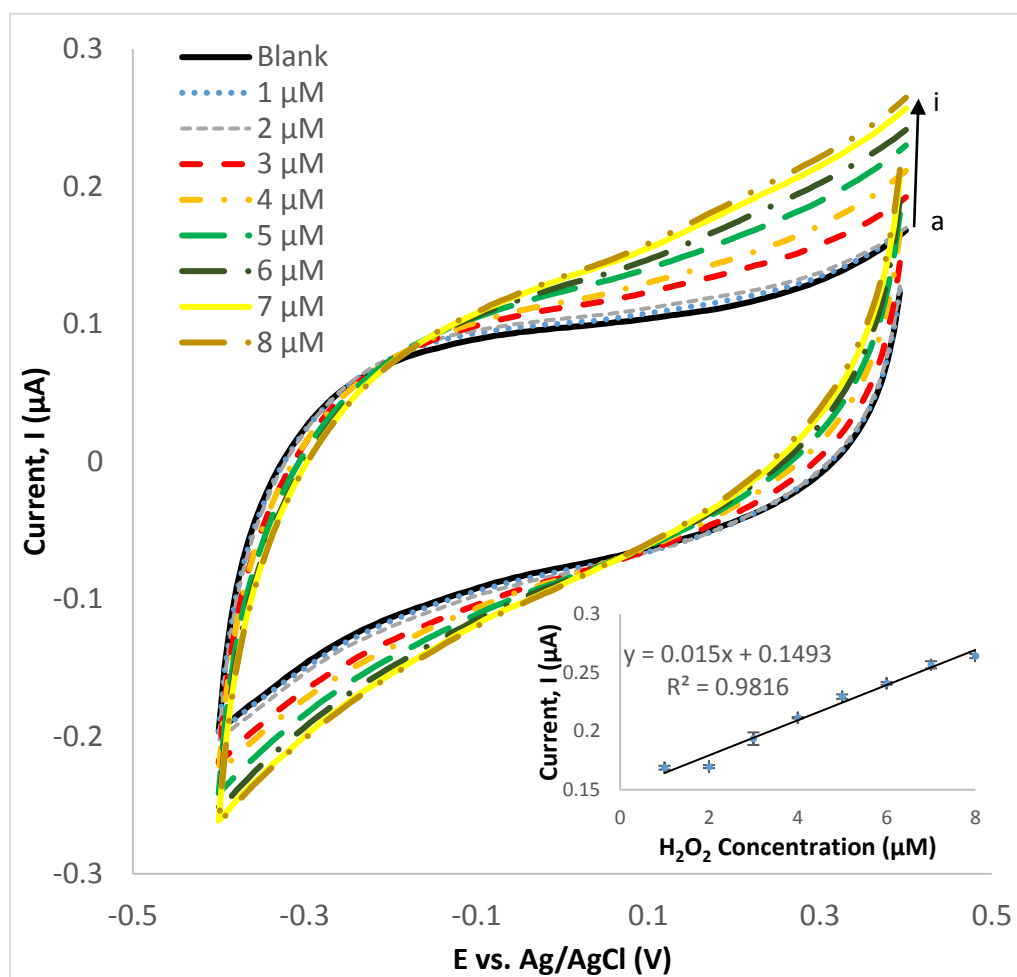
Figure 3.9: Cyclic voltammograms of G/ZnO nanocomposite-modified SPCE in the absence (a) and presence of 1 µM (b), 2 µM (c), 3 µM (d), 4 µM (e), 5 µM (f), 6 µM (g), 7 µM (h) and 8 µM (i) of H₂O₂. Inset is the plots of cathodic peak current against H₂O₂ concentration.

3.3.3.2 Effect of Scan Rate

Figure 3.10 shows the CVs obtained with G/ZnO nanocomposite-modified SPCE in pH 7.4 PBS buffer with varying scan rates from 10 mV/s to 100 mV/s. In general, both anodic peak current (I_{pa}) and cathodic peak current (I_{pc}) increased gradually when higher scan rates were applied. The plots for anodic

(I_{pa}) and cathodic (I_{pc}) peak currents against scan rates are shown in Figure 3.10 inset, exhibiting linear relationship with R^2 = 0.9929 and 0.9809, respectively, demonstrating that the redox reaction occurring is a surface-confined and controlled diffusion process [208]. Besides, the linear relationships between the peaks currents and scan rate also showed the characteristics of thin layer electrochemical behaviour. Notably, the maximum peak currents always occur at the same voltage regardless of the scan rate applied, indicating reversible electron transfer kinetics of the electrode.
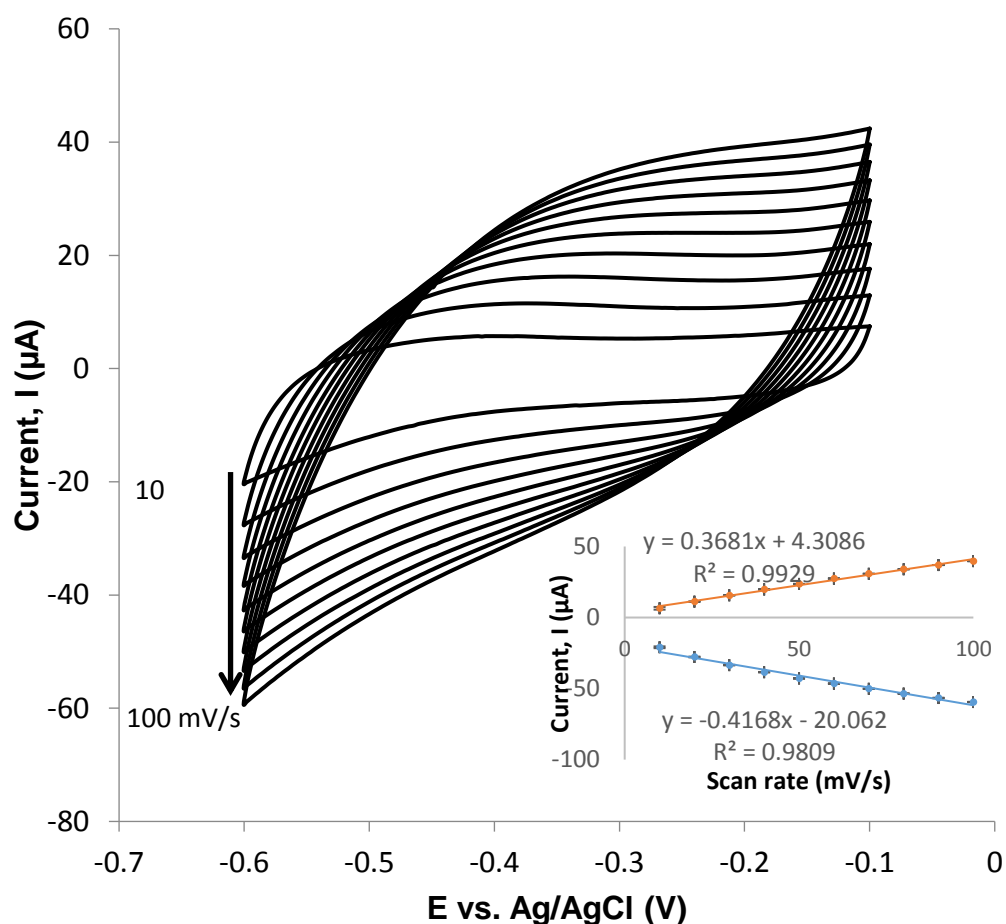
Figure 3.10: Cyclic voltammograms of G/ZnO nanocomposite-modified SPCE in pH 7.4 PBS buffer at different scan rates. The scan rates from inner to outer are 10, 20, 30, 40, 50, 60, 70, 80, 90 and 100 mV/s, respectively. Inset

shows the linear dependence of anodic (I$_{pa}$) and cathodic (I$_{pc}$) peak current against scan rates.

3.3.3.3 Real Time Amperometric Detection of Hydrogen Peroxide

Amperometry was employed in this study to evaluate the electrocatalytic activity of the developed G/ZnO nanocomposite-modified SPCE. During the real time amperometric measurements, the operating potential was hold at 0.4 V and PBS buffer was constantly stirred at 900 rpm. For every 50 s, aliquots of H_2O_2 were successively injected into the supporting electrolyte solution (PBS buffer).

Figure 3.11 shows the steady state amperometric response obtained at G/ZnO nanocomposite-modified SPCE upon addition of various H_2O_2 concentrations in the range of 1 to 15 mM. The calibration curve for H_2O_2 was obtained by measuring the changes in current with each addition of 1 mM H_2O_2 (Figure 3.11 inset). It can be seen from the calibration curve that the current increases linearly with the increase of concentration of H_2O_2. The linear regression equation is I (μA) = 0.0548 C (mM) + 0.0547 with the correlation coefficient (R^2) of 0.9859, which permits reliable quantification of the content of H_2O_2 in a sample. The limit of detection (LOD) of the G/ZnO nanocomposite-modified electrode was 1.663 x 10^{-9} M (S/N = 3) with a sensitivity of 0.055 μA/mM, showing improvement as compared to the sensitivity (0.022 μA/mM) obtained from graphene-modified SPCE [198] (Calculation of the limit of detection is shown in Appendix I). These results clearly showed that the G/ZnO

nanocomposite-modified sensor exhibits fast and well defined response towards each H_2O_2 additions.
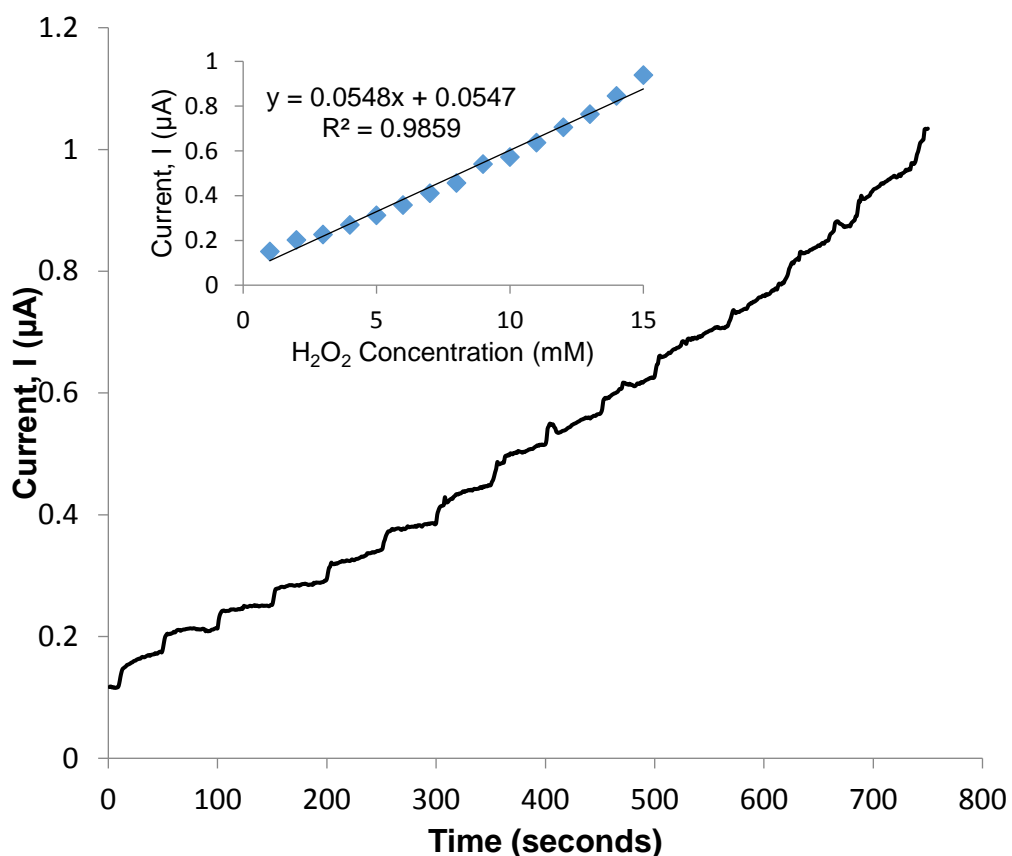
Figure 3.11: Amperometric *i-t* response of G/ZnO nanocomposite-modified SPCE for the addition of different H_2O_2 concentrations into PBS buffer with the applied potential of 0.4 V. Inset is the plot of concentration of H_2O_2 versus current in the linear range.

3.3.3.4 Stability and Selectivity Study

The stability of G/ZnO nanocomposite-modified SPCE was also examined during storage in a dry state at ambient temperature. It was found that the current response remained nearly 93% of its initial value over 4 weeks, validating the good stability of the nanocomposite. The long-term stability can

be plausibly attributed to the well anchored ZnO nanoparticles onto the exfoliated graphene sheets and the strong synergistic effect between graphene and ZnO. The background current retained 95% stability even after 200 consecutive cycles, authenticating the excellent stability of the graphene/ZnO nanocomposite.

The effect of co-existing electroactive species towards the selectivity of the G/ZnO nanocomposite-modified sensor was investigated. The influence from common interference species such as uric acid, fructose and L-cysteine was investigated. As shown in Figure 3.12, for each addition of 1 μM H_2O_2, the biosensor showed quick response. On the other hand, no noteworthy response was observed for the addition of 1 mM uric acid, fructose and L-cysteine. Each addition of the electroactive interfering species resulted in a hardly discernible current response, suggesting that the interfering effect caused by these electroactive species is quite negligible. The result also validates the highly selective detection of H_2O_2 at the G/ZnO nanocomposite-modified SPCE.
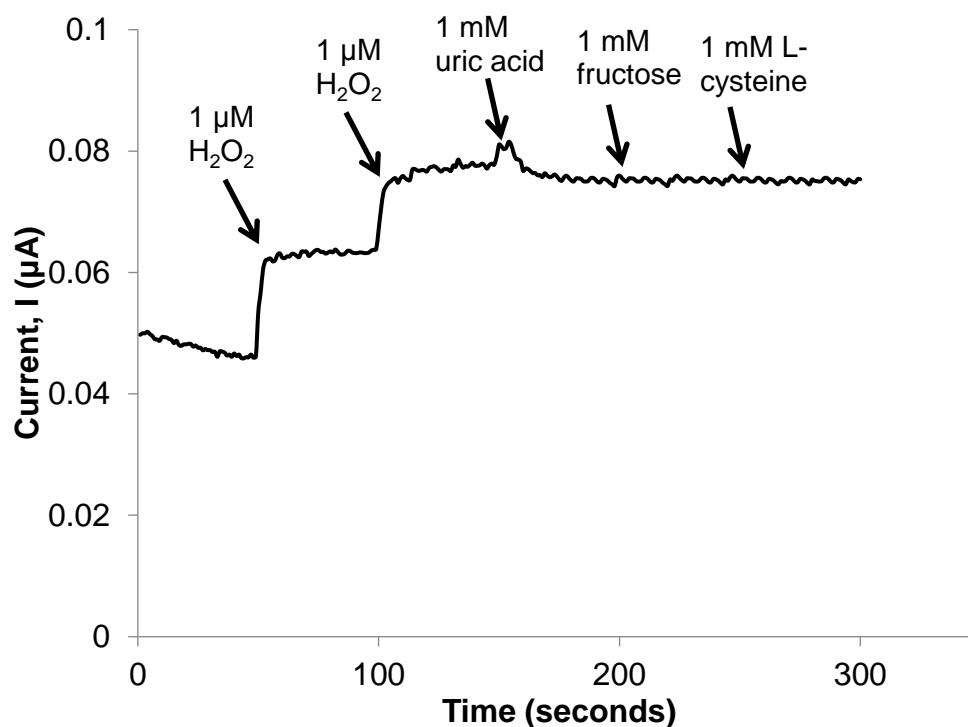
Figure 3.12: Amperometric *i-t* response of G/ZnO nanocomposite-modified SPCE for the successive addition of 1 μM H₂O₂, 1 mM uric acid, 1 mM fructose and 1 mM L-cysteine solutions into continuously stirred PBS buffer.

3.4   Chapter Summary

In this chapter, the ability to replace reduction of graphene oxide with a one step, facile and method green in the synthesis of G/ZnO nanocomposite has been demonstrated. The results of varying the key parameters in G/ZnO nanocomposite synthesis were also studied and discussed. The parameters that were optimised include different graphene to ZnO ratios and different mixing durations. The results showed that the synthesis of graphene/ZnO nanocomposite is more desired without the addition of surfactant, at a ratio of 1:1 and mixing duration of 4 hours.

This method yields G/ZnO nanocomposites with high purity and well-preserved crystallinity, which are affirmed by the results obtained in SEM, EDS, TEM and XRD. In addition, the as-synthesised G/ZnO nanocomposites show promising applicability as an effective sensing platform for the detection of hydrogen peroxide molecules with a limit of detection of 1.663×10^{-9} M (S/N = 3) (Calculation of the limit of detection is shown in Appendix I). The detection of hydrogen peroxide was sensitive up to a maximum of 0.055 µA/mM, displaying almost 3.5 times of improvement as compared to the control electrode. These results clearly indicate that the G/ZnO nanocomposite-modified electrodes displayed a marked increase in signal response if compared to unmodified electrodes, as evidenced by the electrochemical measurements.

However, this approach still leaves much room for improvement, and the following chapter discusses an efficient approach to synthesise G/ZnO nanocomposite with improved catalytic properties.

Chapter 4 Synthesis   of   Graphene/Zinc   Oxide Nanocomposite via Low Temperature Hydrothermal Growth

4.1 Overview

Chapter 4 illustrates the efforts to develop a simple and green synthesis approach for graphene/zinc oxide (G/ZnO) nanocomposites to be used in the fabrication of non-enzymatic hydrogen peroxide (H_2O_2) sensor. While the synthesis approach is simple by mechanically mixing graphene and zinc oxide (ZnO) nanoparticles to produce G/ZnO nanocomposite, the attraction force between graphene sheets and zinc oxide nanoparticles is relatively weak. Therefore, in this chapter, another synthesis approach, i.e. low temperature hydrothermal growth for the synthesis of G/ZnO nanocomposites was enlisted.

Many synthesis routes have been developed for the hybridisation of graphene and ZnO nanoparticles. For example, Bu [209] demonstrated the synthesis of reduced graphene oxide/aluminium doped zinc oxide nanocomposite via reduction of graphene oxide in a vacuum furnace set at 700 °C under hydrogen flow and mixed with the aluminium doped zinc oxide solution. However, these synthesis method utilising high temperature might impose danger to the handler and it is not environmental friendly. Other synthesis methods involved synthesising graphene via modified Hummers method or hydrazine reduction [195, 210]. The usage of harsh and toxic chemicals in the reduction of graphene oxide often culminates in the generation of oxygenated functional group on the reduced graphene oxide.

These impurities will affect the superior electrical conductivity of the graphene. Therefore, a safer and more robust synthesis method is crucial to fully harvest the remarkable property of graphene for the production of G/ZnO composite material with optimal synergistic properties.

In this work, an economical and safe method via one step facile solvent exfoliation was used to synthesise the graphene material prior to the incorporation of ZnO precursor for the production of G/ZnO nanocomposite via a low temperature solvothermal synthesis method. The proposed method ensures the preservation of the pristine quality of graphene, in addition to being safer and more economical to produce the G/ZnO nanocomposite material. The electrochemical performance of the G/ZnO nanocomposite synthesised through this method was also studied to evaluate its potentiality for the fabrication of sensitive H_2O_2 sensing platform.

4.2   Experimental Details

4.2.1   Materials

Graphite flakes (99 % carbon purity) were purchased from Bay Carbon (Michigan, USA). Zinc nitrate hexahydrate ($Zn(NO_3)_2 \cdot 6H_2O$, 98 % reagent grade), sodium hydroxide (NaOH), uric acid, fructose and glucose were bought from Sigma Aldrich (St. Louis, USA). Ethanol was obtained from Merck (Darmstadt ,German), hydrogen peroxide (H_2O_2, 30 %) was purchased from R&M Chemical (Selangor, Malaysia). All chemicals were used as received and deionized water (DI) from the Millipore system was used throughout the experiment. Phosphate buffer solution (PBS) tablets were purchased from

Sigma Aldrich (St. Loius, USA) and dissolved in DI water to produce 0.1 M buffer solution with pH of 7.4.

4.2.2 Synthesis of Graphene

The preparation of graphene has been discussed in Section 3.2.2. In brief, graphite flakes was sonicated in ethanol and DI water (2:3 ratio) mixture, which was then subjected to centrifugation and dried overnight to obtain graphene.

4.2.3 Synthesis of Graphene/Zinc Oxide Nanocomposite

Graphene/ZnO nanocomposite was prepared through one step green low temperature hydrothermal growth as displayed in Figure 4.1 [138]. The as-synthesised graphene was re-dispersed in ethanol via sonication for 30 minutes. Appropriate amount of zinc nitrate hexahydrate was added into the graphene dispersion and stirred for 15 minutes to achieve even mixing. Different mass ratios of graphene to zinc nitrate hexahydrate were used as shown in **Error! Reference source not found.** to determine the optimum ratio. Diluted sodium hydroxide (NaOH) solution was then added to adjust the graphene and zinc nitrate hexahydrate mixture to a pH value of 12. The mixture was then transferred to a 50 ml Teflon stainless steel autoclave and heated at 90 °C for 10 hours. The supernatant was removed by centrifugation and the solid precipitates were washed repeatedly with excess ethanol and water, respectively, and dried overnight at 80 °C to collect the graphene/ZnO nanocomposite.
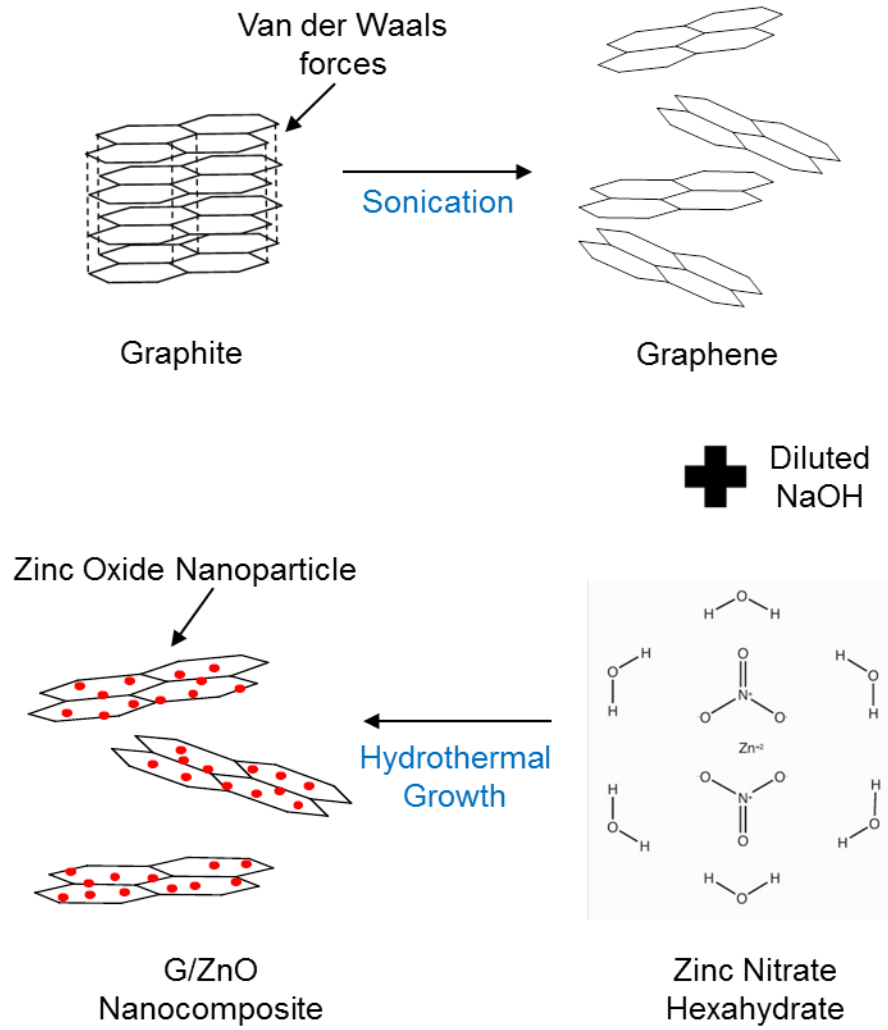
Figure 4.1: Schematic diagram of the synthesis of graphene/zinc oxide

(G/ZnO) nanocomposite via low temperature hydrothermal growth.

Table 4.1: Variation of mass ratios of graphene to zinc oxide precursor used in the synthesis of G/ZnO nanocomposites.

Weight ratio of Graphene : ZnO precursor	Mass of graphene (g)	Mass of ZnO precursor (g)
1 : 1	0.2	0.2
1 : 2	0.2	0.4
1 : 8	0.2	1.6
1 : 16	0.2	3.2

4.2.4 Instrumentation and Characterisation

The instrumentations for the characterisation of as-synthesised G/ZnO nanocomposite have been discussed in Section 3.2.4. In brief, the as-synthesised G/ZnO nanocomposite was characterised using SEM, TEM, EDX and XRD. The Raman spectra on the powdered samples of graphene and G/ZnO nanocomposite were recorded on a Renishaw inVia Raman microscope at room temperature. The system is equipped with a charge coupled device (CCD) detector and a holographic notch filter, using a 514 nm diode laser excitation source with power below 0.5 mW.

Screen printed carbon electrode (SPCE) (DropSens, Spain) (Figure 4.2) was employed in this study to evaluate the electrochemical performance of the as-synthesised materials. The preparation of G/ZnO nanocomposite-modified SPCE has been discussed in Section 3.2.4. Cyclic voltammograms were recorded

from -0.4 V to 0.8 V at a scan rate of 50 mV/s. One-way analysis of variance (ANOVA) was used to evaluate the performance of G/ZnO nanocomposite-modified SPCE. Differences were considered significant at $P < 0.05$.
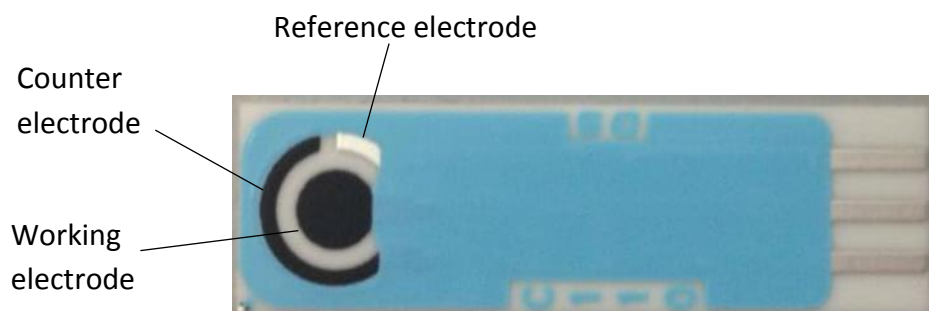
Figure 4.2: Screen printed carbon electrode (SPCE) detailing working, counter and reference electrodes.

4.3   Results and Discussions

4.3.1   Structural and Morphological Characterisation

The effect of different mass ratio of graphene to zinc precursor used in the synthesis of G/ZnO nanocomposite was characterised via SEM (Figure 4.3A to D). It was observed that with an increase in the loading mass of zinc precursor, more ZnO nanoparticles were formed on the surface of graphene sheets. For G/ZnO nanocomposites with mass ratio of 1:1 and 1:2 (Figure 4.3A and B), it was seen that the ZnO nanoparticles were not homogenously distributed on the graphene surface. On the other hand, ZnO nanoparticle agglomerates were found on the graphene surface in Figure 4.3D, in which these aggregates might form non-conducting layers and thus affecting the conductivity property of the composite [138]. Figure 4.3C shows that ZnO nanoparticles were uniformly formed on the surface of graphene sheets,

indicating that the G/ZnO nanocomposite synthesised from the mass ratio of 1 : 8 was desirable. The ZnO nanoparticles formed on the graphene sheet were spherical in shape with diameter around 200 nm.

TEM analysis (Figure 4.3E and F) was performed to supplement the evidence of exfoliation of graphite and formation of ZnO on the graphene sheets. The TEM results manifest the transparent nature of the as-synthesised graphene, indicating graphite was exfoliated into thin sheets. Furthermore, following the optimum mass ratio observed through SEM, TEM result also displayed homogenous deposition of ZnO nanoparticles on the surface of the graphene sheets, complementing the SEM result.

The formation of ZnO nanoparticles from precursor can be illustrated from Equations (4.1) – (4.3). Sodium hydroxide (NaOH) reacts rapidly with zinc nitrate hexahydrate ($Zn(NO_3)_2 \cdot 6H_2O$) to generate $Zn(OH)_2$ colloids as shown in Equation (4.1), part of the $Zn(OH)_2$ dissolves into Zn^{2+} and OH^- ions during the process as indicated in Equation (4.2). Lastly, ZnO nuclei are formed when concentration of the ions reaches supersaturation degree of ZnO according to Equation (4.3). The ZnO nuclei grow larger along the planes and edges of graphene sheets to form the G/ZnO nanocomposites.

$$Zn(NO_3)_2 + 6H_2O + 2NaOH => Zn(OH)_2 + 2NaNO_3 + 6H_2O \quad \text{Equation (4.1)}$$

$$Zn(OH)_2 + 2H_2O => Zn^{2+} + 2OH^- + 2H_2O => Zn(OH)_4^{2-} + 2H^+ \quad \text{Equation (4.2)}$$

$$Zn(OH)_4^{2-} => ZnO + H_2O + 2OH^- \quad \text{Equation (4.3)}$$
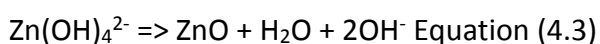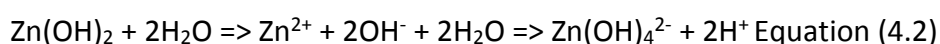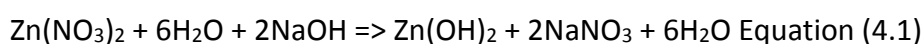
In general, a larger ZnO crystal is a polar crystal whose positive polar plane is rich in Zn and the negative polar plane is rich in O. In the hydrothermal growth process, the growth unit of ZnO is $[Zn(OH)_4]^{2-}$, which leads to different growth rate of planes as reported by Wu and colleagues [211]. The growth rates of different planes are shown as follows:

$$V(0001) > V(01\bar{1}\bar{1}) > V(01\bar{1}0) > V(01\bar{1}1) > V(000\bar{1})$$

Plane disappears quicker as the growth rate increases [212]. Therefore, the most rapid growth rate plane will disappear in the hydrothermal growth process, leading to the formation of rod-like shape ZnO nanoparticles. However, at high reaction temperature (more than 90 °C), heat convection, deregulation movement among molecules and ions in the solution become intense and the deposit rate of the growth unit $[Zn(OH)_4]^{2-}$ on ZnO nuclei became more rapid. Referring to the growth rule mentioned, the second rapid growth rate plane, $(01\bar{1}1)$ may be grown slower than $(01\bar{1}0)$ plane. Therefore, the $(01\bar{1}0)$ plane extrudes and displays as quasi-spherical particles, as shown in Figure 4.3F.

The chemical composition of the as-synthesised product was analysed via energy dispersive X-ray spectrometry (EDS) as shown in Figure 4.3G. The peaks of C, O and Zn in the spectrum depict the presence of carbon, oxygen and zinc compound only, thereby further affirming the purity of the product. The peak corresponding to silicon (Si) was due to the specimen being drop casted onto silicon substrate for characterisation.
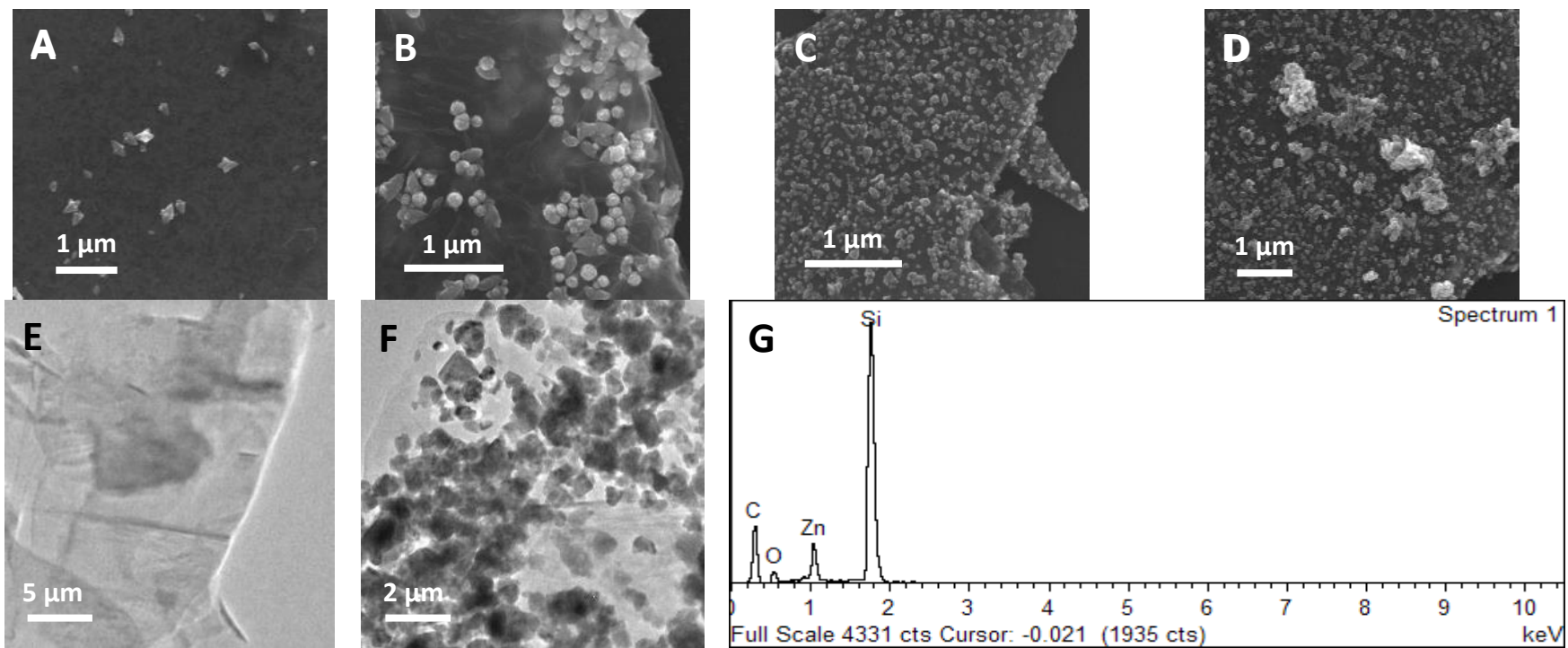
Figure 4.3: SEM images of G/ZnO nanocomposites synthesised in different weight ratios from (A) 1:1, (B) 1:2, (C) 1:8 and (D) 1:16; TEM images of (E) graphene and (F) G/ZnO nanocomposite (1:8); (G) EDS analysis of G/ZnO nanocomposite (1:8).

The XRD patterns of the raw graphite, as-exfoliated graphene, ZnO and as-synthesised G/ZnO nanocomposites are shown in Figure 4.4. The diffraction peaks at 26.63° and 54.71° for graphite and graphene are similar, accounting for the graphitic reflection of (002) plane, which correspond to a d-spacing of 3.34Å (ICSD no. 98-005-2916). This result indicated that the sonochemical method employed for the exfoliation of graphite did not disrupt the pristine crystalline structure, preserving the intact lattice structure of the exfoliated graphene. This differs from graphene synthesised via chemical routes which involves reduction through harsh acid mixture that culminates in structural defects, affecting the properties of the materials. The peaks at $2\theta = 32.07°$, 34.80°, 36.55°, 47.80°, 56.88°, 63.14°, 66.74° and 68.26° can be indexed to the characteristic ZnO crystal planes of (001), (400), (201), (401), (540), (601), (112) and (631), respectively, corresponding to the wurtzite hexagonal structure of ZnO (ICSD no. 98-006-5172). The XRD pattern affirms that the synthesis method employed retained the crystallographic structure of both graphene and ZnO. In addition, no other diffraction peak was observed, confirming the purity of the as-synthesised G/ZnO nanocomposite.
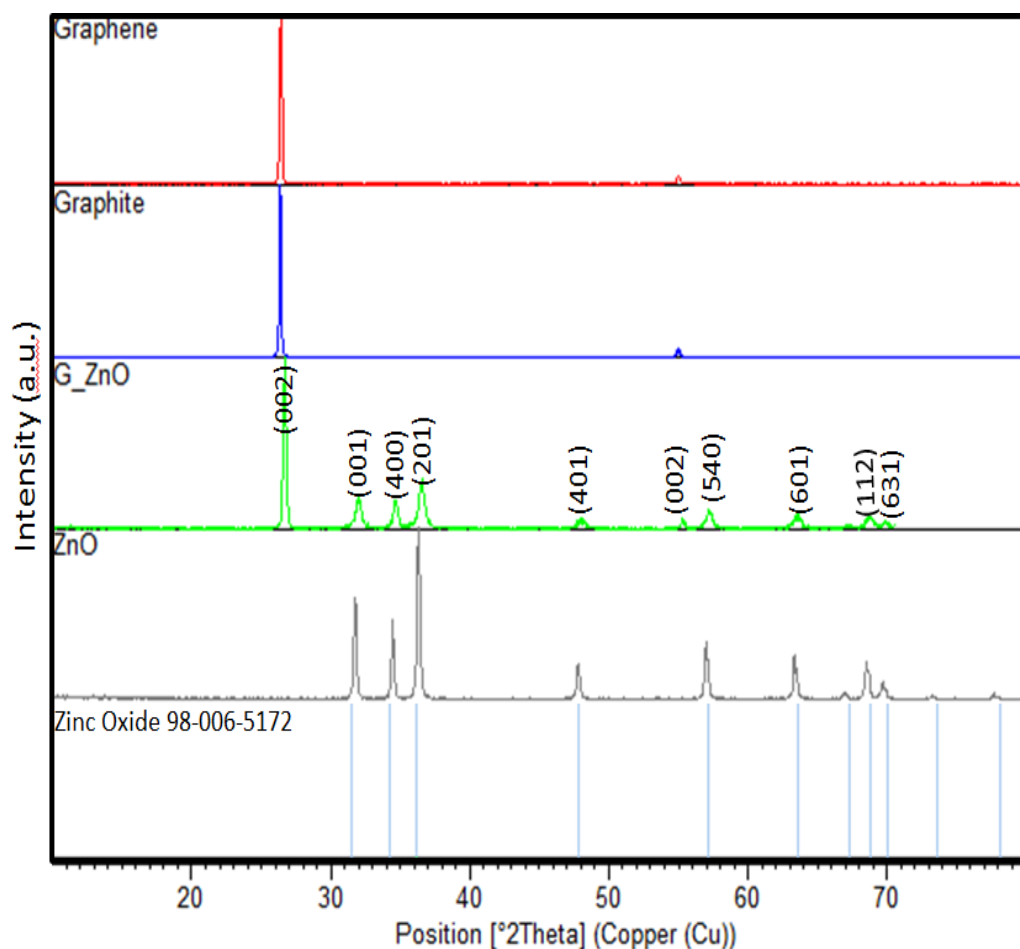
Figure 4.4: XRD patterns of graphite, graphene, zinc oxide and G/ZnO nanocomposite.

Raman spectroscopy is an effective nanometrology analysis method for investigating the crystallisation, structure and defect in nanomaterial. Following the SEM analysis, the Raman spectra of graphene and G/ZnO nanocomposite (1:8) were performed (Figure 4.5). For graphene, three distinct features were prominent, namely the G band at ~1580 cm^{-1} which corresponds to the in-plane vibration of sp^2 carbon atoms, the 2D band at 2719 cm^{-1} and the D band at 1351 cm^{-1}, ascribing to the first-order zone boundary phonons. The D peak is typically associated with edge defects, in which the formation of new edges from the exfoliation process of graphite can be seen as defects [213].

Four peaks labelled as "Z" appeared after the hydrothermal treatment, indicating the growth of ZnO nanoparticles. The peak at ~432 cm^{-1} corresponds to the finger signal of the characteristic E_2 mode of ZnO wurtzite structure, while the peaks at ~327 cm^{-1} and ~574 cm^{-1} are well indexed to the transversal optical modes with A_1 symmetry and the longitudinal optical (LO) modes [214]. The broad peak at ~1127 cm^{-1} is attributed to $2A_1$ (LO), $2E_1$ (LO) and 2LO mode of ZnO [215]. The D-band, G-band and 2D-band were located at ~1349 cm^{-1}, ~1574 cm^{-1} and ~2717 cm^{-1}, the shift of the bands are likely due to the doping effects of ZnO [10]. The Raman spectrum after the hydrothermal treatment confirms that the structure of graphene was not destroyed and the G/ZnO nanocomposites were formed, which is in good agreement with the XRD results (Figure 4.4).
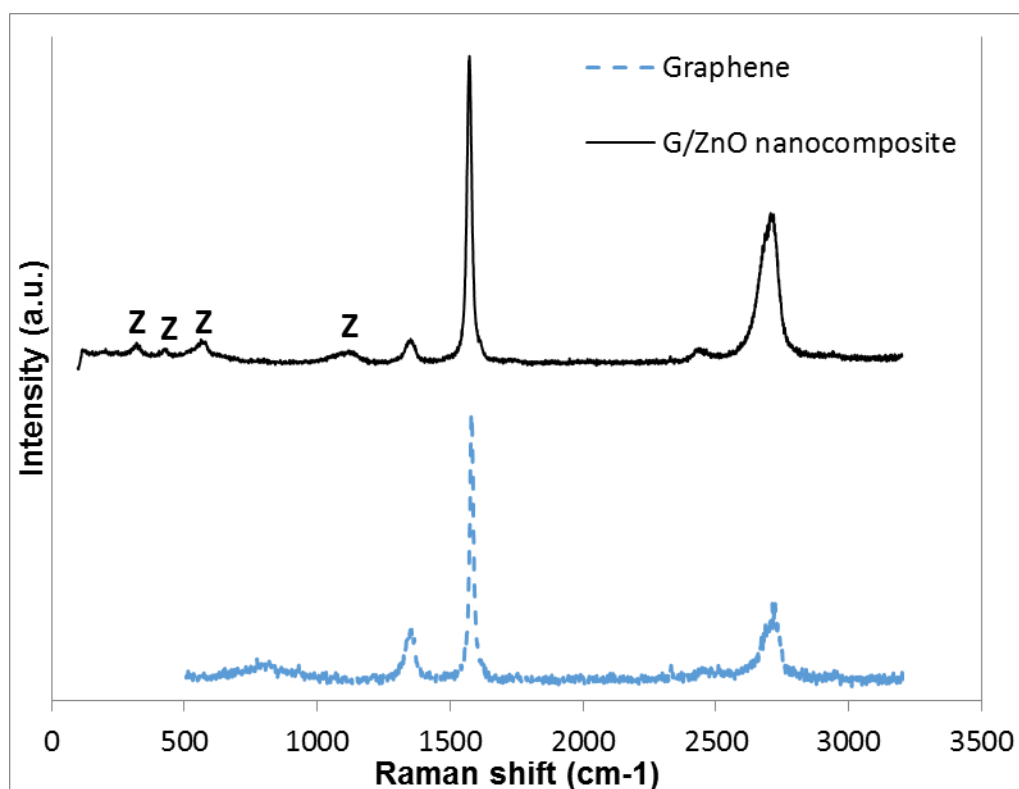
Figure 4.5: Raman spectra of graphene and G/ZnO nanocomposite synthesised via the optimum mass ratio of 1:8.

4.3.2 Preliminary Study on the G/ZnO Nanocomposites with Different Mass Ratios

A preliminary study was carried out to investigate the sensing performances of the G/ZnO nanocomposites synthesised from different mass ratios as shown in Figure 4.6. It was observed that increasing ZnO precursor mass ratio resulting in increasing peak current value until the mass ratio of 1 : 8, after that the G/ZnO nanocomposite synthesised from mass ratio of 1 : 16 showed decrease in the peak current value. The result obtained is in agreement with the SEM analysis (Figure 4.3A to D), where increase in the loading mass of ZnO precursor led to more ZnO nanoparticles being formed on the surface of

graphene sheets. However, ZnO nanoparticles were found to agglomerate on the graphene surface for the mass ratio of 1 : 16, forming non-conducting layers that affect the electrocatalytic activity of the as-synthesised nanocomposites. Therefore, the G/ZnO nanocomposite synthesised from the mass ratio of 1 : 8 was chosen as the optimised ratio and used in the following study.
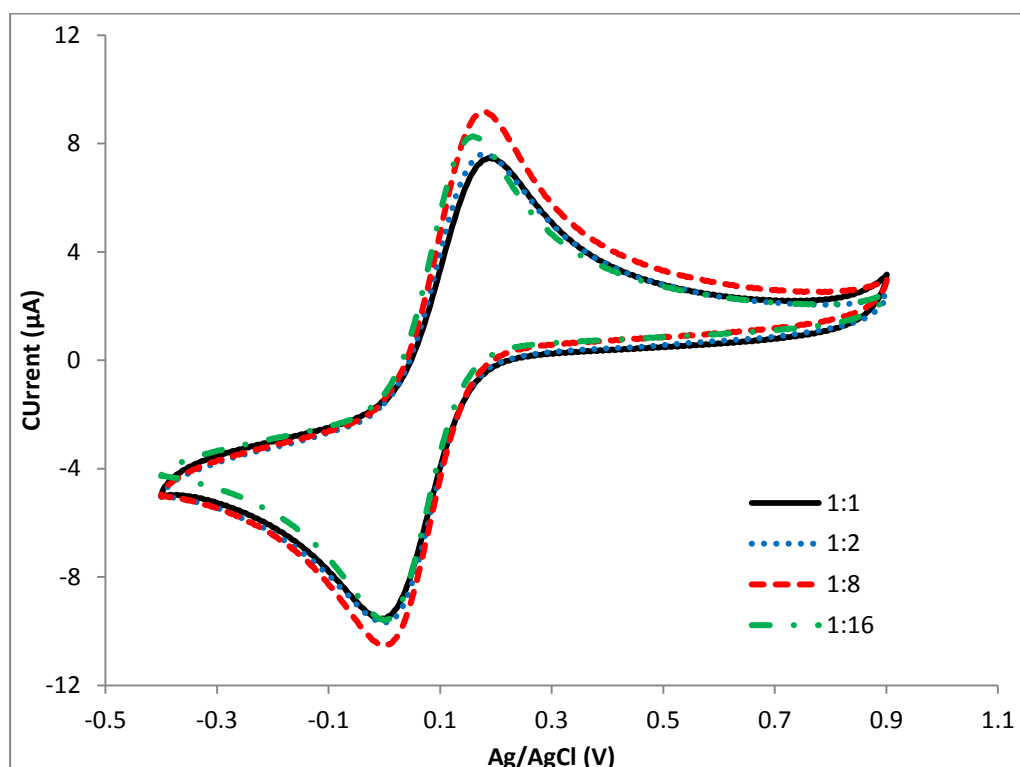
Figure 4.6: Cyclic voltammograms of graphene/zinc oxide nanocomposite synthesised from different mass ratios.

4.3.3 Electrochemical Characterisations of Graphene/Zinc Oxide Nanocomposite

Cyclic voltammetry (CV) was performed to discern the role of individual component and possible synergy between the composite. Based on Figure 4.7, both graphene (curve b) and G/ZnO nanocomposite-modified SPCE (curve c)

showed an enhanced activity towards the reduction of H_2O_2 as compared to that of bare SPCE (curve a). The results also depicted that the G/ZnO nanocomposite (curve c) demonstrated a significant increase in peak current of almost 3 times of the response of bare SPCE (curve a). The improved electrochemical properties of the nanocomposites could be attributed to the synergistic effect between graphene and ZnO nanoparticles, in which the pristine quality of the graphene improves the electrical conductivity while ZnO nanoparticles provide a 3D conductive system for the transfer of electron [195].

Hydrogen peroxide (H_2O_2) is generally taken as the model analyte for the evaluation and electroanalytical properties of materials since it is the by-product of most electrochemical response of enzymatic process and also plays an important role in food industry, environmental monitoring, clinical diagnosis and detection of biological compounds [216]. Therefore, the sensitivity of a biosensor towards the detection of H_2O_2 is of utmost importance. In Figure 4.7(d), the CV response of G/ZnO nanocomposite-modified SPCE increased dramatically upon the addition of H_2O_2, revealing remarkable electrocatalytic activity of the composite towards the reduction of H_2O_2. This can be attributed to the large surface area-to-volume ratio of graphene and electroactive property of ZnO, thus improving the electron transfer process [195]. Notably, no redox peaks were observed in Figure 4.7(d), since the redox peaks for H_2O_2 occurs at very high switching potential [207]. Therefore, it is due to this reasoning that non-enzymatic H_2O_2 biosensor is assessed at the maximum current to ascertain its sensing capability [217].
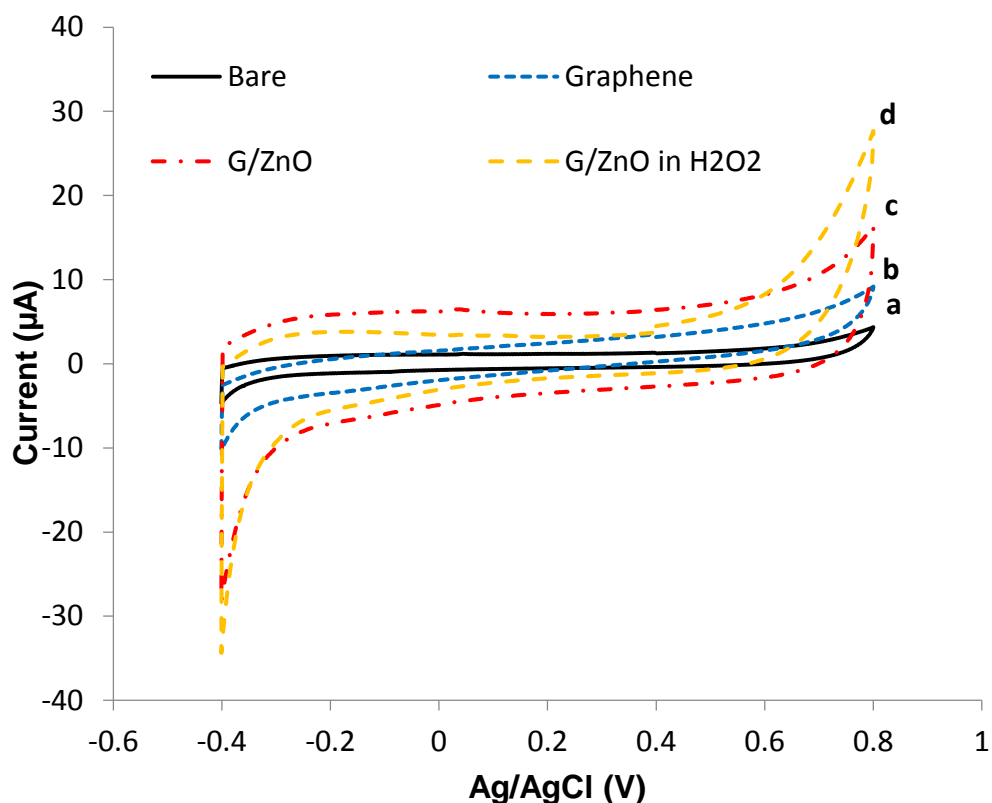
Figure 4.7: Cyclic voltammograms of (a) bare SPCE, (b) graphene-modified SPCE, (c) G/ZnO nanocomposite-modified SPCE in 0.1 M of PBS and (d) G/ZnO nanocomposite-modified SPCE in 0.1 M containing H_2O_2.

4.3.3.1 Effect of Scan Rate

Figure 4.8 shows the cyclic voltammograms recorded for G/ZnO nanocomposite-modified SPCE by varying scan rate from 10 to 100 mV/s. In general, it was observed in Figure 4.8 that peak current increased when a faster scan rate was used. According to the Randles-Sevcik equation (Equation 4.4), in a Nernstian system (reversible system), linear relationship between peak current (i_p) and square root of scan rate ($v^{1/2}$) provides an evidence for a chemically reversible and controlled diffusion electrochemical process [218].

$$i_p = (2.69 \times 10^5)\, n^{3/2}\, A\, D^{1/2}\, C\, v^{1/2} \quad \text{Equation (4.4)}$$

At 25 °C, i_p is the peak current (A), n is the electron stoichiometry, A is the electrode area (cm^2), D is the diffusion coefficient (cm^2s^{-1}), C is the concentration ($molcm^{-3}$) and v is the scan rate (V/s).

It was observed that the occurrence of maximum peak currents always remained at the same voltage regardless of the value of scan rate applied, indicating reversible electron transfer kinetics of the electrode. Besides, the peak current is linearly proportional to the square root of the scan rate as seen in the inset of Figure 4.8, with a correlation coefficient, R^2 of 0.9768. This indicates a diffusion controlled process of the reactants, a relationship which reaffirms that measurements correlate to surface confined reactions at the electrode [218].
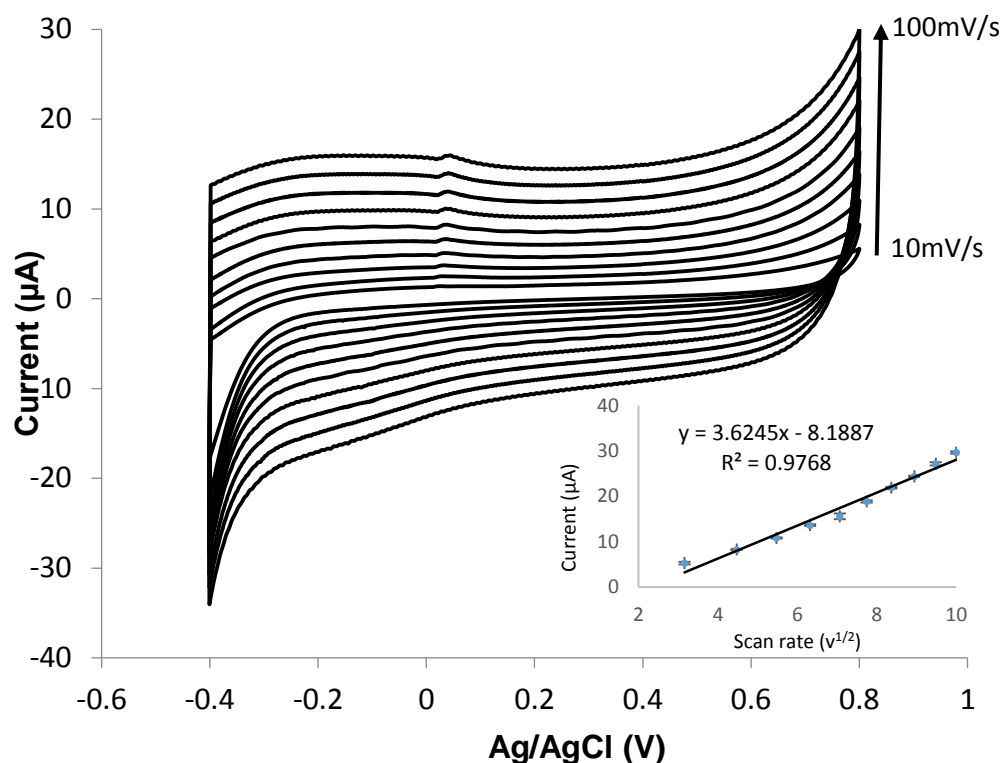
Figure 4.8: Cyclic voltammograms of G/ZnO nanocomposite-modified SPCE at varying scan rates from 10 to 100 mV/s. Inset shows the linear dependence of peak current against square root of scan rates.

4.3.3.2   Amperometric Detection of Hydrogen Peroxide at Graphene/ZnO Nanocomposite-modified SPCE

Amperometry is an analytical chemistry technique to evaluate the sensor's electrocatalytic activity towards the analyte by measuring the current in an electrochemical cell at a fixed potential. In the present study, the electrochemical performance of the as-synthesised G/ZnO nanocomposite was evaluated using the amperometric technique with H_2O_2. During the amperometric *i-t* measurements, the working potential was set at -0.4 V, where the amperometric response of the modified SPCE reached the maximum value. For every 50 seconds, aliquots of 1 mM H_2O_2 were successively injected into

the PBS buffer. For performance comparison purpose, similar analyses were carried out using bare and graphene-modified SPCE.

The amperometric *i-t* responses of bare, graphene- and G/ZnO nanocomposite-modified SPCE are shown in Figure 4.9. It was observed that upon the successive addition of 1 mM H_2O_2, the G/ZnO nanocomposite-modified SPCE displayed the highest current response as compared to bare and graphene-modified SPCE. The G/ZnO nanocomposite-modified SPCE responded rapidly and reached a steady state (95% of the maximum value) within 3 seconds, indicating a fast amperometric response to H_2O_2 reduction and the high sensitivity of the biosensor.

B
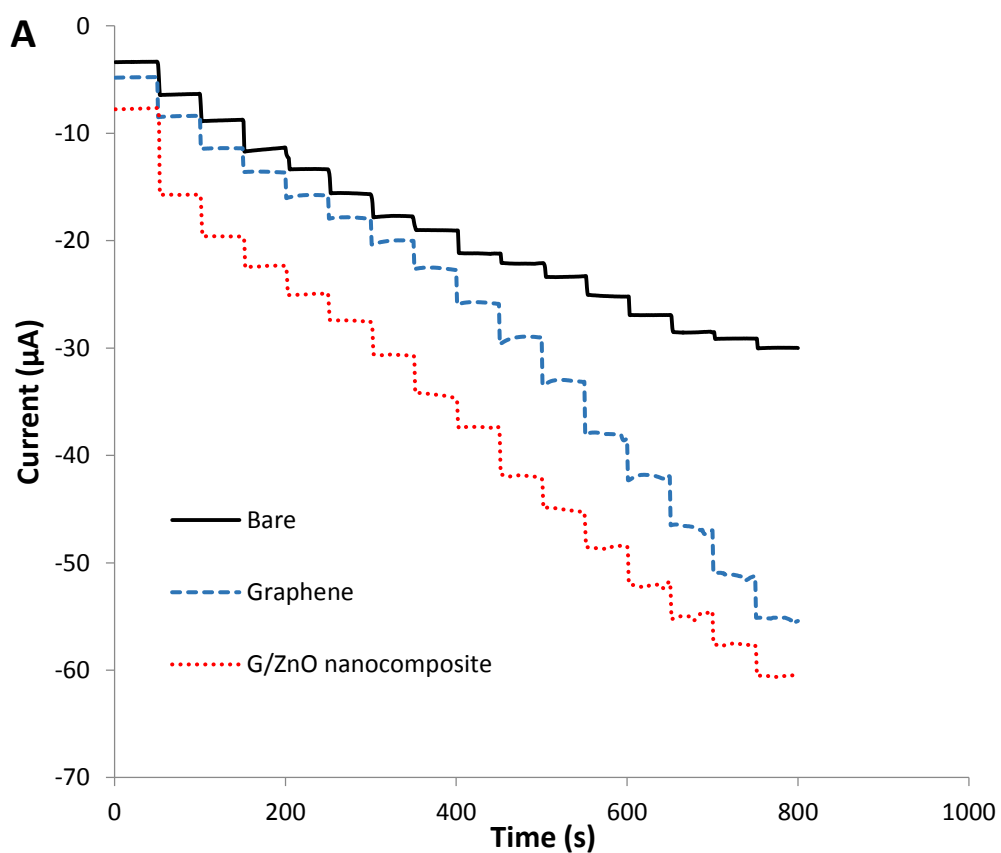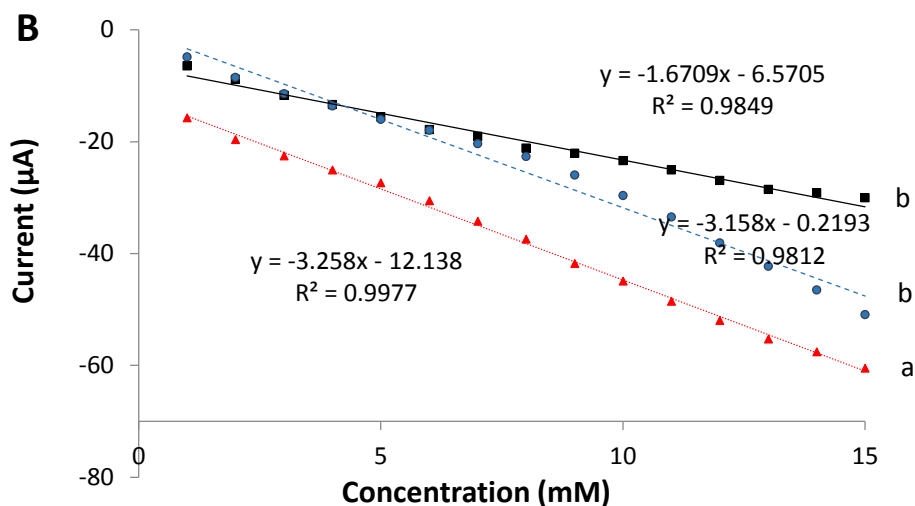
Figure 4.9: (A) Real time amperometric response of bare, graphene- and G/ZnO nanocomposite-modified SPCE for successive additions of H_2O_2 ranging from 1 to 15 mM in PBS buffer at a fixed potential of -0.4 V; (B) Plot of the linear range of bare, graphene- and G/ZnO nanocomposite-modified SPCE with their respective regression equation and R^2 value.

In addition, the G/ZnO nanocomposite-modified SPCE displayed a good linear relationship with H_2O_2 in the range of 1 to 15 mM with a correlation coefficient, R^2 of 0.9977 (Figure 4.9B) was obtained. It was also observed that G/ZnO nanocomposite-modified SPCE exhibited the highest sensitivity (3.2580 μAmM^{-1}) among the three SPCEs tested, approaching approximately 200% current response of bare SPCE (1.6709 μAmM^{-1}). As compared to the sensitivity (0.055 μAmM^{-1}) of the sensor modified with G/ZnO nanocomposite synthesised from the method mentioned in Chapter 3, this developed sensor manifested an approximate 58 times of improvement. This could be postulated to the stronger bonding between graphene sheets and ZnO nanoparticles resulting from hydrothermal growth, thereby the as-synthesised G/ZnO nanocomposite

exhibited an improved electrocatalytic activity. The detection limit of the G/ZnO nanocomposite-modified SPCE was estimated to be 7.4357 µM based on signal-to-noise ratio equal to 3 (S/N = 3).

The analysis on the ANOVA, means and standard deviations are presented in Table 4.2 and Figure 4.9B. The one-way ANOVA showed significant main effect for sensor modified with different materials, $F(2, 42) = 8.35$, $P < 0.05$. From the Fisher's protected least significant difference (LSD) analysis, it was observed that the G/ZnO nanocomposite-modified SPCE showed the highest significance for the sensitivity for the detection of H_2O_2 as indicated by the letter "a" in Figure 4.9B.

Table 4.3 shows the comparison of several typical nonenzymatic H_2O_2 sensors reported previously, the present G/ZnO-modified sensor displayed a comparable performance. The high sensitivity of the G/ZnO nanocomposite based sensing platform is promising and is postulated to be suitable for the detection of other biological compounds, such as glucose, DNA as well as biomarkers.

Table 4.2: Results of one-way analysis of variance (ANOVA) with sensor at 3 levels in a completely randomised design (CRD).

Source of variation	Degree of freedom	Sum of square	Mean square	Computed F value	Probability value
Sensor	2	2.630×10^{-9}	1.315×10^{-9}	8.35	<.001
Residual	42	6.619×10^{-9}	1.576×10^{-10}		

Total	44	9.249×10^{-9}

Table 4.3: Comparison of G/ZnO nanocomposite-modified electrode with some previously reported H_2O_2 sensors.

Sensors	Detection limit	Sensitivity	Reference
Ag nanoparticles/graphite substrate	1.0 µM	0.0490 µAmM^{-1}cm^{-2}	[219]
Horseradish peroxidase/Au/ITO	8 µM	-	[220]
Graphene wrapped Cu_2O nanocubes	20.8 µM	-	[221]
Mesoporous platinum microelectrodes	4.5 µM	0.0028 µAmM^{-1}cm^{-2}	[222]
Graphene/ZnO	7.4357 µM	3.2580 µAmM^{-1}	This work

4.3.3.3 Interference Study

It was well known that some co-existing electroactive species in nature will affect the sensor response. Therefore, the selectivity of the G/ZnO-modified SPCE was studied by introducing common interference species into the PBS buffer. Figure 4.10 shows the amperometric response upon the addition of 1 mM H_2O_2, 1 mM uric acid, 1 mM fructose and 1 mM glucose into the buffer. The result demonstrated that for each addition of H_2O_2, the graphene/ZnO-modified sensor showed rapid response. On the other hand, no

significant response was observed for the addition of 1 mM uric acid, fructose and glucose, respectively. The result validates the high selectivity of G/ZnO-modified SPCE towards the detection of H_2O_2.
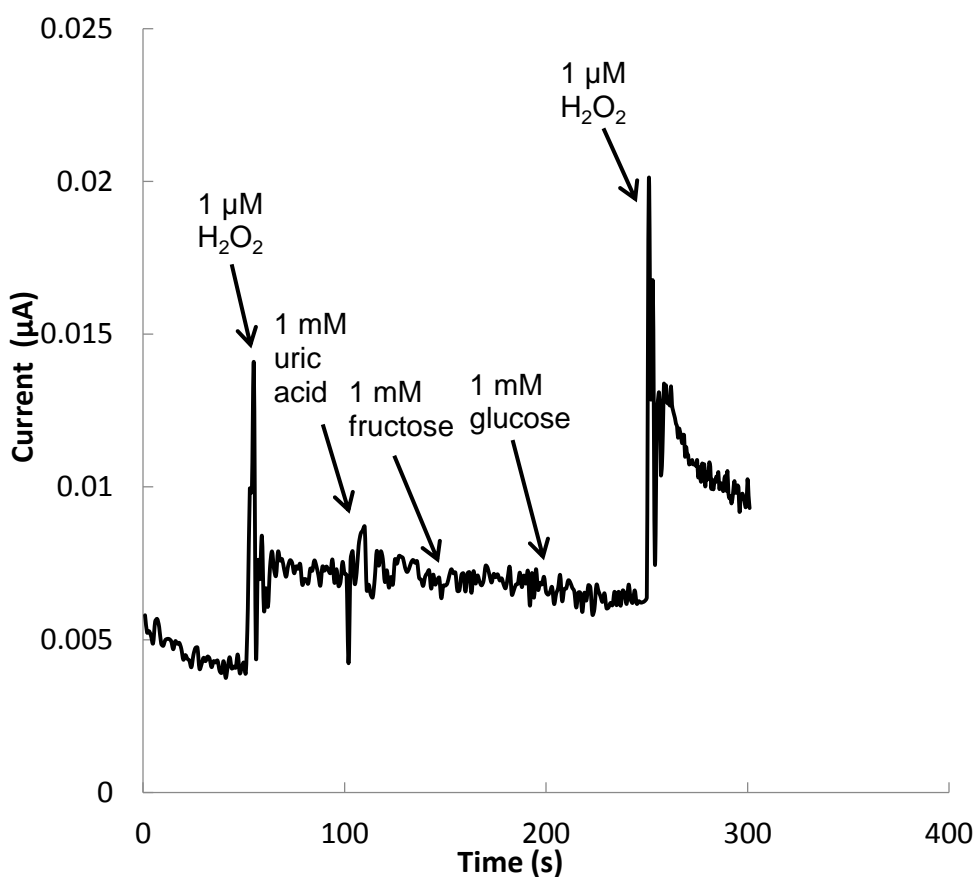
Figure 4.10: Amperometric response of G/ZnO nanocomposite-modified SPCE for the successive addition of 1 μM H_2O_2, 1 mM uric acid, 1 mM fructose, 1 mM glucose and 1 μM H_2O_2 into PBS buffer.

4.4   Chapter Summary

In this chapter, a facile, green and efficient approach for the synthesis of graphene/ZnO nanocomposite at low temperature has been reported. The structural analysis and electrochemical properties of the G/ZnO nanocomposite were studied comprehensively. The SEM and TEM images

clearly revealed that that ZnO nanoparticles were homogenously distributed on the graphene sheets while the XRD result affirmed the successful hydrothermal growth of ZnO nanoparticles. In comparison with unmodified SPCE, the G/ZnO nanocomposite-modified SPCE demonstrated an improved electrochemical performance. The G/ZnO nanocomposite-modified SPCE displayed the best electrochemical performance, at a significance level of $P >$ 0.05. In this chapter, the sensitivity of the sensor modified with the as-synthesised G/ZnO nanocomposite was determined to be 3.2580 μAmM^{-1}, with a LOD of 7.4357 μM based on signal-to-noise ratio equal to 3 (S/N = 3). Therefore, the G/ZnO nanocomposite synthesised from the low temperature hydrothermal growth described in this chapter has been determined to be a more suitable sensor electrode platform which is used in further work.

Chapter 5 Detection of Avian Influenza *H5* Gene by Graphene/Zinc Oxide Nanocomposite-Enhanced Electrochemical Genosensor

5.1 Overview

Chapter 4 described a successful demonstration of the fabrication of non-enzymatic hydrogen peroxide (H_2O_2) sensor using graphene/zinc oxide (G/ZnO) nanocomposites synthesised via low temperature solvothermal growth method. The G/ZnO nanocomposite-modified sensor exhibited an excellent electrocatalytic activity towards the reduction of H_2O_2 with a significance level of $P > 0.05$. The sensitivity of the G/ZnO nanocomposite-modified hydrogen peroxide sensor was 3.2580 μAmM^{-1} with a limit of detection of 7.4357 μM. Owing to the good electrochemical performance of the G/ZnO nanocomposite-modified sensor in detecting H_2O_2, the feasibility of G/ZnO platform for biosensing application was further evaluated for the detection of an Avian Influenza H5N1 viral gene.

Influenza A viruses are well known for their genetic and phenotypic diversity in avian and mammalian hosts. They are divided into subtypes from the two proteins on the surface of viruses; haemagglutinin (HA) and neuraminidase (NA). In 2009, the world witnessed the first influenza pandemic of the 21st century with the outbreak of H1N1 influenza A, culminating in an estimate of 284,500 deaths due to its high transmissibility [223]. Currently, there are over 17 different types of haemagglutinin from H1 to H17 and 9

different types of neuraminidase, from N1 to N9, all of which can easily evolve at high rate and the world is on high alert for the next highly pathogenic avian influenza (HPAI) that may lead to the next global pandemic [224].

Particularly, the HPAI virus subtype H5N1, distinguishable on the basis of H5 and N1 antigenic surface proteins has attracted much concern because it is the most virulent and deadliest. Till year 2015, the world health organisation (WHO) has recorded 784 cumulative human cases for H5N1 infections with 429 deaths, which sum up to an alarming 55% human mortality rate [225]. This is because many patients with milder symptoms could not discriminate the symptoms of H5N1 from common influenza at early stage, and were hospitalised later with severe complications. To hold back the disease progression at an early stage of outbreak and further prevent a worldwide transmission, the development of novel, highly sensitive and rapid analytical techniques for medical diagnostics is of utmost importance. To date, a variety of methods have been developed for the detection and identification of virus, such as viral isolation, quartz crystal microbalance and many more [224, 226, 227]. However, these techniques are commonly more time consuming, costly, laborious and demanding for well trained personnel.

Conventionally, PCR amplicons are detected by agarose gel electrophoresis which is time consuming and involves the usage of harmful agents such as ultraviolet (UV) light and ethidium bromide. Furthermore, the detection methods for PCR amplicons are expensive with the uses of chemicals such as SYBR® green dye, Taqman or molecular beacons and a specialised

thermal cycler. Electrochemical DNA biosensors (genosensors) provide a very promising alternative compared to conventional molecular detection approaches, due to their advantages such as high sensitivity, low cost, time effectiveness, compatibilities with microfabrication technology and compact instrumentation taking on portable devices. For this purpose, nanomaterials based matrices have intrigued the development of novel and improved sensing devices, in terms of providing efficient platforms for immobilisation of various biomolecules. This chapter reports on a highly sensitive electrochemical DNA biosensor modified with G/ZnO nanocomposites synthesised via low temperature hydrothermal growth. Soliciting further investigations in future, G/ZnO-based electrochemical genosensor may provide an all-rounded detection platform which permits early, rapid and sensitive detection of *H5* gene of H5N1 virus, enabling the achievement of a more effective treatment outcome.

5.2   Experimental Details

5.2.1   Materials

Streptavidin (purified from *Streptomyces avidinii*), 1-ethyl-3-(3-dimethyl-aminopropyl) carbodiimide hydrochloride (EDC), *N*-hydroxysuccinimide (NHS), ethanolamine hydrochloride, bovine serum albumin (BSA), sodium dodecyl sulphate (SDS), sodium chloride (NaCl), monosodium phosphate (NaH_2PO_4), disodium phosphate (Na_2HPO_4) and 1-pyrenebutyric acid N-hydroxysuccinimide ester (PSE) were purchased from Sigma Aldrich (St. Louis, USA). Horseradish peroxidase (HRP)-conjugated rabbit

polyclonal antifluorescein antibody (1.5 mg/ml) were purchased from Abcam (Cambridge, MA). Stock antibodies solution (diluted to 1:200 ratio (1 antibody: 200 PBS)) was prepared in 0.05 M PBS buffer. Ethanol was obtained from Merck (New Jersey, US). 10x saline sodium citrate (SSC) was purchased from First Base (Selangor, Malaysia). All chemicals were used as received and deionised water (DI) from the Millipore system was used throughout the experiment. Phosphate buffer solution (PBS) tablets were purchased from Sigma Aldrich (St. Loius, USA) and dissolved in DI water to produce 0.1 M buffer solution with pH of 7.4.

5.2.2   Functionalisation of Materials with PSE

The graphene and G/ZnO nanocomposites used in this work were synthesised as reported in Section 4.2.2 and 4.2.3, respectively. Both graphene and G/ZnO nanocomposites were functionalised with PSE according to the method reported by Joanna and colleagues [228]. Briefly, the material dispersion and PSE in the ratio of 1 : 4 were mixed thoroughly via sonication for 30 minutes at room temperature. The mixture was centrifuged at 1000 rpm and washed repeatedly with ethanol and DI water respectively to remove loosely bound PSE. The sediment was dried overnight at 80 °C to collect PSE-functionalised materials (G/PSE and G/ZnO/PSE). The PSE-functionalised material dispersions (5 µL) were drop casted onto screen printed carbon electrode (SPCE, DropSens, Spain) and air-dried.

5.2.3 Fabrication of Genosensor

The fabrication of enzyme-based electrochemical genosensor is shown in Figure 5.1. It starts with immobilisation of streptavidin onto the working electrode of SPCE (Figure 5.1A). For bare SPCE (Figure 5.1AI), covalent agent (2.5 µL, 200 mM EDC and 50 mM NHS prepared in 50 mM phosphate buffer) was dropped onto the working electrode of bare SPCE and incubated for surface activation. Streptavidin (5 µL) displaced the functional group of NHS and therefore was bound onto the bare SPCE.

For G/PSE-modified SPCE (Figure 5.1AII), 5 µL of streptavidin was drop casted on the working electrode of SPCE and incubated. Streptavidin was bound onto the SPCE via amide bond with the PSE. Following the method employed for G/PSE-modified SPCE, G/ZnO/PSE-modified SPCE also used the same method to fabricate streptavidin treated SPCE.

Following the immobilisation of streptavidin onto SPCE, the unbound area on the streptavidin-treated SPCE was blocked with 50 µL of ethanolamine hydrochloride and incubated in dark. Next, 50 µL of BSA was added to prevent non-specific binding of HRP-conjugated antifluorescein antibody. Each step was incubated for 10 min at room temperature and the SPCE was washed by dipping once in 5 mL of DI water after each step.

To test the sensitivity of the fabricated genosensor, different dilutions of *H5* viral gene DNA were deposited onto the SPCE (Figure 5.1B). Briefly, 5 µL of biotin- and fluorescein-labelled DNA was pipetted onto the SPCE and incubated for 5 min. The biotin label would form specific covalent bond with

streptavidin and hence the DNA was bound onto the SPCE. The SPCE was then incubated for 5 min with 5 µL of HRP-conjugated antifluorescein antibody. The HRP enzyme was bound onto the SPCE via the conjugation of antifluorescein antibody to fluorescein label. After each incubation step at room temperature, the SPCE was washed by dipping 10 times in 5 mL of 0.1x SSC containing 0.5% SDS to minimise a nonspecific immobilisation of biological compound.

AI

AII

EDC/NHS

SPCE
Bare SPCE

SPCE

SPCE

SPCE
Streptavidin-treated
SPCE

PSE-functionalised
graphene
(G/PSE)

SPCE
G/PSE-modified
SPCE
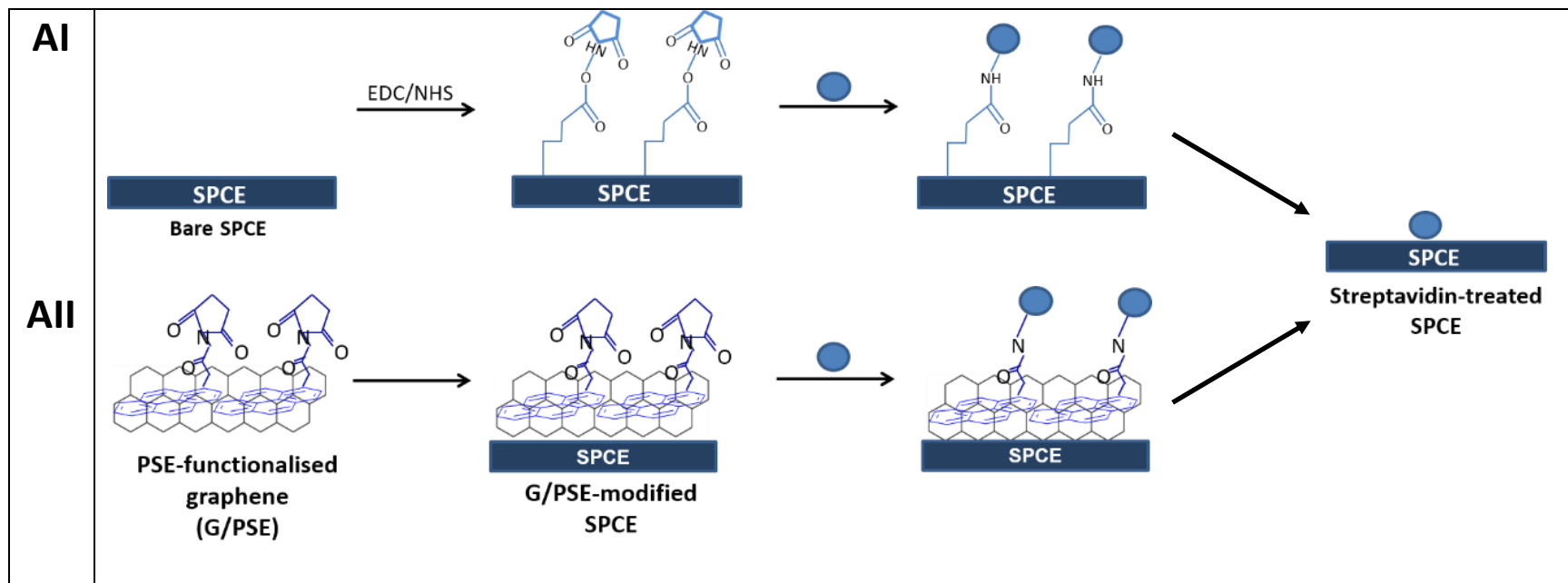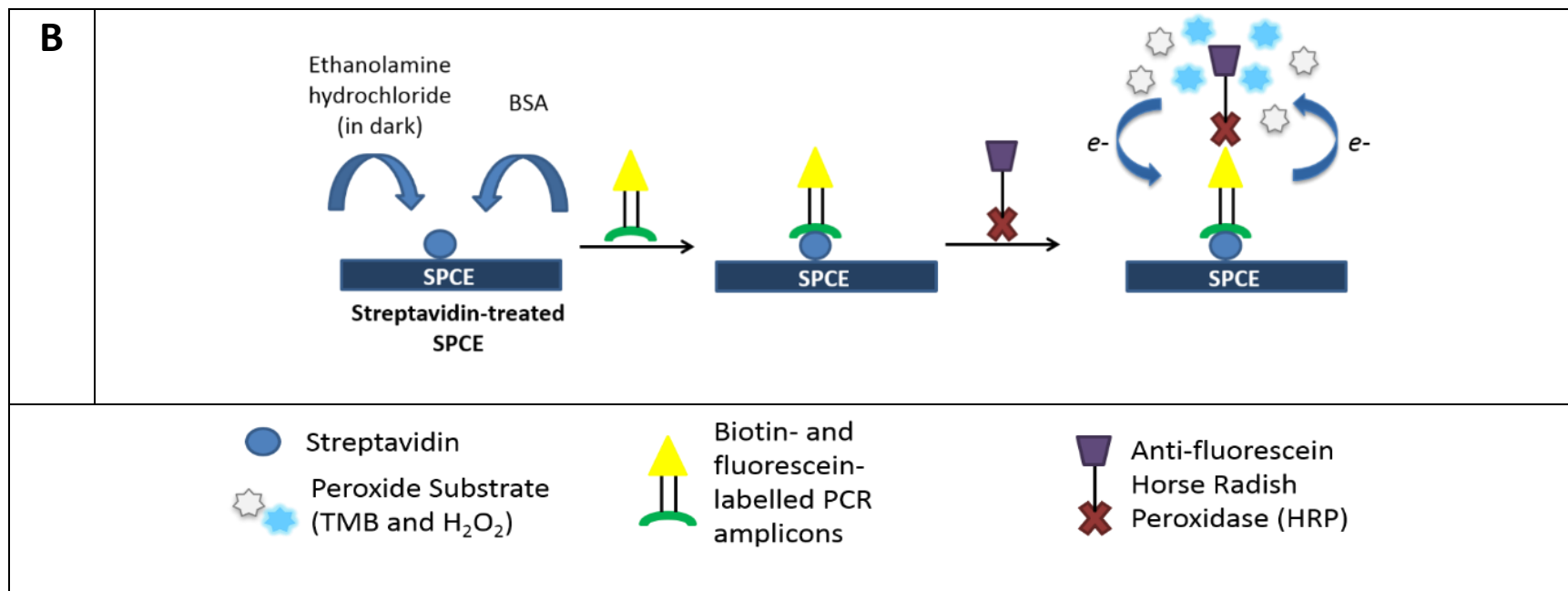
SPCE

Figure 5.1: Schematic diagrams for the development of electrochemical DNA biosensor for the detection of *H5* gene. (A) Immobilisation of streptavidin on (I) bare SPCE via covalent agent (EDC and NHS), (II) PSE-functionalised graphene (G/PSE)-modified SPCE, (B) Development of sandwich platform for amperometric detection of PCR amplicons.

5.2.4 Polymerase Chain Reaction (PCR)

The haemagglutinin, *H5* DNA sequence of the highly pathogenic Avian Influenza (HPAI) H5N1 strain A/chicken/Malaysia/5744/2004(H5N1) was synthesised based on the Influenza Virus Resource at National Centre for Biotechnology Information (NCBI) (Genbank accession: KC684446). The modified biotin- and fluorescein-labelled primers were designed flanking the *H5* gene and custom synthesised by First Base (Selangor, Malaysia), sequences as shown below:

Biotin-modified forward primer, HAFP (B): 5'-/5BiosG/GG TTA CCA TGC AAA CAA CTC GAC AGA GC -3'/

Fluorescein-modified reverse primer, HARP (F): 5'-/5FluorT/AT TGT AAC GAC CCA TTG GAG CAC ATC CAT AAG -3'/

Polymerase chain reaction (PCR) was performed in 50 µL reaction containing 1x KCl PCR buffer, 1.5 mM $MgCl_2$, 0.3 mM dNTPs, 0.3 µM of each forward and reverse modified primer, 1.0 U of *Taq* DNA polymerase, and 1 ng of DNA template. All PCR reagents were purchased from Fermentas (Lithuania). The PCR thermal cycling was carried out using GS2 PCR thermal cycler (G-Storm, UK).

For gradient PCR program, the annealing temperatures were set ranging from 50 °C to 72 °C. This step was taken in order to select an optimum annealing temperature for the generation of *H5* amplicons.

After that, the DNA template was pre-denatured at 94 °C for 3 min, amplified for 30 cycles with denaturation at 94 °C for 1 min, annealing at optimised temperature (56.5 °C) for 1 min and extension at 72 °C for 1 min 30 s with a final elongation at 72 °C for 8 min.

The PCR amplicons were then purified using GeneAll® PCR SV purification kit (GeneAll Biotechnology, Seoul, Korea) and eluted using buffer EB (10 mM TrisCl, pH 8.5) for maximum DNA recovery and long term storage.

5.2.5 Agarose Gel Electrophoresis

PCR amplicons with different dilution factors along with GeneRulerTM 1 kb DNA ladder (Fermentas, Lithuania) were subjected to 1 % agarose gel electrophoresis. The gel was run at 90 V for 35 min, which was then visualised by UV light box and Alpha Innotech Fluorescence (Alpha Innotech, USA).

5.2.6 Dot Blot Assay

The dot blot assay was carried out in a way similar to the preparation of sandwich platform as shown in Figure 5.1. Streptavidin (3 mL) was pipetted onto 1 cm^2 of nitrocellulose membrane strip (Bio-Rad, Hercules, CA) and the membrane was subsequently placed in individual wells of a MicroWell™ 24-well polystyrene plate (Sigma Aldrich) placed on an orbital shaker. PBST buffer (500 mL, 10 min) was used for washing after every incubation step unless stated otherwise. Blocking of non-specific antibodies binding was done by incubation with BSA (500 mL, 1 h). Purified *H5* PCR amplicons (2 mL, different dilutions) were spotted onto the streptavidin-blotted nitrocellulose membrane, followed by antifluorescein horseradish peroxidase (HRP) conjugate (2 mL, 30

min). The washing steps were repeated thrice with PBST for complete removal of unbound conjugates, once with deionised water for removal of buffer residues. Lastly, 3,3',5,5'-Tetramethylbenzidine (TMB) (300 mL, 5 min) was added to the membrane. The reactions were terminated immediately with deionised water, once the visible blue aggregates were spotted on the membrane.

5.2.7 Amperometric Detection of *H5* Gene

TMB substrate peroxidase solution (50 mL) (KPL, Gaithersburg, MD) was added to the fabricated genosensor for amperometric detection of PCR amplicon derived from the *H5* gene. The enzymatic redox reaction was detected as current signals using µAutolab PGSTAT III potentiostat (Metrohm, Netherlands) interfaced with controlling software NOVA 1.10. Intermittent pulse amperometry (IPA) was employed for the measurement in this study involving a 10 seconds incubation period followed by an applied potential of 1.0 V with a measurement time of 45 seconds and pulse time of 10 seconds, at a frequency of 5 Hz and a current range of 1 mA.

The *H5* PCR amplicon was serially diluted as shown in Table 5.1 to test the sensitivity of the genosensor. The reproducibility of the fabricated genosensor was determined by the relative standard deviation (%RSD) of three measurements performed in three separate experiments, which were calculated using standard deviations (SD) and mean current changes of the serially-diluted *H5* PCR amplicons.

Table 5.1: Dilution factor of *H5* PCR amplicon and their respective

concentrations.

Dilution factor	Concentration (ng/μL)
1	8.5096
2	4.2548
4	2.1274
8	1.0637
16	0.5319
32	0.2659

The data was assessed via Shapiro-Wilk test and Bartlett's test, respectively in Genstat to determine the distribution pattern of the residuals and homogeneity of variance. One-way analysis of variance (ANOVA) was used to evaluate the performance of G/ZnO/PSE-modified SPCE at different concentrations. Differences were considered significant at $P < 0.05$.

5.3 Results and Discussions

5.3.1 Polymerase Chain Reaction (PCR) Detection of Avian Influenza H5 Gene

Polymerase chain reaction (PCR) was performed to amplify the *H5* viral gene insert in TOPO 2.1 holding plasmid vector with a specific primer pair that consists of respective biotin-labelled forward primer and fluorescein-labelled

reverse primer. Selection of PCR primers annealing temperature is crucial as usage of too low annealing temperature can produce non-specific products whereas too high annealing temperature might reduce the PCR yield. Therefore, a series of PCR reactions containing constant primer and DNA template concentrations, across a range of annealing temperatures were carried out for obtaining the most optimum annealing temperature for the primers.

In this work, the annealing temperatures of PCR primers were varied from 50 °C to 72°C. Figure 5.2 shows the agarose gel profiles with 12 identical samples that were subjected to different annealing temperatures. The bands were estimated to be slightly larger than the 1500 bp ladder indicator, which corresponded to the size of *H5* gene (1616 bp), indicating a successful amplification of targeted *H5* gene sequence. An optimum annealing temperature should result in abundant PCR product yield with specificity, displaying a thick band of the correct size with less smearing. This analysis revealed that 56.5 °C (L5) used in the PCR assay was appropriate; therefore this annealing temperature was chosen in the following PCR reactions.
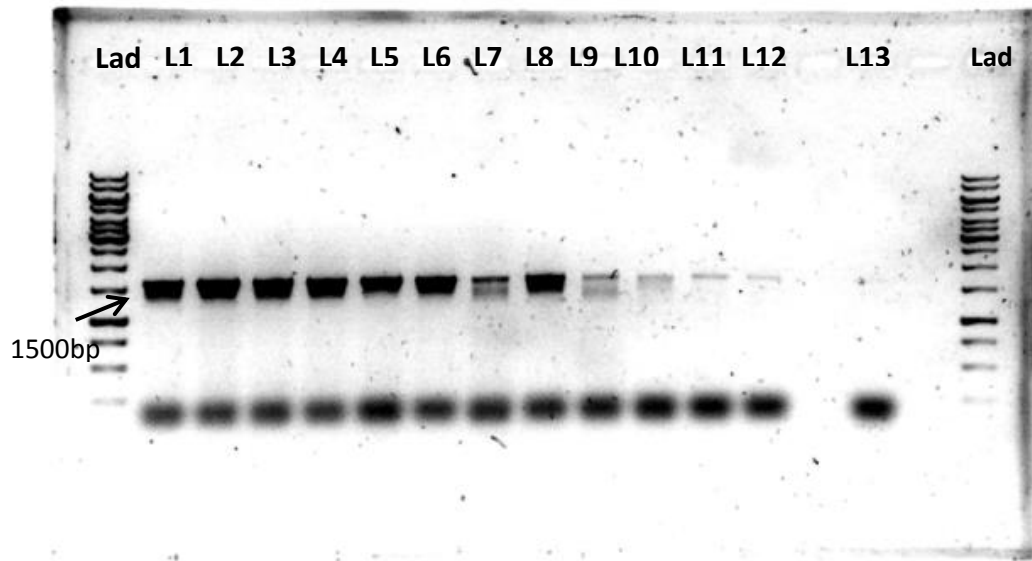
Figure 5.2: PCR profiles of the *H5* products amplified at the annealing temperatures varied from 50 °C to 72 °C, electrophoresed at 1% w/v agarose gel. Lad - GeneRuler™ 1 kb DNA ladder; L1 – 50.2 °C; L2 – 50.8 °C; L3 – 52.0 °C; L4 – 54.1 °C; L5 – 56.5 °C; L6 – 59.4 °C; L7 – 62.3 °C; L8 – 65.2 °C; L9 – 68.5 °C; L10 – 70.5 °C; L11 – 71.7 °C; L12 – 72.4 °C; L13 – no template negative control.

PCR was performed to amplify the *H5* gene sequence and the resulting PCR product was purified using GeneAll® PCR SV purification kit. Figure 5.3 shows the agarose gel electrophoresis analysis of purified PCR products illuminated under ultraviolet (UV) ray. It was observed that positive samples (L1 and L2) were presented as bright bands in the gel while no band was observed for negative sample (L3). Successful PCR amplification of *H5* gene was indicated by the band sizes of the PCR products which were larger than the 1500 bp ladder indicator. Upon comparison between stained and unstained agarose gel, fluorescence signal from the labelled PCR amplicons was observed

in both cases, affirming successful tagging of fluorescein label onto the PCR products.
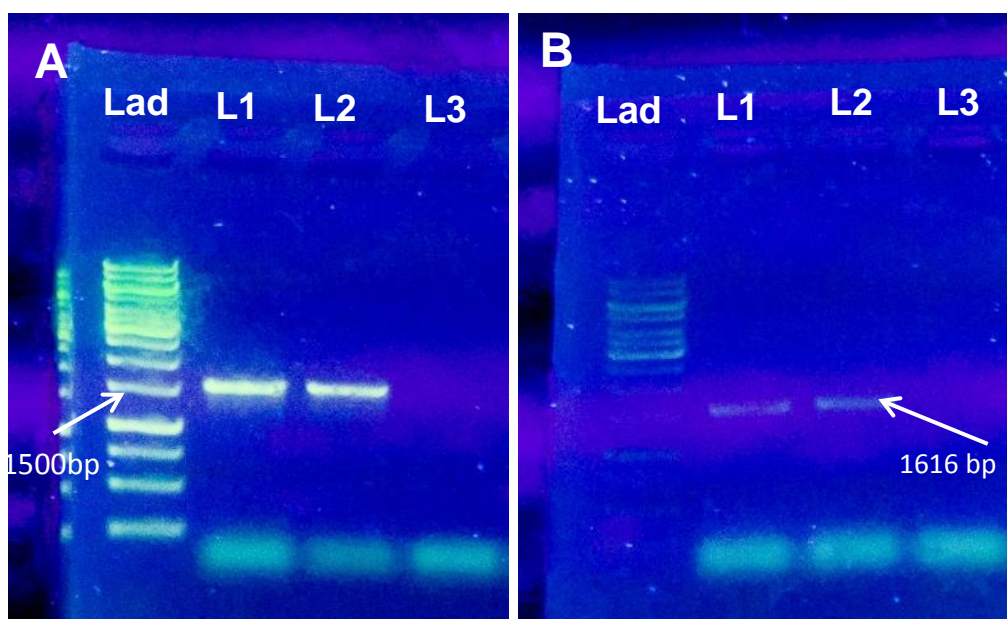
Figure 5.3: Gel electrophoresis analysis of PCR products illuminated under UV ray (A) with and (B) without staining with SYBR® Green. Lad – GeneRuler™ 1 kb DNA ladder; L1, L2 – H5 PCR amplicons; L3 – no template negative control.

5.3.2 Detection of Avian Influenza *H5* Gene using Developed Genosensor

In the development of Avian Influenza *H5* gene sensing platform, bare SPCE was constructed as control to compare the sensing performance with graphene- and G/ZnO-modified SPCE. As shown in Figure 5.1AI, the covalent agent (EDC/NHS) was applied to bare SPCE for surface activation. EDC is a zero-length crosslinking agent used to crosslink proteins via amines and carboxylic acids. EDC will react with carboxylic acid groups to form an active O-acylisourea ester, and NHS is usually added to increase the stability of the active ester [229]. The ester will react with nucleophiles, such as primary amine group, to form

stable zero-length amide bonds [230]. Therefore, after the surface activation of bare SPCE with EDC and NHS, streptavidin with the amine group will displace the functional group of NHS, thereby being bound onto the bare SPCE.

In this work, PSE was used as a bi-linker to anchor the probe DNA onto the graphene- and G/ZnO-modified electrodes. The PSE bi-linker consists of a pyrene moiety and a succinimidyl fragment. The four condensed six-membered aromatic rings on the pyrene fragment would interact with graphene surface via strong pi-pi interaction whereas the succinimidyl fragment is highly reactive to nucleophilic substitution by primary and secondary amines that exist on the surface of most biological molecules (Figure 5.1AII) [231]. Streptavidin with amine groups was then bound onto the G/PSE- or G/ZnO/PSE-modified SPCE by forming an amide bond with the succinimidyl ester. In addition, the pyrene and succinimidyl fragments are linked by an alkyl chain whose structure is highly flexible, thereby developing a highly versatile sensing platform based on graphene or G/ZnO nanocomposite.

After incubation of SPCEs with streptavidin, ethanolamine hydrochloride was added to inactivate the unreacted esters. BSA was then added to the SPCE to block the SPCE surface, ultimately preventing non-specific binding of HRP-conjugated antifluorescein antibody [232]. Based on the high affinity between streptavidin and biotin, the biotinylated PCR amplicon was bound onto the streptavidin-treated SPCE [233]. The fluorescein label on the PCR amplicon was recognised by the HRP-conjugated antifluorescein antibody, and thereby completing the development of sensing platform.

In this electrochemical genosensing platform, TMB substrate was selected to be used for enzymatic reaction due to its acceptably high detection sensitivity and popularity in research use. Incubation with TMB generally yields a prominent background, hence, the use of more diluted antibody is usually recommended which also leads to a saving on the usage of antibody [234]. In addition, TMB is more rapidly oxidised than other HRP substrates, resulting in a faster detection. The oxidation of TMB was catalysed by HRP, in which TMB acts as the hydrogen donor for the reduction of H_2O_2 (Figure 5.4) [235]. This reaction involved electron transfer which was then recorded as amperometric signal by autolab.
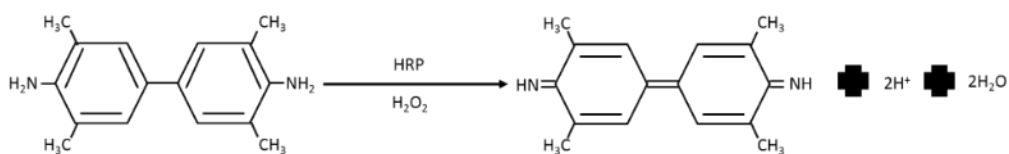
Figure 5.4: Reaction mechanism for the HRP catalysed oxidation of TMB in the presence of H_2O_2 [235].

In order to generate a standard measurement, threshold limit of each sensor was determined to eliminate any background signal. Besides, the threshold limits also serve as a standard to discriminate between positive and negative samples, where the amperometric signals above the threshold will be interpreted as a positive response and vice versa. After serial testing of no template and buffer negative controls, the threshold limits for the three sensors are listed in Table 5.2.

Table 5.2: Threshold limits for different sensors used to generate a standard measurement.

Sensor (SPCE)	Threshold limit (μA)
Bare	10.6 ± 1.06
G/PSE-modified	8.40 ± 0.84
G/ZnO/PSE-modified	8.71 ± 0.87

The accuracy of the electrochemical genosensor for the *H5* PCR product was assessed by comparing the samples according to the threshold limit. Figure 5.5A shows that the current responses of all sensors were concentration-dependent. The increase in the dilution factor of PCR amplicon resulted in decreasing current response. This decrease in current response is due to lower amount of binding sites (fluorescein label of PCR amplicon) available for the attachment of HRP-conjugated anti-fluorescein antibody in the sensing platform (Figure 5.1B). Therefore, lower amount of HRP was present to catalyse the oxidation of TMB, subsequently yielding a decrease in the current signal. The result is clearly displayed in Figure 5.5B, showing a linear correlation between PCR amplicon concentration and amperometric signal.

In general, all three sensors demonstrated obvious current responses that were well distinguishable between positive and negative samples of *H5* gene according to the respective threshold limits. Furthermore, all genosensors showed good sensing capability towards the detection of *H5* PCR amplicon at different concentrations. In particular, the G/ZnO/PSE-modified genosensor displayed the highest sensitivity, with a good correlation coefficient, r^2 of

0.9716 (Figure 5.5B). The enhanced electrochemical performance of the G/ZnO/PSE-modified sensor could be attributed to the large surface area-to-volume ratio of graphene and electroactive property of ZnO, thus improving the electron transfer process [195].

In order to qualitatively analyse the sensing performance of the genosensors, analysis of variance (ANOVA) was performed and the results are presented in Figure 5.5A and Table 5.3. From the Fisher's protected least significant difference (LSD) test as shown in Figure 5.5A, it was observed that the interaction between G/ZnO/PSE-modified genosensor and non-diluted *H5* PCR amplicon displayed higher current response than other interactions. In addition, the LSD test also indicated that the G/ZnO/PSE-enhanced genosensor showed the highest significance for the detection of non-diluted *H5* PCR amplicon than other diluted PCR amplicons as indicated by the letter "a" in Figure 5.5A. It was also observed that bare genosensor is not significant in the detection of different dilution factors as all dilution factors were represented by the same letter, *gh* and *h*. On the contrary, the current responses of both graphene- and G/ZnO-modified genosensors towards PCR amplicons of different dilution factors were significantly different ($P < 0.001$), demonstrating the enhanced electrochemical performance of modified SPCE as compared to bare SPCE.

The result of two-way analysis of variance is shown in Table 5.3. The result showed significant main effect for both dilution factor and sensor type, $F_{(5, 36)} = 18.58$, $P < 0.05$ and $F_{(2, 36)} = 62.94$, $P < 0.05$, respectively. Besides,

results also showed that the interaction between dilution factor and sensor was significant, $F_{(10, 36)} = 3.60$, $P < 0.05$. These analyses demonstrated that the effect of modification of sensor with material is significant, as the difference in the current responses obtained from different genosensors is obvious. The result also suggests that modification of genosensor with G/ZnO nanocomposite significantly enhanced the detection sensitivity, yielding a highly sensitive sensing platform for *H5* gene.
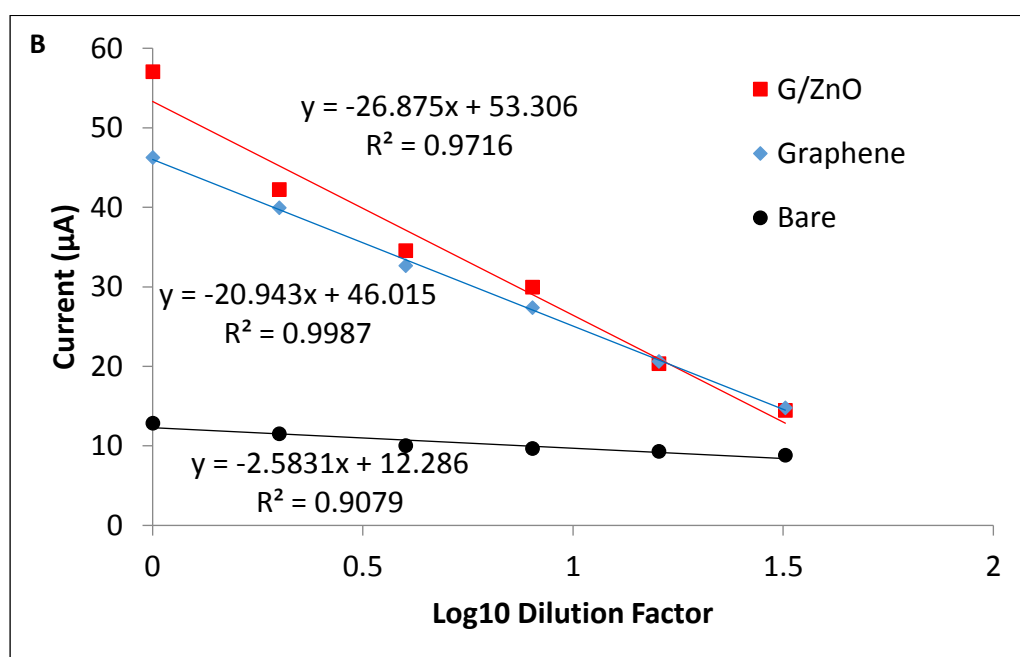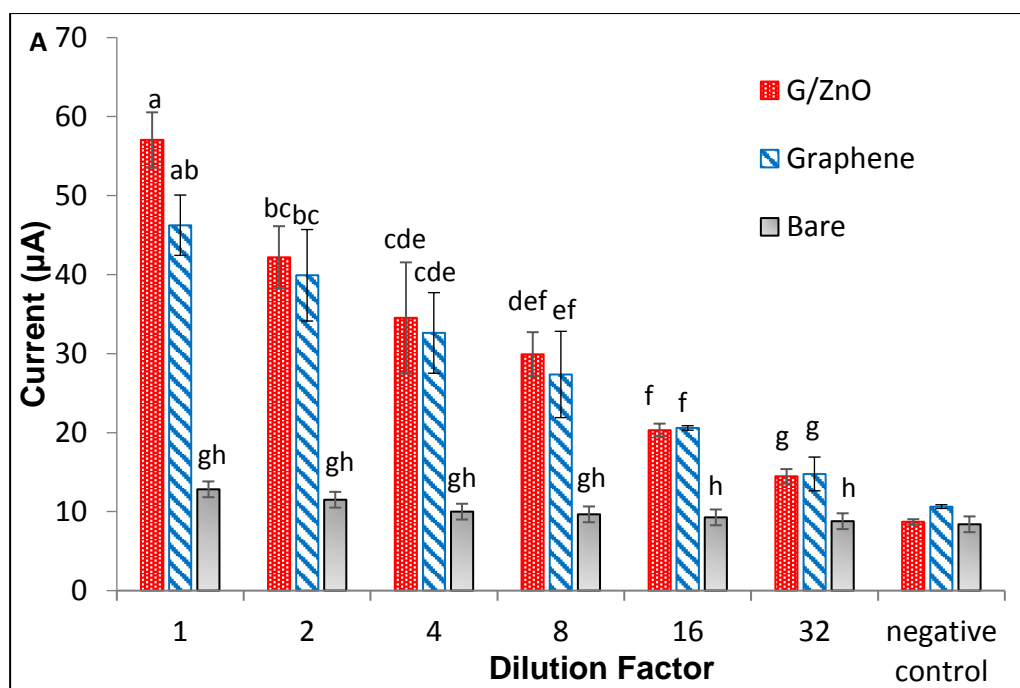
Figure 5.5: (A) Amperometric responses of bare, G/PSE- and G/ZnO/PSE-modified electrochemical DNA biosensors with different dilutions of *H5* PCR amplicon (mean ± SD (n=3)), error bars were plotted according to the SD of each triplicate, different letters indicate differences among dilution factors as determined by Fisher's protected least significant different (LSD) test at *P* = 0.05. (B) Plot of current signals against different dilution factors of *H5* PCR amplicon.

Table 5.3: Results of the two-way analysis of variance (ANOVA) with dilution factor at 6 levels and sensor type at 3 levels replicated 3 times in a completely randomised design (CRD).

Source of variation	Degree of freedom	Sum of square	Mean square	Computed F value	Probability value
Dilution factor	5	4.080×10^{-9}	8.160×10^{-10}	18.58	<0.001
Sensor type	2	5.529×10^{-9}	2.764×10^{-9}	62.94	<0.001
Dilution factor x Sensor type	10	1.581×10^{-9}	1.581×10^{-10}	3.60	0.002
Residual	36	1.581×10^{-9}	4.393×10^{-11}		
Total	53	1.277×10^{-8}			

5.3.3 Verification of Developed Sensing Platform

Dot blot assay was performed to investigate the feasibility of the sensing platform, where TMB acts as the visualising reagent for the observation of colorimetric change. TMB is oxidised during the reduction of H_2O_2 catalysed by HRP, forming a one-electron oxidation product, resulting in blue aggregates as observed (Figure 5.4). The intensity of the blue aggregates is dependent on

the concentration of HRP, lower HRP concentration leads to lower blue intensity in the dot blot assay and vice versa. As observed in Figure 5.6, increasing the dilution factor of the PCR amplicon resulted in a decrease in blue dot intensity, while negative control displayed no colorimetric response. This is due to higher dilution factor possesses lower amount of fluorescein-labelled PCR amplicon for the binding of anti-fluorescein HRP, resulting in lesser redox reactions of TMB and H_2O_2 in the dot blot assay. The dot blot assay affirms the feasibility of the sandwich platform, in which the biotin-labelled PCR amplicon was successfully bound to streptavidin via non-covalent biological interaction, while the anti-fluorescein HRP was bound to fluorescein-labelled PCR amplicon that was fixed onto the streptavidin blotted membrane [233]. Therefore, the PCR amplicon acts as the link between streptavidin and HRP, indicating the enzymatic reactions are proportional to the labelled PCR amplicon concentrations, with formation of blue aggregates as the direct indicator for the reaction. In addition, the dot blot result obtained is in agreement with that of G/ZnO nanocomposite-enhanced genosensor, thereby complementing the genosensing assay.
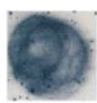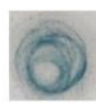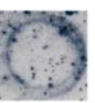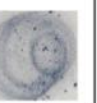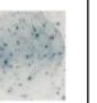
Dot Blot Assay	Non-diluted PCR amplicon	½ diluted PCR amplicon	¼ diluted PCR amplicon	$1/_8$ diluted PCR amplicon	$1/_{16}$ diluted PCR amplicon	$1/_{32}$ diluted PCR amplicon	Negative control

Figure 5.6: Dot blot assay results for *H5* gene PCR amplicon performed at the dilution factors of 1, 2, 4, 8, 16, 32, respectively and negative control.

The detection of *H5* PCR amplicon by electrochemical genosensor was compared with the conventional method of PCR amplicon detection, i.e. agarose gel electrophoresis. The fluorescence signals observed from gel electrophoresis for PCR products subjected to dilution factors of 1, 2, 4, 8, 16 and 32 (L1-L6) are shown in Figure 5.7. The fluorescence signals obtained were in agreement with the current signals detected by the genosensor, in which the signals weakened with increasing dilution factors. No obvious fluorescence signal was observed for PCR samples with dilution factors of 8 and above. Comparatively, the current response of the G/ZnO/PSE-enhanced genosensor was still significant ($P < 0.05$) when the PCR amplicon was subjected to dilution factor of 32 (Figure 5.5A), exhibiting approximately 5 times better sensitivity than the conventional gel electrophoresis. Furthermore, G/ZnO nanocomposite-enhanced genosensor generates quantifiable result, requires low sample consumption and excludes handling of carcinogenic agent. Therefore, the G/ZnO/PSE-modified genosensor showed promising results with its facile and rapid measurement which is vital for the detection and identification of this deadly disease.
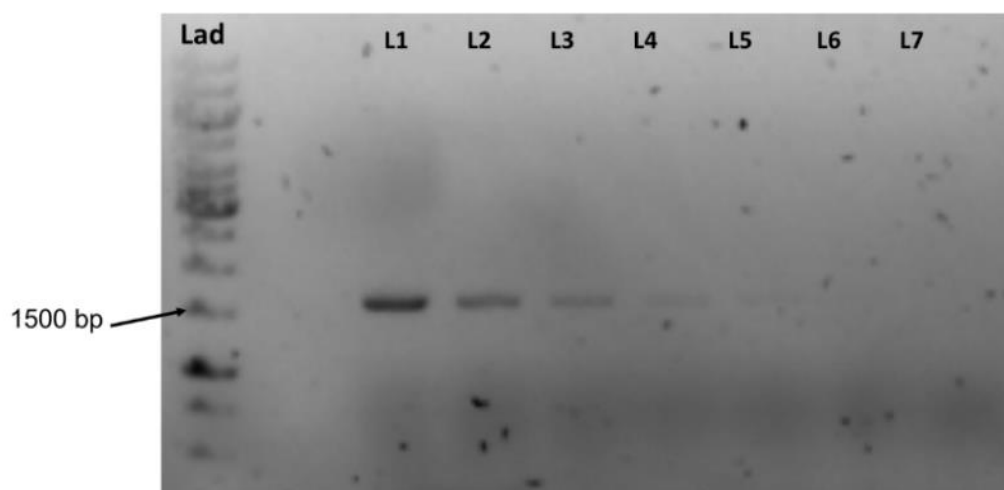
Figure 5.7: Agarose gel electrophoresis with different dilutions of *H5* gene PCR amplicon. Lad – 1 kbp DNA ladder (250, 500, 750, 1000, 1500, 2000, 2500, 3000, 4000, 5000, 6000, 8000 and 10000 bp); L1-L6 – PCR product with different dilution factors of 1, 2, 4, 8, 16 and 32; L7 – negative control.

5.4 Chapter Summary

In this study, a sandwich sensing platform was proposed for the detection of Avian Influenza *H5* gene. Two different methods were used for the binding of streptavidin onto the sensors, namely EDC/NHS crosslinking for bare SPCE and pi-pi stacking with PSE for graphene and G/ZnO-modified SPCE. Different dilutions of *H5* PCR amplicon were applied onto the sensing platform to evaluate the sensitivity of the developed sensors. Threshold limit was also determined for each sensor to eliminate background signal for a standard measurement. As a result, the G/ZnO nanocomposite-modified electrochemical DNA biosensor displayed a good sensitivity towards the detection of *H5* gene PCR amplicon, with a good correlation coefficient, r^2 of 0.9716. The ANOVA analysis indicated that the effects of both material

modification and PCR amplicon concentration are significant towards generating the current response of the sensor. Dot blot assay was performed for the verification of the sandwich sensing platform and the result was fascinatingly positive. Detection of different dilutions of *H5* gene PCR amplicon was also carried out with agarose gel electrophoresis for comparison of sensing performance with the electrochemical genosensor. The G/ZnO/PSE-enhanced SPCE displayed approximately 5 times better sensitivity than the conventional gel electrophoresis, showing a proof of concept which can be investigated further for the development of an early and rapid detection tool for the avian influenza H5N1 virus. The sandwich platform developed in the present study is highly versatile as it can be employed for DNA detection and any other biological compound via the antigen-antibody interaction. This electrochemical enzyme-based DNA biosensor technique can be utilised for the detection of other DNA sequence by changing to specific primer sequences, enabling a rapid identification of diseases. The G/ZnO/PSE-enhanced genosensor used in this study is novel and universal as it can detect biotin- and fluorescein-labelled PCR amplicon derived from any organisms or mutant gene to facilitate an early and accurate diagnosis.

Chapter 6 Sensitivity Enhancement of Graphene/Zinc Oxide Nanocomposite-based Electrochemical Impedance Genosensor for Single Stranded RNA Detection

6.1 Overview

Chapter 5 demonstrated the development of a highly versatile sandwich sensing platform based on G/ZnO nanocomposites, for the detection of Avian Influenza *H5* gene. The Avian Influenza *H5* gene was amplified and tagged with biotin-fluorescein label via PCR, in which the PCR amplicon was bound onto the G/ZnO/PSE-modified SPCE via streptavidin. Different dilutions of *H5* PCR amplicon were applied onto the sensing platform to evaluate the sensitivity of the developed sensors. The G/ZnO nanocomposite-modified electrochemical DNA biosensor successfully displayed a good sensitivity towards the detection of *H5* gene PCR amplicon, demonstrating approximately 5 times better sensitivity than the conventional gel electrophoresis.

The fabrication of sandwich sensing platform described in Figure 5.1 enabled the detection of double stranded PCR amplicon. In this chapter, an improved sensing platform based on G/ZnO nanocomposite for the detection of single stranded viral RNA is presented.

Coconut cadang-cadang viroid (CCCVd, family *Pospiviroidae*, genus *Cocadviroid*) causes a lethal disease to coconut palm (*Cocos nucifera* L.), amounting an estimated death of over 40 million coconut palms, resulting in an annual yield loss of approximately 22000 tonnes of copra since its first

recognition [236]. Although early attempts of CCCVd eradication have been carried out since early of 1950s, these viroids spread naturally and their epidemiology is poorly understood, thus, up to date, no direct control measures are currently available. In addition, the oil palm CCCVd variants are difficult to detect since they generally present in low concentration in the palm tissues. This renders typical molecular detection techniques such as polyacrylamide gel electrophoresis (PAGE), hybridisation assay and conventional reverse transcription-polymerase chain reaction (RT-PCR) becoming ineffective [237]. Although ribonuclease protection assay (RPA) has been proposed as an alternative for the detection of CCCVd, its major drawback is the utilisation of radioactive probe [238].

With the excellent properties of G/ZnO nanocomposite, this chapter reports on a simple, efficient and highly sensitive G/ZnO nanocomposite-based electrochemical biosensor for a proof of concept detection of single stranded CCCVd RNA. The electrochemical detection of CCCVd sequence is based on the impedance changes upon a hybridisation event between both the chemically synthesised single stranded RNA (ssRNA) target and the complementary single stranded DNA (ssDNA) probe functionalised on the sensor electrode platform.

6.2   Experimental Details

6.2.1   Materials

Phosphate buffer saline (PBS) tablet, potassium ferricyanide ($K_3[Fe(CN)_6]$), 1-pyrenebutyric acid N-hydroxysuccinimide ester (PSE) and methylene blue (MB) were purchased from Sigma Aldrich (St. Louis, USA). The

synthetic oligonucleotides, namely the 5'-amine terminated single stranded DNA (ssDNA) probe (complementary to CCCVd genomic RNA sequence), CCCVd genomic ssRNA (ssRNA) target, single-based mismatched ssRNA strand (msRNA1), double-base mismatched ssRNA strand (msRNA2) and non-target ssRNA (ntRNA) strand were purchased from Helix Biotech (Selangor, Malaysia) with sequences listed as follows:

Amino-modified ssDNA probe (ssDNA):

5'-NH_2-CCAGATTCGTTTGAGGTTTCCCCGG-3'

CCCVd genomic ssRNA target (ssRNA):

5'-CCGGGGAAACCUCAAACGAAUCUGG-3'

Single-base mismatched ssRNA strand (msRNA1):

5'-CCGGGGAAACCUCAAACGAAUCUG<u>U</u>-3'

Double-base mismatched ssRNA strand (msRNA2):

5'-CCGGGGAAACCUCAAACGAAUCU<u>UA</u>-3'

Non-target ssRNA strand (ntRNA):

5'- CAGGGCACCCCAAAAACUACUGC-3'

The ssRNA target sequence is located at the region of 60 to 84 nucleotides (nt) from the 5'-terminus of CCCVd (GenBank accession number: DQ097183). The hybridisation processes were carried out in the presence of 0.1 M PBS buffer prepared with sterile, nuclease free water. All aqueous

solutions were prepared using autoclaved Milli-Q water, with resistivity of 18.2 MΩcm^{-1} (Millipore Corporation, USA). Reagents and solvents were of analytical grade and used without further purification. All experiments were carried out at room temperature.

6.2.2 Fabrication of Electrochemical Impedance Genosensor

The preparation of PSE-functionalised G/ZnO nanocomposites (G/ZnO/PSE) was detailed in Section 5.2.2. The G/ZnO/PSE dispersion (5 µL) was drop casted onto SPCE (DropSens, Spain) and air-dried to obtain G/ZnO/PSE-modified SPCE.

The fabrication of electrochemical impedance genosensor based on G/ZnO nanocomposite was performed at room temperature as shown in Figure 6.1. The ssDNA probe (5 µL, 20 mM) was drop casted on the surface of the G/ZnO/PSE-modified SPCE and incubated for 1 hour. The modified electrode was rinsed with deionised (DI) water and air-dried to form G/ZnO/PSE/ssDNA-modified SPCE. The hybridisation procedure was performed by pipetting ssRNA target (5 µL, 20 mM) onto G/ZnO/PSE/ssDNA-modified SPCE and incubated for 1 hour. Lastly, the hybridised electrode (G/ZnO/ssDNA/ssRNA-modified SPCE) was rinsed with DI water to remove non-specifically adsorbed ssRNA.
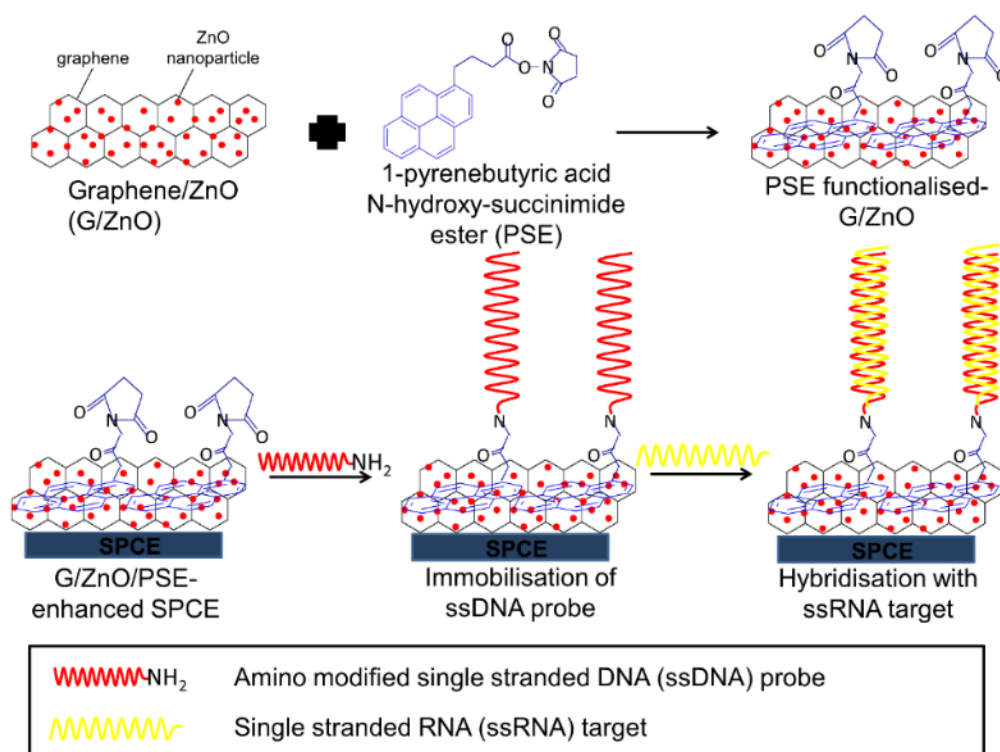
Figure 6.1: Schematic diagram for the development of electrochemical impedance genosensor for ssRNA detection.

6.2.3 Electrochemical Measurements of the Genosensor

All electrochemical measurements were carried out on µAutolab PGSTAT III potentiostat (Metrohm, Netherlands) interfaced with controlling software NOVA 1.10. Electrochemical impedance spectroscopy (EIS) measurement were tested with as-prepared biosensor in 10 mM PBS buffer with 10 mM $K_3[Fe(CN)_6]$ as the electrochemical probe. 100 mV amplitude of sine voltage signal was applied to the three electrode system under open circuit potential (OCP), and the frequency varied from 0.1 Hz to 10 kHz. Cyclic voltammetry (CV) measurements were performed from -0.4 V to 0.7 V at a scan rate of 50 mV/s.

The biosensor was prepared for differential pulse voltammetry (DPV) analysis by immersing into 10 mM PBS buffer containing 50 µM of methylene blue (MB) for 30 minutes to sufficiently accumulate MB molecules. The biosensor was then rinsed with excessive blank PBS buffer to remove non-specifically bound MB molecules before being analysed immediately in MB-free PBS buffer. DPV was recorded within the potential range from -0.6 V to -0.2 V under pulse amplitude of 50 mV, pulse width of 0.05 s, pulse period of 0.2 s and an increasing potential of 4 mV.

6.3 Results and Discussion

6.3.1 Electrochemical Characterisation of the Developed Sensor

The electrochemical performances of bare, graphene- and G/ZnO nanocomposite-modified electrodes were compared via cyclic voltammetry (CV) using 10 mM $[Fe(CN)_6]^{3-/4-}$ as probe (Figure 6.2A). As shown in Figure 6.2A, a pair of well-defined redox peaks was observed for all three modified electrodes. These redox peaks correspond to the $K_3Fe(CN)_6$ electron transfer process, with a peak to peak separation (ΔEp) of 150 mV. For the G/ZnO-modified electrode, a sharp increase of peak current response of approximately 4 times was observed, when compared to the bare electrode. In addition, the G/ZnO-modified electrode also demonstrated a better electrochemical response when compared to the graphene-modified electrode.

The Electrochemical Impedance Spectroscopy (EIS) was also used to characterise the different modified electrodes (Figure 6.2B). From the Nyquist plot, the charge transfer resistance, R_{ct} for bare electrode was 2150.3 Ω. After

modification with graphene and G/ZnO nanocomposite, the R_{ct} values were reduced to 1817.8 Ω and 1241.3 Ω, respectively. The decreasing R_{ct} values in the order of bare > graphene- > G/ZnO nanocomposite- modified electrodes indicates the better performance of G/ZnO-modified electrode, which is in agreement with the CV results. The enhanced electrochemical properties of G/ZnO nanocomposite could be attributed to the synergistic effect between graphene and ZnO nanoparticles, in which the good electron conductor, graphene coupled with ZnO nanoparticles, improved the charge transfer between the materials, thereby resulting in a higher electrocatalytic response [195].
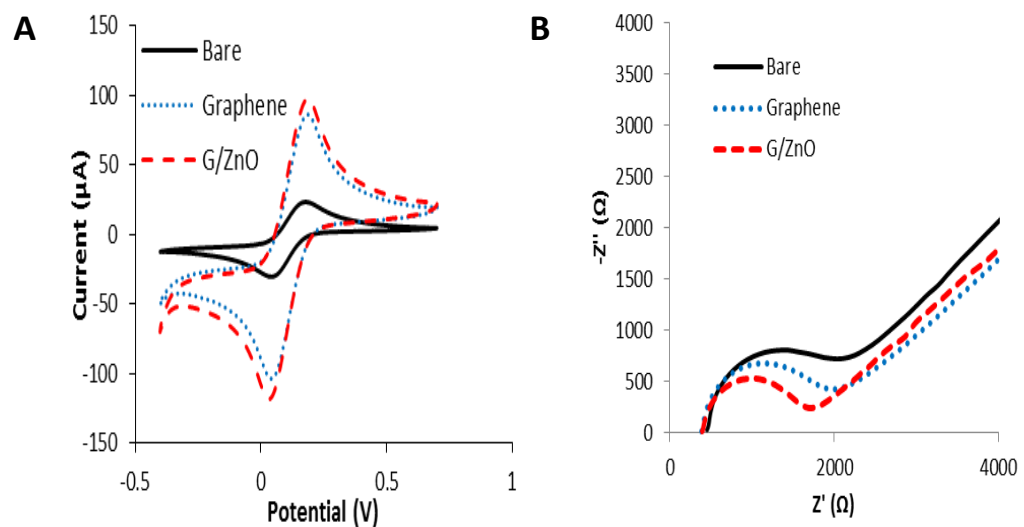
Figure 6.2: CVs (A) and Nyquist diagram (B) of bare, graphene and G/ZnO nanocomposite-modified electrode for electrochemical characterisation of electrodes with different modifications.

The development of highly versatile sensing platform based on G/ZnO nanocomposite was described in Session 5.3.2, where PSE was used as a bi-linker for the attachment of biological compound. This simple organic bi-linker

consists of a pyrene moiety and succinimidyl fragment, enables strong irreversible non-covalent binding to the surface of graphene via π-π hydrophobic stacking that does not disrupt the pristine structure of graphene. The succinimidyl ester at the other end allows the bonding to amine group on biological surface.

The ssDNA probe has been amino-modified and thus consists of an amine ($-NH_2$) functional group. Therefore, the ssDNA probe can be immobilised onto G/ZnO/PSE-modified electrode through covalent bonding. The ssRNA target was then applied to the G/ZnO/PSE/ssDNA-modified electrode for hybridisation between complementary ssDNA probe and ssRNA target. These assembly steps were both examined using CV and EIS with $[Fe(CN)_6]^{3-/4-}$ as the reactive probe (Figure 6.3). The CV analysis showed that upon modification with the PSE bi-linkers, the redox peak current decreased compared to that of G/ZnO-modified electrode, indicating the successful functionalisation of G/ZnO with PSE. The decrease in current response may be due to the hydrophobic property of PSE and the formation of a physical barrier that hinders the electron transfer to the electrode surface [239].

Comparatively, a further decrease in peak current response with larger redox peaks separation was observed for G/ZnO/PSE/ssDNA-modified electrode. The result suggests that the redox reversibility of $[Fe(CN)_6]^{3-/4-}$ became poorer upon the successful immobilisation of the ssDNA probe, likely attributed to the negative charged phosphoric acid groups on the ssDNA probe interfered the diffusion of electronegative $[Fe(CN)_6]^{3-/4-}$ to the electrode

surface [240]. When the ssDNA probe hybridised with ssRNA target, the peak current of G/ZnO/PSE/ssDNA/ssRNA-modified electrode decreased further, due to the presence of additional negative charged phosphoric acid groups immobilised on the electrode surface. These modification steps were further examined using electrochemical impedance spectroscopy (EIS), a proven powerful tool in assessing the interfacial properties of conductive or semi-conductive surfaces.

EIS is typically employed for sensitively studying bio-recognition events at the electrode surface [241]. Figure 6.3B depicts the corresponding EIS of the G/ZnO nanocomposite-modified genosensor. The impedance spectra obtained were interpreted by fitting with a Randles equivalent circuit of $R_s[(R_{ct}W)Q]$ (the schematic of the circuit was included as inset in Figure 6.3B). The G/ZnO/PSE-modified electrode showed increased R_{ct} from 1241.3 Ω to 3236.8 Ω, depicting the successful functionalisation of G/ZnO nanocomposite with PSE. After covalent immobilisation of ssDNA probe on the electrode surface, R_{ct} of G/ZnO/PSE/ssDNA-modified electrode continually increased, reaching a value of 4542.9 Ω. Upon one hour of hybridisation with 20 µM of ssRNA target, R_{ct} of G/ZnO/PSE /ssDNA/ssRNA-modified electrode further increased to 4820.9 Ω. The results obtained from both CV and EIS evidently demonstrated the success of each modification step, and subsequently the detection of ssRNA by the sensor platform.
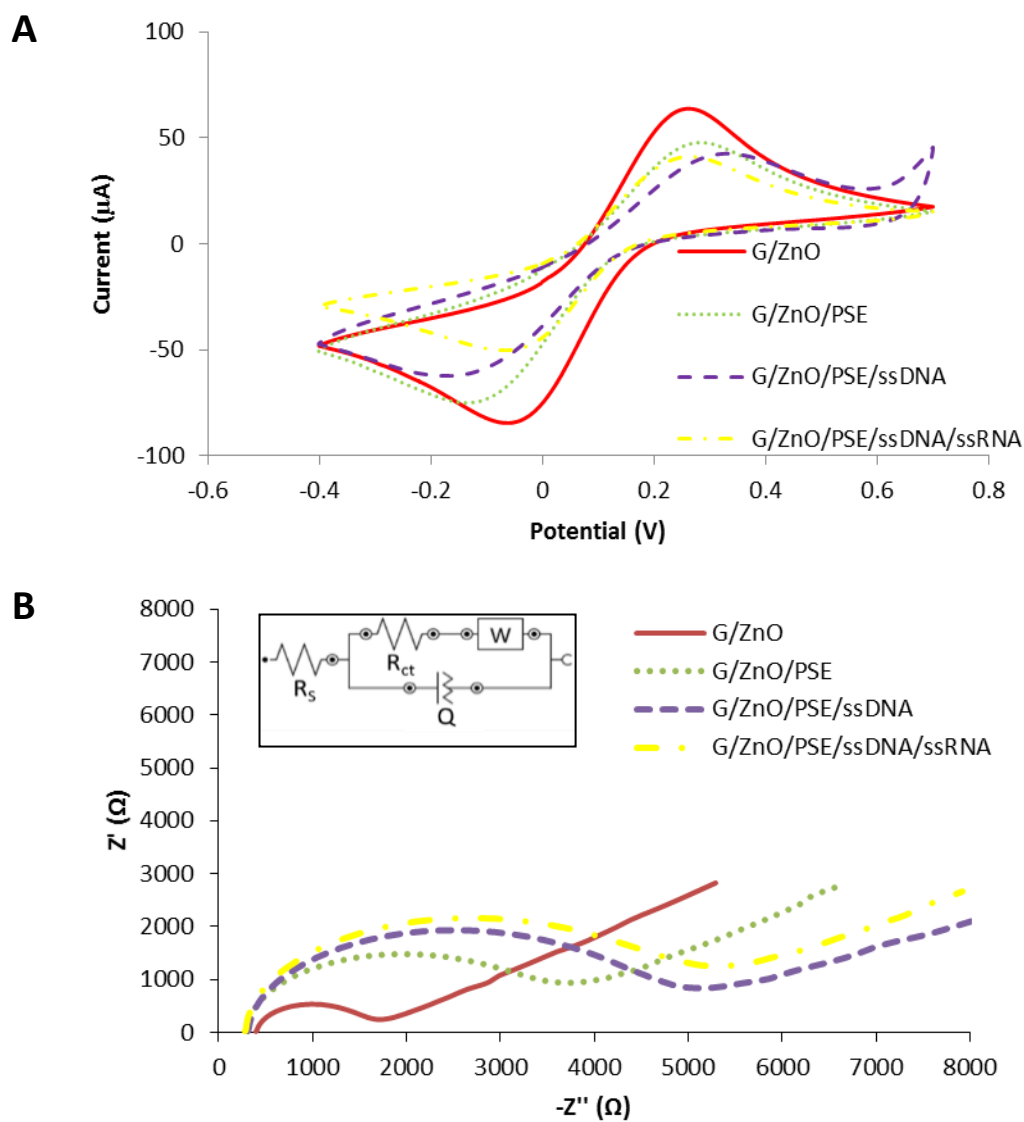
Figure 6.3: CVs (A) and corresponding Nyquist diagrams (B) of G/ZnO-, G/ZnO/PSE-, G/ZnO/PSE/ssDNA- and G/ZnO/PSE/ssDNA/ssRNA-modified SPCE, in 10 mM PBS buffer containing 10 mM $K_3Fe(CN)_6$. Inset: Equivalent circuit used to fit the experimental data, R_s, Q, R_{ct} and W represent the resistance of electrolyte solution, value of constant phase element, charge-transfer resistance and Warburg impedance, respectively.

6.3.2 Optimisation of Sensing Conditions

In order to optimise the condition for efficient detection, different parameters such as hybridisation time and temperature were investigated. The effect of hybridisation time on EIS signals of G/ZnO/PSE/ssDNA/ssRNA-modified electrode are shown in Figure 6.4A and B. The ssDNA functionalised G/ZnO/PSE-modified electrode was incubated in 5 µL of 20 µM ssRNA at 24 °C for varying incubation periods from 10 to 70 minutes. Results showed that the R_{ct} increased rapidly with longer hybridisation time from 10 to 60 minutes, and reached a saturation after 60 minutes. The saturated signal may be the result of complete hybridisation of ssRNA target with all available ssDNA probes anchored on the sensor platform. As such, considering sensitivity and assay time, the optimum hybridisation time chosen was 60 minutes.

The effect of hybridisation temperature was carried out by incubating G/ZnO/PSE/ssDNA-modified electrode with 5 µL of 20 µM ssRNA target for 60 minutes at different temperatures ranging from 24 °C to 40 °C. Results showed that as hybridisation temperature increased from 24 °C to 28 °C, the R_{ct} value also increased, depicting a higher amount of detected ssRNA target by the sensor platform. However, a further increase in hybridisation temperature above 28 °C resulted in the decrease of R_{ct} value (Figure 6.4C and D). This could be due to the effect of temperature on the thermodynamic properties for DNA/RNA duplex formation, thereby affecting the hybridisation efficiency between ssDNA strand and ssRNA target [242]. Consequently, the optimised hybridisation temperature adopted for the biosensor was 28 °C.
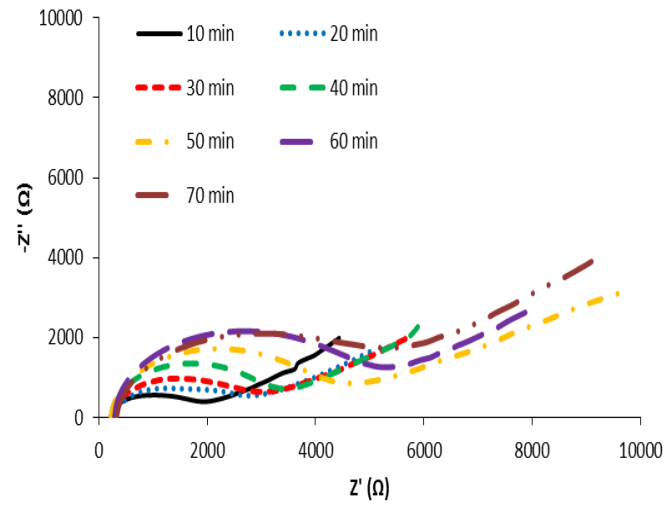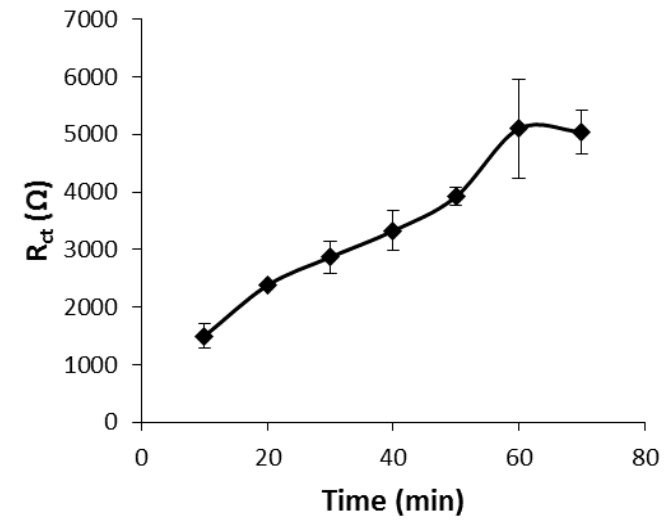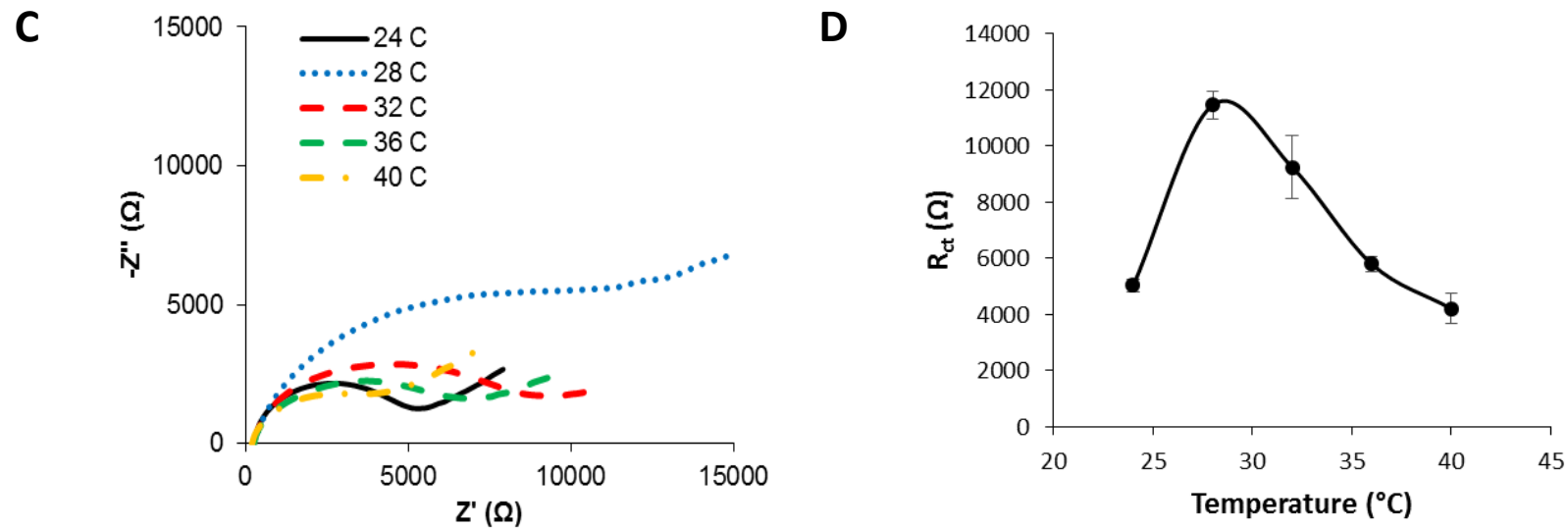
Figure 6.4: Effects of hybridisation time (A), calibration curve of R_{ct} versus hybridisation time (B), hybridisation temperature (C) and calibration curve of R_{ct} versus hybridisation temperature (D) on R_{ct} of G/ZnO/PSE/ssDNA/ssRNA-modified SPCE. The optimum hybridisation time and temperature for G/ZnO/PSE-modified electrode were 60 minutes and 28 °C, where the impedance value was observed at the maximum.

6.3.3 Performance of the Developed Sensor

Based on the parametric optimisation study (Figure 6.4), the experimental results showed that the best hybridised time and temperature for the developed G/ZnO/PSE-enhanced biosensor were 60 minutes and 28 °C, respectively. Under optimal sensing conditions, the analytical performance of the impedance biosensor was examined using the G/ZnO/PSE/ssDNA-modified electrode to detect ssRNA target of different concentrations, ranging from 1×10^{-11} M to 1×10^{-6} M (Figure 6.5). Results showed that the developed sensor had successfully detected the specific CCCVd ssRNA target with signal response increased proportionally with increasing target concentrations at a correlation coefficient of 0.9927 (Figure 6.5 inset). The limit of detection was estimated to be 4.3×10^{-12} M (S/N = 3). Table 6.1 lists the sensor performance comparison between the developed sensor and other modified electrodes. As it can be seen from Table 6.1, the performance of the developed electrochemical impedance genosensor is comparable to other reported work with a relatively wide dynamic range [243-247].
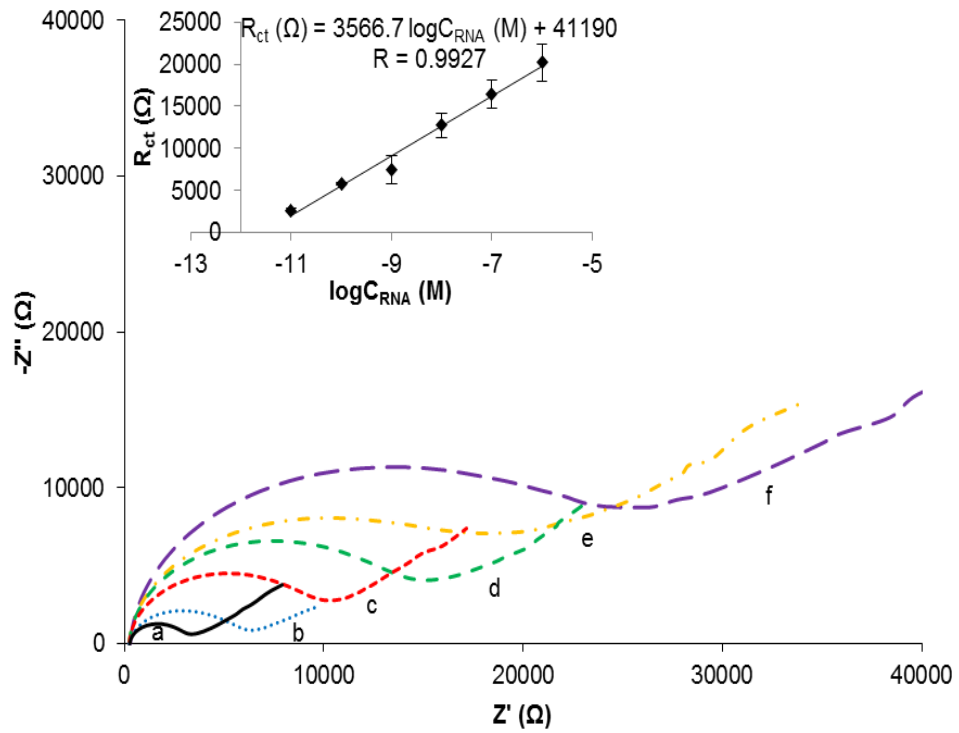
Figure 6.5: Nyquist diagrams recorded by G/ZnO/PSE/ssDNA-modified electrode after hybridisation with different concentrations of ssRNA target: 1 x 10^{-11} M (a), 1 x 10^{-10} M (b), 1 x 10^{-9} M (c), 1 x 10^{-8} M (d), 1 x 10^{-7} M (e) and 1 x 10^{-6} M (f) in 10 mM PBS buffer containing 10 mM K$_3$Fe(CN)$_6$. Inset shows the corresponding calibration curve of the biosensor.

Table 6.1: Comparison on the performance of different sensors using EIS.

Platform	Linear Range (M)	Detection Limit (M)	Reference
NH$_2$-G$_4$PAMAM dendrimers	1×10^{-11} - 1×10^{-8}	3.8×10^{-12}	[243]
Au/PDC membranes	1×10^{-10} - 1×10^{-5}	2.4×10^{-11}	[244]
Au/TB-GO	1×10^{-11} - 1×10^{-9}	2.9×10^{-12}	[245]
ZnO-CNT/ITO	$5 - 180$ ng µL^{-1}	-	[247]
Graphene	8×10^{-9} - 1×10^{-7}	5.0×10^{-9}	[246]
Graphene/ZnO/PSE	1×10^{-11} - 1×10^{-6}	4.3×10^{-12}	Current study

6.3.4 Selectivity of the Developed Sensor

Selectivity is a crucial factor to evaluate the performance of a DNA biosensor. Therefore, the selectivity of the developed sensor platform was evaluated with 20 µM of various RNA oligonucleotides and their respective recorded R_{ct} values were compared to that of hybridisation with target ssRNA (Figure 6.6). EIS analysis results showed that upon the introduction of non-target ssRNA (ntRNA), the R_{ct} value recorded (4487.5 Ω) was negligible, with respect to the R_{ct} value of unhybridised electrode (G/ZnO/PSE/ssDNA) (4542.9 Ω), suggesting that no hybridisation took place. The single- (msRNA1) and double- (msRNA2) base mismatched ssRNA sequences exhibited lower impedance responses, with recorded R_{ct} values of 29768 Ω and 23809 Ω,

respectively as compared to that of G/ZnO/PSE/ssDNA-modified electrode hybridised with ssRNA target (34800 Ω). These results indicate that the developed sensor platform has a good hybridisation selectivity to discriminate the specific target from the non-target RNA and mismatched ssRNA target sequences down to a single base mismatch.
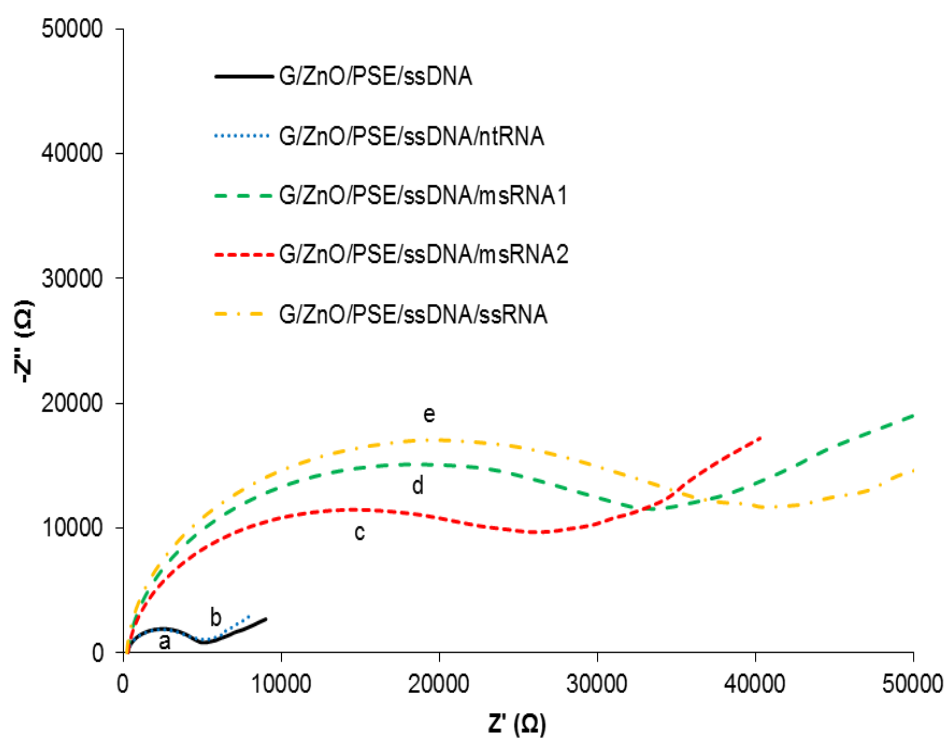
Figure 6.6: Nyquist plots of the G/ZnO/PSE/ssDNA-modified (a) electrode hybridised with (b) non-target ssRNA, (c) double-base mismatched ssRNA strand (msRNA2) and (d) single-based mismatched ssRNA strand (msRNA1) and (e) ssRNA target. The hybridisation between G/ZnO/PSE/ssDNA-modified electrode with ssRNA target generated a higher impedance signal than that of mismatched sequences (msRNA1 and msRNA2) while hybridisation with ntRNA resulted in no change of impedance, indicating no hybridisation at all.

To investigate the reproducibility, five G/ZnO/PSE/ssDNA-modified electrodes were prepared in parallel and hybridised with 20 µM of ssRNA target, respectively. An acceptable relative standard deviation (RSD) of 7.5% (n = 5) for the R_{ct} value was obtained, which shows the good reproducibility of the ssRNA detection. The stability of the developed sensor was studied by preserving the G/ZnO/PSE/ssDNA-modified electrode at 4 °C for 7 days. The hybridisation process was carried out by dropping 20 µM of ssRNA target onto the preserved G/ZnO/PSE/ssDNA-modified electrode and incubated for 1 hour. EIS was performed under optimised conditions and upon comparing the response signals between the freshly prepared and preserved sensors, the preserved one displayed only 2.2% decrement in response signal, thus demonstrating a good stability.

6.3.5   Estimation of ssDNA Probe Accumulation via Methylene Blue

Methylene blue (MB), 3,7-bis(dimethylamino)phenothiazin-5-ium-chloride, is an organic dye belonging to the phenothiazine family. MB is frequently used as electroactive marker, as it can interact with nucleic acids via electrostatic attraction or intercalation into double stranded DNA (dsDNA), and exhibits high affinity towards guanine bases [248]. Therefore, MB was used as a redox active indicator to double confirm the hybridisation event between the ssDNA probe and ssRNA target via differential pulse voltammetry (DPV), a known sensitive electrochemical measurement technique [249]. Figure 6.7A shows that the electrochemical response of MB molecules increases significantly after incubation of G/ZnO/PSE/ssDNA-modified electrode with

ssRNA target. This could be attributed to the specific intercalation of MB molecules with the formed DNA-RNA duplex, thereby confirming the successful detection of the ssRNA target [249]. Furthermore, the DPV peak currents increased gradually with the increasing complementary ssRNA target concentrations, demonstrating a higher amount of DNA-RNA hybrid which was formed on the electrode surface through hybridisation event (Figure 6.7A). The peak current exhibited a linear correlation with the logarithm values of ssRNA concentrations in the range from 1 x 10^{-11} M to 1 x 10^{-5} M, with a regression equation of I (μA) = 0.0839 $logC_{RNA}$ (M) + 1.0365, r = 0.9640 as displayed in Figure 6.7B. These results are complementary to the EIS result (Figure 6.5), in which, higher impedance signal was observed with increasing amount of ssRNA, confirming the formation of DNA-RNA hybrid on the sensor electrode platform.

Owing to the specific affinity of MB to guanine bases on ssDNA, the surface density of ssDNA probe on the G/ZnO/PSE-modified sensor platform can also be estimated from the current response of MB [250]. Accordingly, it can be deduced that the charge quantity of the reduction process of MB is proportional to the mol quantity of guanine bases on the ssDNA probe. In this work, the charge quantity of MB reduction process obtained from the DPV result was 2.52 x 10^{-6} (n=3) (Figure 6.7A). The mol quantity of MB (N) could be estimated according to the following equation 7.1:

$$N = \frac{Q}{ne\mathrm{NA}}$$
Equation 7.1

where Q is the electric charge quantity of MB reduction process, n is the number of electrons participating in the reaction, to be 2 in this experiment, e

is the electric charge quantity of one electron, to be 1.6 x 10^{-19} C, NA is the Avogadro's number, 6.02 x 10^{23} mol [250]. The surface density of the sensor platform could be calculated from the equation because one MB molecule combined with one guanine base. The ssDNA sequence contained 6 guanine bases in this experiment. The apparent area of the working electrode of the SPCE is 1.26 x 10^{-1} cm^2. Therefore, the surface density of ssDNA on G/ZnO/PSE sensing platform was estimated to be 1.73 x 10^{-11} mol cm^{-2}.
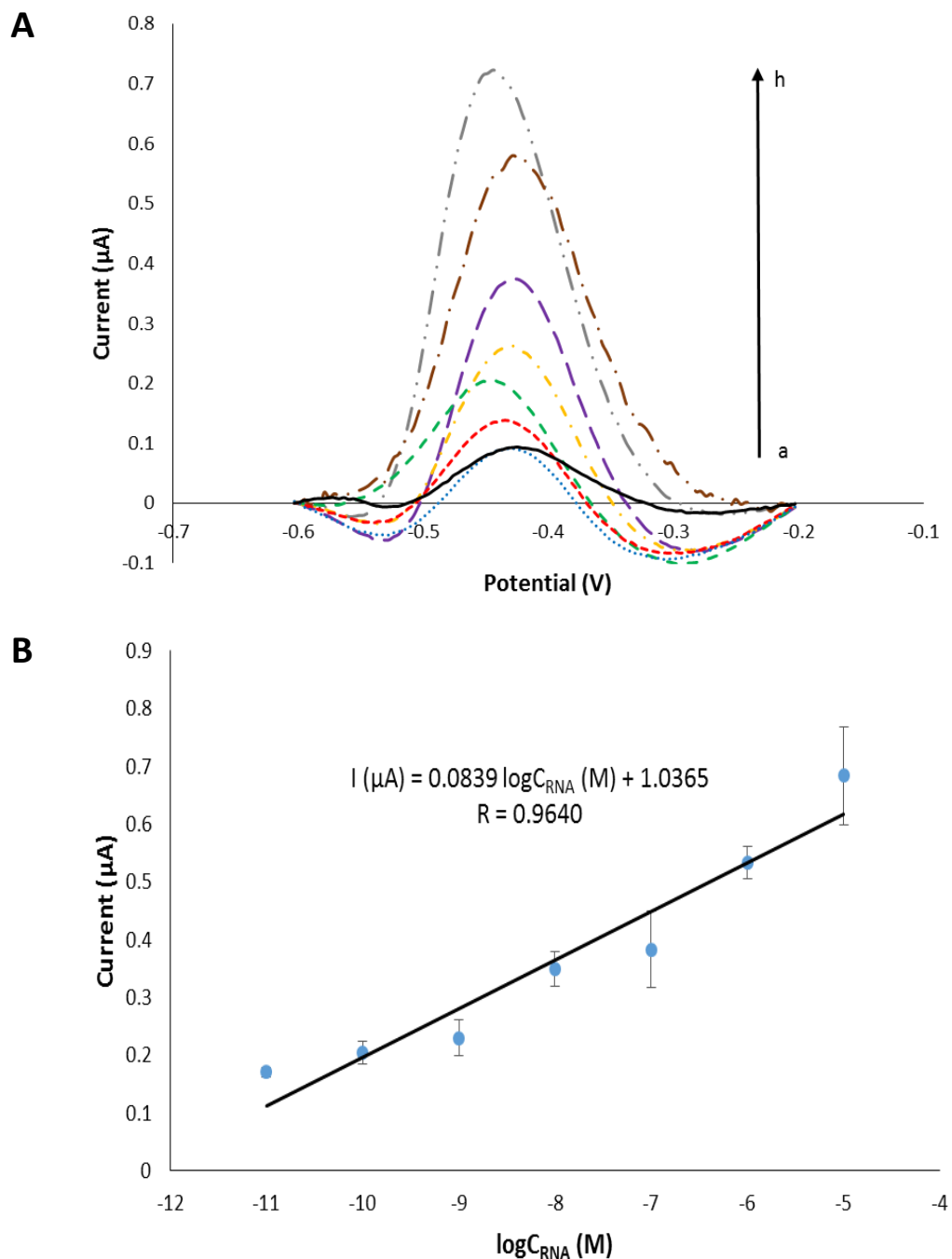
Figure 6.7: (A) DPVs of MB on G/ZnO/PSE/ssDNA-modified electrode before (a) and after hybridisation with different concentrations of ssRNA target: 1 x 10^{-11} M (b), 1 x 10^{-10} M (c), 1 x 10^{-9} M (d), 1 x 10^{-8} M (e), 1 x 10^{-7} M (f), 1 x 10^{-6} M (g) and 1 x 10^{-5} M (h) in 10 mM PBS buffer. (B) Corresponding DPV peak values of the biosensor hybridised with different concentrations of ssRNA target.

6.4 Chapter Summary

In this chapter, a facile and efficient electrochemical impedance genosensor based on PSE-functionalised G/ZnO nanocomposite for sensitive detection of single stranded RNA was successfully fabricated. Electrochemical characterisation results showed that the ssDNA probe can be effectively immobilised on the G/ZnO/PSE-modified sensing platform through covalent binding. Hybridisation event between ssDNA probe and ssRNA target caused changes in impedance and were monitored by EIS technique. DPV with MB as electroactive marker was also performed to verify the formation of DNA-RNA hybrids and to estimate the surface density of ssDNA probe on G/ZnO/PSE sensing platform. CCCVd sequence was used in this work, but these results pave a way for efficient and rapid electrochemical detection of any types of nucleic acid sequences encoded for various diseases. The low limit of detection can be reached without using PCR or any other enzyme-based amplification process. In addition, the developed genosensor presents a good selectivity for discriminating the target sequence from the mismatched and non-target sequences. Due to large specific area, good conductivity and catalytic properties of G/ZnO nanocomposite, a promising sensing platform with good sensitivity and detection limit could be developed for heterologous nucleic acid analyses.

Chapter 7 Conclusion and Future Direction

7.1 Conclusion

For many fatal diseases, the key to their effective treatment and management is to diagnose the diseases at their earliest and pre-symptomatic stage. The ideal diagnostic tool must be simple, easy to use, rapid, highly sensitive and specific, and most importantly affordable. Efforts reported in this work strives towards the aforementioned global health challenge, that is to develop low cost and effective diagnostic tools for early detection of various diseases. Accordingly, the ultimate aim of this research was to develop a versatile, highly sensitive and selective biosensing platform based on graphene/Zinc Oxide nanocomposite (G/ZnO) for early detection of various diseases. Emphasis was put on four very important areas for a feasible biosensor:

(i) The method used to synthesise the electrode material must be simple, cheap and environmental friendly.

(ii) The electrode material used in the fabrication of biosensing platform must possess good conductivity, thereby achieving high sensitivity.

(iii) The developed biosensing platform must be selective, to ensure accurate detection of target molecule.

(iv) The developed biosensing platform should be versatile to enable detection of a wide range of target, demonstrating its feasibility in many applications.

The proposed method to synthesise G/ZnO has successfully eradicate/remove the use of harsh acids and high temperature. A simple, facile and green exfoliation method was used to produce graphene flakes which was then subjected to a low temperature hydrothermal process in the presence of Zinc precursor, to produce the nanocomposite material. The quality and purity of the as produced nanocomposite was confirmed via comprehensive analytical characterisations using scanning electron microscopy (SEM), electron dispersive X-ray spectroscopy (EDS), transmission electron microscopy (TEM), X-ray diffractometry (XRD) and Raman spectroscopy. These results are crucial to demonstrate the quality of G/ZnO, as the presence of defect or functional group will affect the excellent electrical conductivity and electrocatalytic activity of the G/ZnO, which are undesirable for the fabrication of biosensing platform. In additional, electrochemical analysis also confirms that G/ZnO modified electrode platform has better electrochemical performance than graphene modified or bare electrode, as reflected in the increment in sensitivity.

Following this, the as-produced G/ZnO nanocomposites were used as electrode sensing platform for hydrogen peroxide (H_2O_2), which is an important biological analyte due to its presence in various biological reactions and functions. As such, responsiveness towards the detection of H_2O_2 bears a promising future for the biosensing application of the as-synthesised G/ZnO (e.g glucose sensor). It was found that the detection of H_2O_2 was sensitive up to a maximum of 3.2580 μAmM^{-1}, approaching approximately 200% current

response of the control electrode (bare electrode). In the amperometric studies, the G/ZnO-modified electrode displayed excellent selectivity towards interfering species, accurately detecting the target molecule.

With the promising detection of H_2O_2, the ability of this sensor platform to detect biological molecules were further explored. To ensure the specificity of the biosensor, a bi functional linker, 1-Pyrenebutyric acid *N*-hydroxysuccinimide ester (PSE) was used to immobilise the bio-recognition layer on the platform. The functionalisation was achieved via π-π interaction between the pyrene moiety of PSE with the graphitic basal planes of G/ZnO, thus preserving the pristine nature of graphene and its superior electrical conductivity properties. The PSE-functionalised G/ZnO composite was applied for the fabrication of sandwich sensing platform for the detection of Avian Influenza *H5* gene. The G/ZnO/PSE-modfied genosensor displayed highest sensitivity among graphene-modified and bare electrode, attributing to the large surface area-to-volume ratio and good electrocatalytic activity of the composite. The G/ZnO/PSE-modified genosensor displayed 5 times improvement in sensitivity as compared to the conventional gel electrophoresis, at a significance level of $P < 0.05$. These results demonstrated the feasibility of G/ZnO-enhanced genosensor to replace the conventional gel electrophoresis, as the genosensor is faster, more sensitive and requires lesser sample.

While the G/ZnO nanocomposite-enhanced sandwich sensing platform demonstrated good sensitivity and selectivity to the target of interest, further

effort was used to simplify the biosensing platform for the detection of single stranded DNA/RNA. Subsequently, the final work reports for the first time, the detection of Coconut Cadang-Cadang Viroid Disease (CCCVd) single stranded viral RNA (ssRNA) using single stranded DNA (ssDNA) as probe. The hybridisation event between ssDNA probe and ssRNA target was studied using electrochemical impedance spectroscopy (EIS). The G/ZnO-modified genosensing platform demonstrated wide linear detection range from 1×10^{-11} M to 1×10^{-6} M with a good detection limit of 4.3×10^{-12} M. Moreover, the G/ZnO-modified genosensor is also highly specific in discriminating the specific target from non-target and mismatched ssRNA sequences. Although the ssDNA probe used in this work is targeted towards CCCVd, the ssDNA probe on the G/ZnO nanocomposite-modified genosensing platform could be changed according to the sequence of interest, demonstrating the versatility of this sensing platform. In addition, the developed platform can be used as a model to develop effective biosensor platform for the early detection of other diseases by modifying the recognition layer with other antigen probes such as enzymes and antibodies. In short, the developed G/ZnO nanocomposite-based biosensing platform holds great potential for the detection of various target analytes in a wide range of applications in the near future.

7.2   Future Direction

The vision of this research was to produce versatile, highly sensitive and selective sensing platform based on G/ZnO nanocomposite synthesised. The work achieved in this report has built a foundation for future work to be based

upon. There are several issues and challenges that should be addressed based on the outcomes of the work in this thesis.

The biosensing work carried out in this research was based on commercialised screen printed carbon electrode (SPCE) while the modification with G/ZnO nanocomposite was performed by drop casting the G/ZnO dispersion onto the SPCE working electrode. The future work could be directed towards printing of electrode using G/ZnO nanocomposite-based ink, eliminating the modification step.

This study has demonstrated that the as-synthesised G/ZnO has very promising biosensing potential. The G/ZnO-modified electrode detected the ssRNA target synthesised based on the same sequence of CCCVd viral RNA. Thus, further work can focus on exploring real application, which is the detection of real sample. The CCCVd ssRNA can be extracted from infected oil palm leaves and apply to the G/ZnO-modified sensing platform. Also, the ideal medical biosensor is an implantable device which can detect the target molecule *in vivo*. Therefore, much consideration should be put on the toxicity and biocompatibility on the electrode material and design of the biosensor. Stringent toxicological assessment should be performed on G/ZnO to investigate its biocompatibility.

This study has developed a versatile genosensing platform based on G/ZnO nanocomposite. Therefore, future work can explore the detection of other diseases using the G/ZnO-modified genosensing platform by modifying the probe sequence used. In addition, one of the ultimate aim for biosensor

research is multianalyte detection. This work demonstrated the good H_2O_2 sensing capability of G/ZnO nanocomposite-modified biosensor, further exploration into detection of multianalyte simultaneously is worth looking into. In order to further develop the G/ZnO-modified biosensing platform, incorporation of biosensor with a microfluidic system can enable continuous detection of target molecule.

APPENDIX 1

Calculation of limit of detection (LOD) of developed sensor

The limit of detection is the lowest concentration at which the analyte can not be reliably detected but at which some predefined goals for bias and imprecision are met. The LOD could be calculated using this equation:

$$\text{LOD} = \frac{3\sigma}{S}$$

where σ is the standard deviation of the blank current response and S is the slope of the calibration curve.

Taking the developed sensor in Chapter 4 as an example,

the LOD of the developed sensor $= \frac{3 \; x \; (0.0304)}{0.0548}$

$$= 1.663 \text{ x } 10^{-9} \text{ M}$$

APPENDIX 2

Cyclic voltammetry (CV)

Electrochemistry can be defined as the study of phenomena resulting from the interrelation between electrical and chemical reactions. In general, it is the study of chemical reactions caused by electric current, or the study of current produced as a result of chemical reactions [251]. Cyclic voltammetry (CV) is a popular electrochemical method that is widely used to characterise an electrochemical system. CV is also the most versatile electroanalytical tool employed for the analysis of pharmaceuticals and biologically active compounds as it provides a wealth of information regarding the redox reactions, reversibility of the processes, interfacial phenomena at the electrode surface and bulk properties of materials in or on electrodes [252].

In CV experiment, the potential is cycled between two values (measured in volts) at a fixed rate and the current is recorded. The voltage begins at an initial potential (V_2), scanning continues to a predetermined switching potential (V_1), then reverses direction and sweep back to the initial value, thus the term cyclic voltammetry [252]. Therefore, the potential waveform input to the electrochemical cell is triangular or cyclic as shown in Figure A2.1.

A typical three-electrode cell consisting of a working electrode (WE), a reference electrode (RE) and an auxiliary electrode (AE) (also known as counter electrode, CE) is suitable for studying the electrochemistry of materials. The

voltage of the electrochemical cell is measured between the reference electrode and working electrode, while the current is measured between the counter electrode and working electrode [19]. The chemical reactions occur at the working electrode are investigated and the current that changes at this electrode is known as the *Faradaic* current [253]. In general, the potential of RE is kept at constant, whilst the potential of WE is varied in respect to RE. The standard REs that are used in electrochemical cell are Saturated Calomel Electrode (SCE) or Silver/Silver Chloride Electrode (Ag/AgCl). The function of CE is to maintain the current by providing electrons in the opposite direction as compared to the RE. As an example, if reduction occurs at RE, CE will provide electrons in reverse direction and thus oxidation will occur, thus maintaining the electron balance in the system [253].
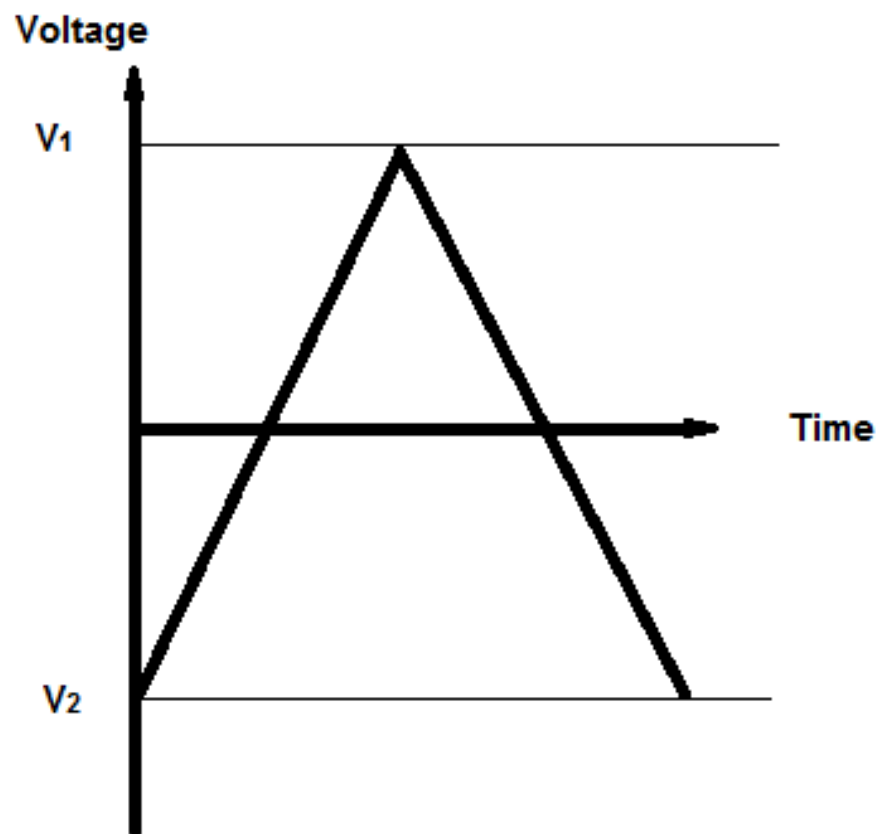
Figure A2.1: Schematic representation of a CV waveform. In CV experiment, the voltage is swept back at forth between two fixed values, V_1 and V_2 at a constant scan rate [254].

The CV measurements are plotted as a function of current versus potential, also known as a cyclic voltammogram as illustrated in Figure A2.2. The CV is typically characterised by several important features such as the cathodic (E_p') and anodic (E_p) peak potentials, the corresponding cathodic (i') and anodic (i) peak currents and the half peak potential ($E_{p1/2}$) [255]. Multiple peaks in the CV might be observed due to multi-step parallel or consecutive mechanisms, or presence of several different redox species. Therefore, CV could provide researchers with information on the electrochemical cell through the analysis on the characteristics of CV.
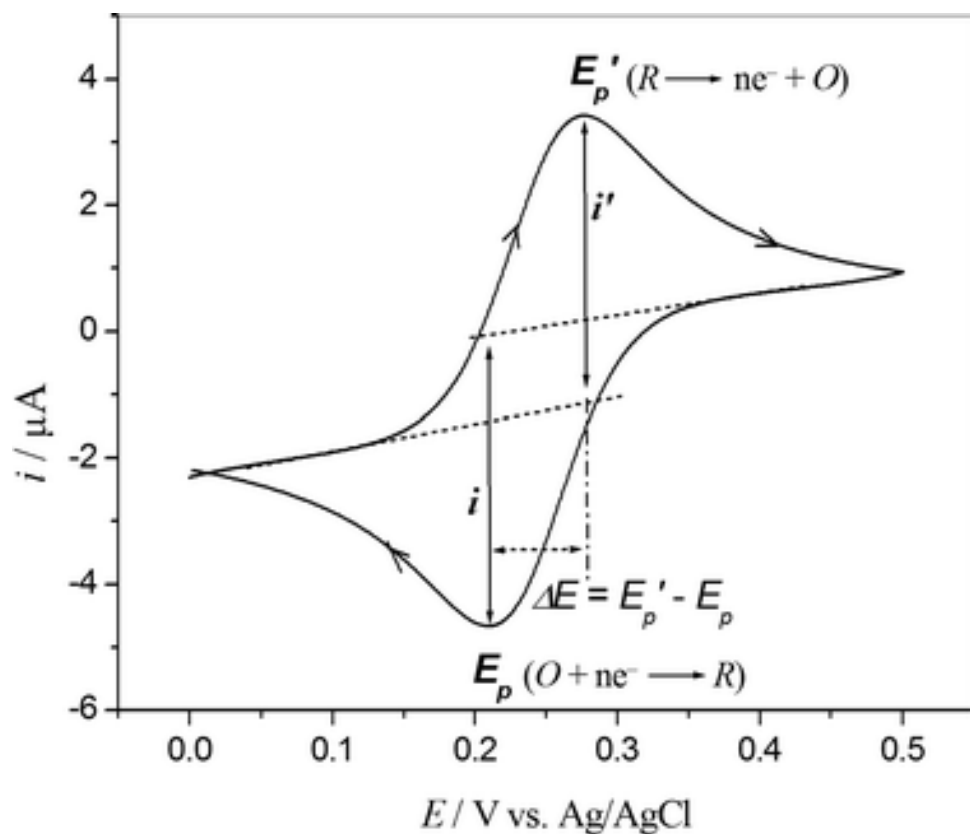
Figure A2.2: A typical cyclic voltammogram of a fully reversible redox couple showing the key features, peak potentials, peak currents and potential separation [256].

Basic Theory

In CV, the Randles-Sevcik equation (Equation A2.1) describes the effect of scan rate on the peak current (i_p) [218].

$$i_p = (2.69 \text{ x } 10^5) \, n^{3/2} \, A \, D^{1/2} \, C \, v^{1/2} \hspace{2cm} \text{Equation A2.1}$$

At 25 °C, i_p is the peak current (A), n is the electron stoichiometry, A is the electrode area (cm^2), D is the diffusion coefficient (cm^2/s), C is the concentration (mol/cm^3) and v is the scan rate (V/s).

This equation is particularly important in the study of electrode mechanism as it can be employed for the testing of reversibility of an electrode reaction. It was deduced that by studying the relationship between the peak current and the square root of scan rate (speed of the voltage sweep), the nature of the redox process can be understand [257].

APPENDIX 3

Amperometry

The term "amperometry" describes an electroanalytical technique in which the current resulting from oxidation or reduction reactions at a fixed potential is recorded over a period of time [258]. The current can be used to quantify the electrochemical species involved in the redox reaction. The commonly used amperometric detectors are three-electrode setup type as shown in Figure A3.1. The fixed potential is set by working electrode relative to the reference electrode, and the flowing current is measured as signal. The current is amplified and recorded as a function of the time flow, resulting in the chromatogram displaying concentration-time profile [259].
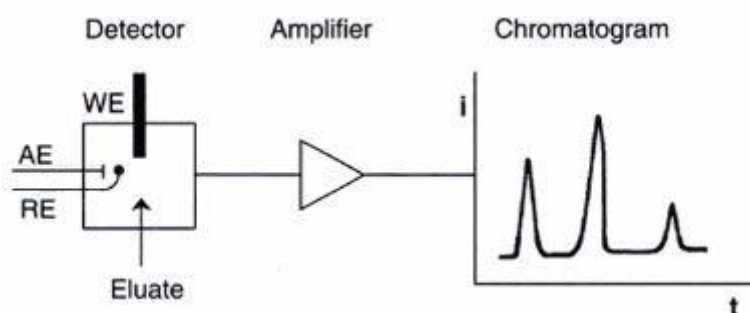
Figure A3.1: Outline of amperometric detection, detailing three electrodes setup with the resulting chromatogram. WE – working electrode; AE – auxiliary electrode (also known as counter electrode); RE – reference electrode [259].

Intermittent Pulse Amperometry (IPA)

Intermittent pulse amperometry (IPA) is an electrochemical technique developed for simultaneous and independent measurements of DNA and RNA in multitarget samples using low- or high-density sensor arrays. It involves a series of milliseconds pulses of the same potential applied to the working electrode, separated by longer periods when the electrode is disconnected from the potentiostat circuit [260]. The potential waveform of IPA is shown in Figure A3.2A and upon comparing with conventional direct current amperometry (DCA), a five to ten fold amplification of current signal measured during the last 100 microseconds is observed (Figure A3.2B). This is due to the concentration depletion created by continuously applied potential in DCA [261].
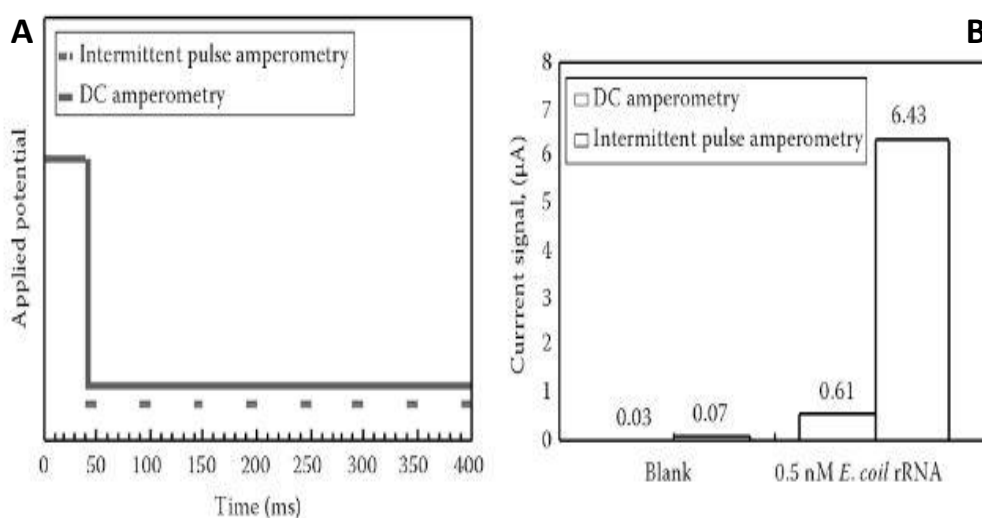
Figure A3.2: (A) Typical potential waveforms used in direct current amperometry and intermittent pulse amperometry, (B) Comparison of target detection sensitivity using DC amperometry and IPA [261].

APPENDIX 4

Electrochemical Impedance Spectroscopy (EIS)

Electrochemical impedance spectroscopy (EIS) is a powerful analytical tool that can be used to study the complex electrical resistance of a system and is sensitive to changes in surface phenomena or electrical properties of materials. In principle, impedance is similar to resistance, which is the opposition force to electrical current in a circuit. However, impedance differs from resistance because it does not obey Ohm's law, is observed in alternating current (AC) with phase shift and frequency dependent [262]. Therefore, EIS is performed by applying a small amplitude sinusoidal voltage signal to the electrochemical cell and the resulting current response is detected [263].

EIS has numerous applications, for example it can be used in the study of interfacial processes, geometric effects or applications in power sources [264]. In terms of biosensing, EIS can be employed to analyse biomolecules, such as enzymes, lipids and membranes, as well as the adsorption behaviour of antigens and DNA at the surface of modified electrode [265]. The binding efficiency of antibodies onto electrode surface will affect the impedance of electrode, which will be reflected in the increment of charge transfer resistance in EIS analysis. In fact, almost any process that involves change in conductivity of a system can be recognised by EIS, hence a multitude of properties can be elucidated using this technique.

Basic Theory

The EIS technique is developed based on the complex mathematical transforms to yield real values of impedance in temporal space, first described in the late 19th century by Oliver Heaviside [262]. Critically, the "operational impedance" was defined as the "complex ratio of the voltage and current in an alternating current (AC) circuit", which is denoted today as Equation A4.1.

$$Z(j\omega) = \frac{V(j\omega)}{I(j\omega)} \qquad \text{Equation A4.1}$$

Where Z is the impedance, V is the voltage, I is the current, j is the imaginary component and ω is the frequency. As $j = \sqrt{-1}$ and the excitation frequencies are expressed as ω (rad.s^{-1}) and f (Hz), the impedance can be presented in terms of the real Z_{re} (ω), and imaginary Z_{im} (ω) components, as shown in Equation A4.2.

$$Z(j\omega) = Z_{re}(\omega) + jZ_{im}(\omega) \text{ whereby } \omega = 2\pi f \qquad \text{Equation A4.2}$$

Ultimately, the complex impedance is determined from the real Z_{re} (ω), and imaginary Z_{im} (ω) components, which are originated from the resistance and capacitance of the electrochemical system, and commonly plotted in the Nyquist plot [263].

EIS Nyquist Plot

In EIS experiment, voltage is applied at a set frequency and the resulting current will flow through the electrochemical cell, which is then recorded by the potentiostat and converted by software via Equation A4.2 into an

impedance value with a real and imaginary component. The real and imaginary components of the overall impedance value are deduced by repeating the process across a frequency range. The in-phase current response determines the real (related to resistance) component while the out-of-phase current response determines the imaginary (related to capacitance) component of the impedance [266]. As a result, the data is presented by plotting the real and imaginary impedance components against one another in Nyquist plot [265]. The Nyquist plot typically consists of a semi-circular portion at high frequencies, corresponding to the electron transfer limited process and a linear portion at low frequencies, resulting from the diffusion limiting step as illustrated in Figure A4.1.
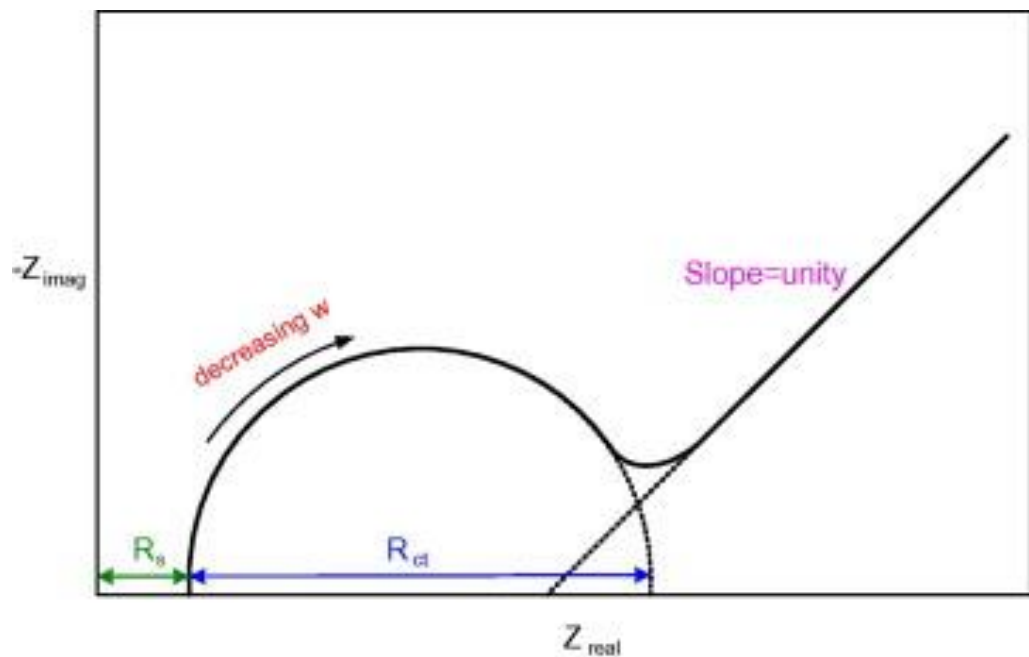
Figure A4.1: A typical Nyquist plot displaying a semi-circular portion and a linear portion with various impedance parameters such as the charge transfer resistance, R_{ct}, the solution resistance, R_s and frequency, w [266].

Equivalent Circuit Modelling

Equivalent circuit modelling in correspond to the experimental impedance spectra is performed to extract information on the electrochemical reactions occurring at the electrode/electrolyte interface [263]. Basically, the impedance data of a simple electrochemical reaction is fitted to an equivalent circuit consisting of resistors and capacitors arranged in a circuit shown in **Error! Reference source not found.** A4.2, which is being termed as the Randles equivalent circuit. The Randles circuit consists of four elements which are usually used to describe the impedance behaviour: ohmic resistance of the electrolyte solution (R_s), the Warburg impedance (Z_w) resulting from the diffusion of ions from the bulk electrolyte to the electrode interface, the double layer capacitance (C_d), and electron transfer resistance (R_{ct}) that exists if a redox probe is present in the electrolyte solution [263]. Generally, R_s and Z_w represent the bulk properties of the electrolyte, whereas C_d and R_{ct} reflect the electrode properties, specifically the insulating layer at the electrode/electrolyte interface [267]. A constant phase element (CPE) could be used to replace the capacitor in the presence of chemical inhomogenities or surface roughness of the electrode [265]. As such, depending on the focus of study, researchers could analyse the impedance spectra based on the values computed from respective elements in the equivalent circuit.
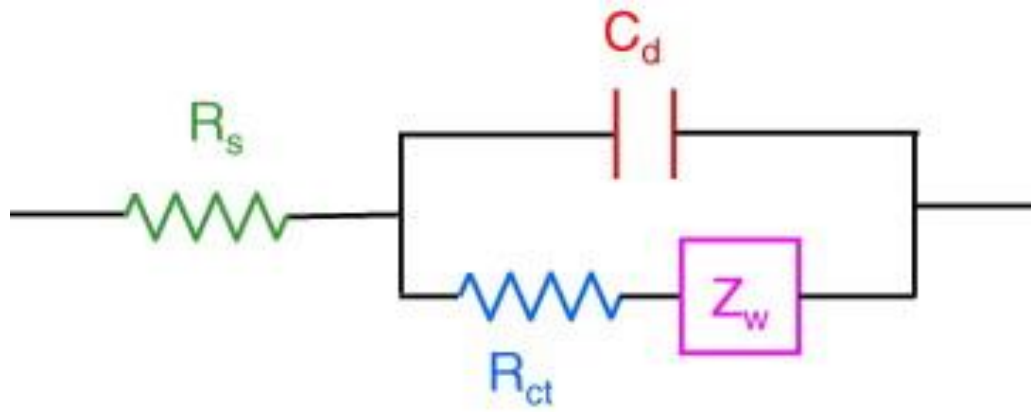
Figure A4.2: Randles equivalent circuit consisting of the solution resistance, R_s in series with charge transfer resistance, R_{ct} and the Warburg impedance, Z_w placed in parallel with the double layer capacitance, C_d [266].

APPENDIX 5

Differential Pulse Voltammetry (DPV)

Differential pulse voltammetry (DPV) is an electrochemical technique useful in measuring trace levels of organic and inorganic species [268]. It consists of a series of measurement pulses applied through a working electrode. Ini DPV, pulses are superimposed on a linear potential ramp within the user-defined range (Figure A5.1). The pulse duration is typically set at 50 milliseconds while the pulse repetition period is in the range of 0.5 to 5 seconds.
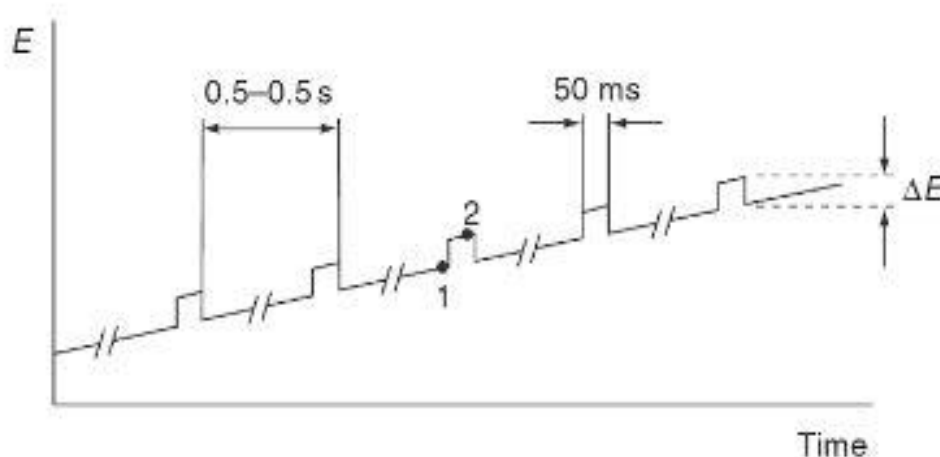
Figure A5.1: Schematic waveform of pulses superimposed on a linear potential ramp in differential pulse voltammetry [268].

The current is measured twice as shown in **Error! Reference source not found.** A5.2, once just before the pulse application and once at the end of the pulse. The signal current is obtained by the subtraction between the first and second current. Therefore, a differential pulse voltammogram is a plot of

differential current against the applied potential, where the peak height is directly proportional to the concentration of the corresponding analytes.
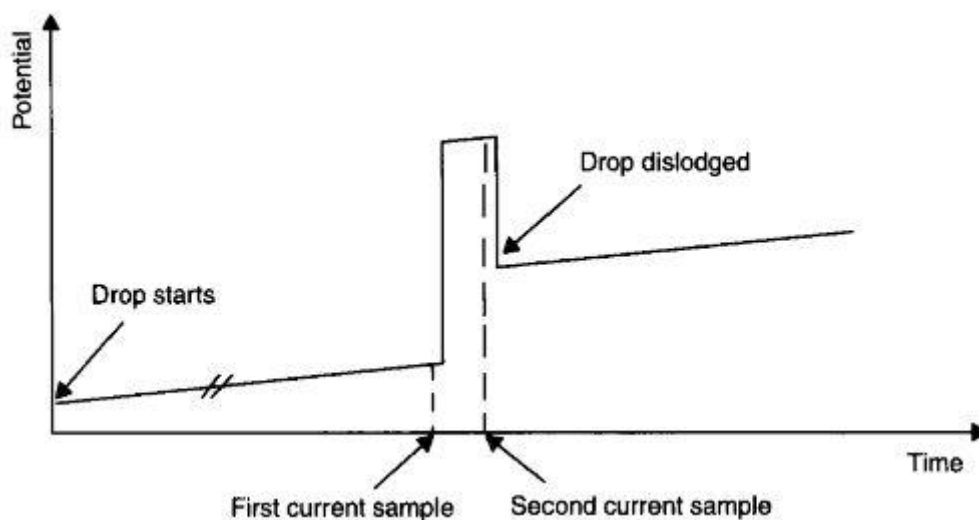
Figure A5.2: Diagram showing the time point of current being sampled, once just before the pulse and once before the drop is dislodged at the end of the pulse [269].

The use of pulses and differential measurement greatly reduces the contribution of the non-Faradaic processes, principally capacitive, avoiding problems with interference from capacitive currents that originate as consequence of the electrode/media bilayer interface [270]. In addition, DPV has the ability to detect the presence of several electroactive species simultaneously by examining a range of potentials between the limits of the potential ramp.

APPENDIX 6

Scanning Electron Microscopy (SEM)

In the rapid advancement of technology, researchers today are often required to observe and correctly explain phenomena happening on a micrometer or even submicrometer scale. The scanning electron microscopy (SEM) is a powerful surface microscopy technique which permits the characterisation of heterogenous materials [271]. Comparing with light microscope, the SEM deals with electrons of shorter wavelength, thereby enabling greater magnification, along with increase in resolution capability, allowing the researchers to visualise small organelles and more [272].

SEM is a versatile electron-optical instrument for the examination and investigation of specimens as it can yield information on surface topography, crystalline structure, chemical composition, magnetic and electrical characteristics of the specimens [273]. The basic components of the SEM are the lens system, electron gun, electron detection system, visual and recording cathode ray tubes (CRTs) and the electronics associated with them as displayed in Figure A6.1.
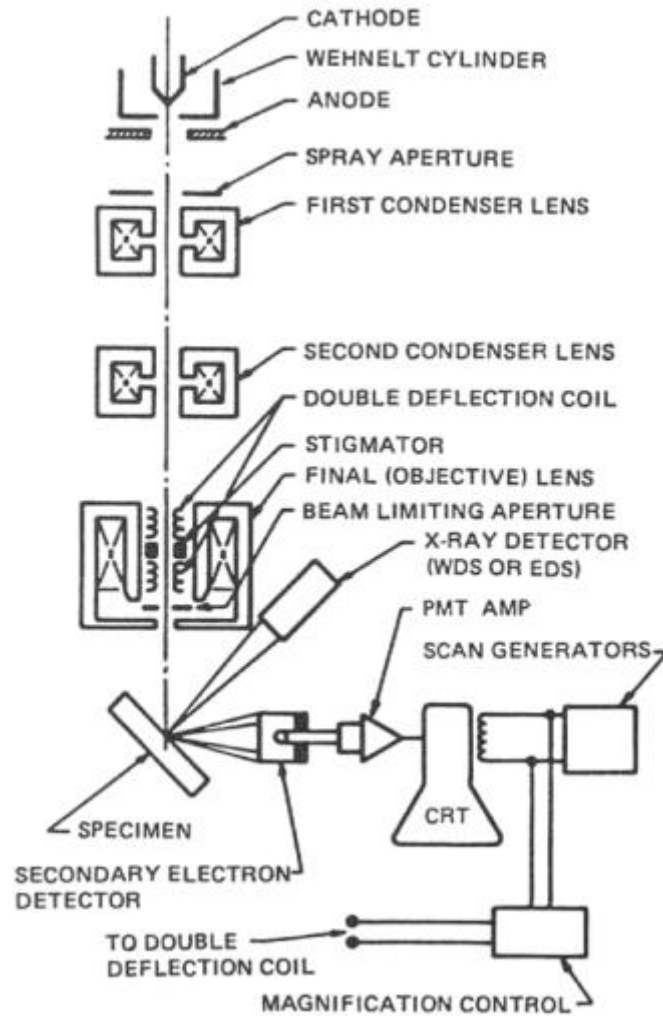
Figure A6.1: Schematic diagram of a scanning electron microscope (SEM) [274].

In SEM, an electron beam with energy typically in the range of 2 to 40 keV is ejected from the electron gun to generate a variety of signals at the surface of the specimen. The accelerated electron beam is normally generated by tungsten hairpin filament, lanthanum hexaboride filaments or field emission guns [273]. The electron beam is demagnified into fine probe upon passing through several condenser lens, which is then scanned across the specimen surface. The interaction of the electron beam with the specimen produces a

number of signals, such as back-scattered electrons, secondary electrons, Auger electrons and X-ray fluorescence as illustrated in Figure A6.2. The generated signals are collected by electron detectors placed at various positions.
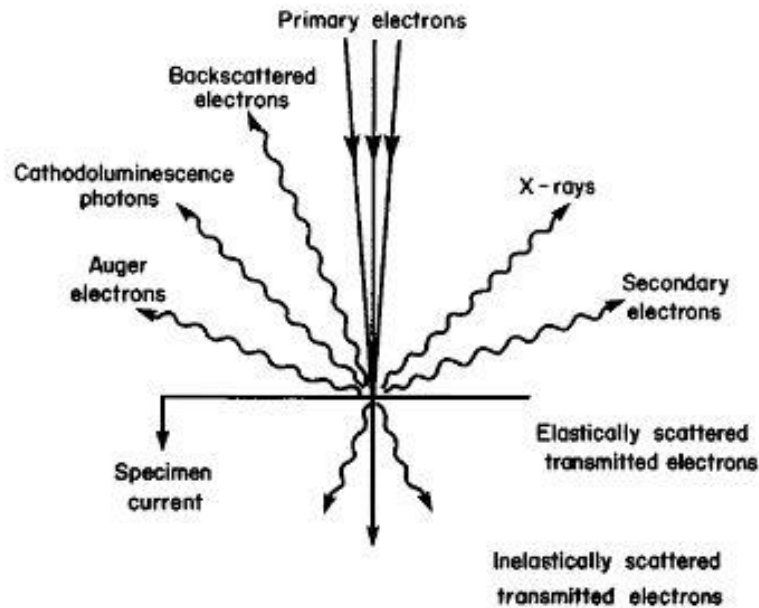
Figure A6.2: Signals resulting from interaction between electron beam and specimen [275].

Upon in contact with the specimen, some electrons are elastically scattered without significant loss of energy, known as back-scattered electrons, while some electrons encounter inelastic collision, causing the specimen atom to ionise, termed as secondary electrons (SEs). Generally, backscattered electrons (BSEs) are defined to be electrons with broad energy range of 50 eV up to the incident electron beam energy. On the other hand, secondary electrons consist of lower energy, mostly in the energy range of 0.5 to 5 eV [276].

Most SEM images are collected with the Everhart-Thornley (ET) detector as shown in Figure A6.3. The ET detector collects mainly SEs and BSEs, which are the most common signals in the formation of SEM image [277]. The ET detector consists of a collector grid, a scintillator and a photomultiplier. SEs are attracted toward the scintillator by a 200 V potential on the collector grid. BSEs could also be collected but less efficiently due to their high energy. A 10 kV bias is applied onto the scintillator to accelerate SEs enough to cause photon emission in the light pipe. The photons will then be transferred to the photomultiplier, which are being converted into electrical signals.
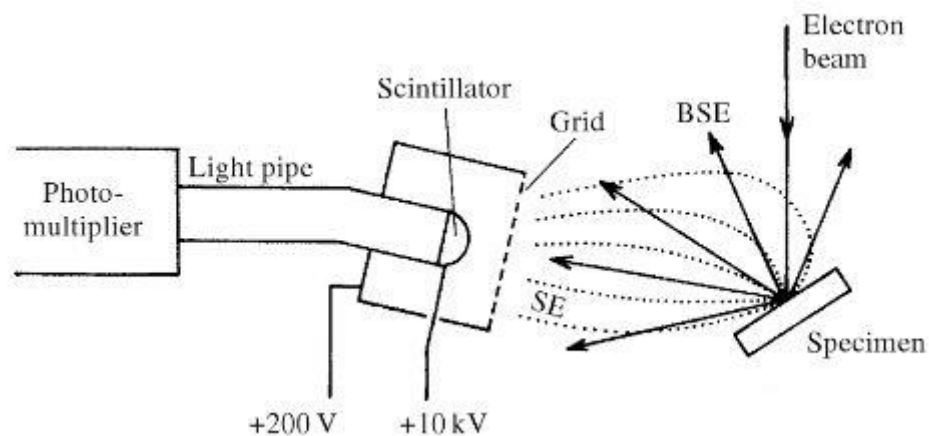
Figure A6.3: Schematic diagram showing an Everhart-Thornley (ET) detector typically used in SEM [277].

APPENDIX 7

Energy Dispersive X-Ray Spectroscopy (EDS)

Energy dispersive X-ray spectroscopy (EDS) is a technique used to analyse the chemical composition of materials based on the characteristic X-ray pattern emitted by the atoms of elements in the sample [278]. EDS is one of the most common used X-ray microanalysis due to its cost effectiveness and rapid detection of elements present in the specimen [279].

In EDS, a solid state X-ray detector, usually consisting of a Si(Li) crystal maintained at cryogenic temperatures and pulse counting electronics are used. The detector converts the energy of an incoming X-ray photon into charge pulse of proportional amplitude, which is later processed into the appropriate channel of a multi-channel analyser (MCA) as shown in Figure A7.1, resulting in a histogram of X-ray energy versus intensity [280]. The X-ray energies are unique for each element, thereby facilitating atom identification, with the relative peak intensities can be related to relative atomic concentrations through comparison.
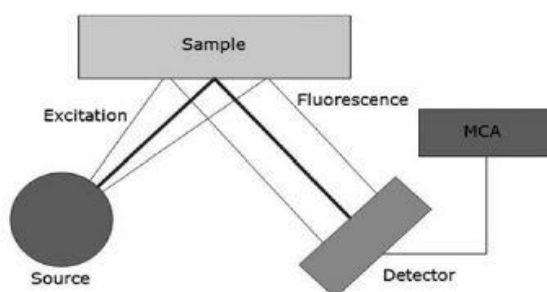
Figure A7.1: Schematic diagram of an energy dispersive X-ray spectrometer [281].

The EDS spectrum is generally displayed in digitised form with the x-axis representing the X-ray energy while the y-axis indicating the number of counts per channel (Figure A7.2). All elements with an atomic number higher than beryllium, Z = 4, in principle detectable as long as present in sufficient quantity [280]. The main advantage of EDS is the ability to simultaneously detecting elements with a cost effective small detector placed inside the electron beam system, adding an elemental analytical capability to the imaging system.
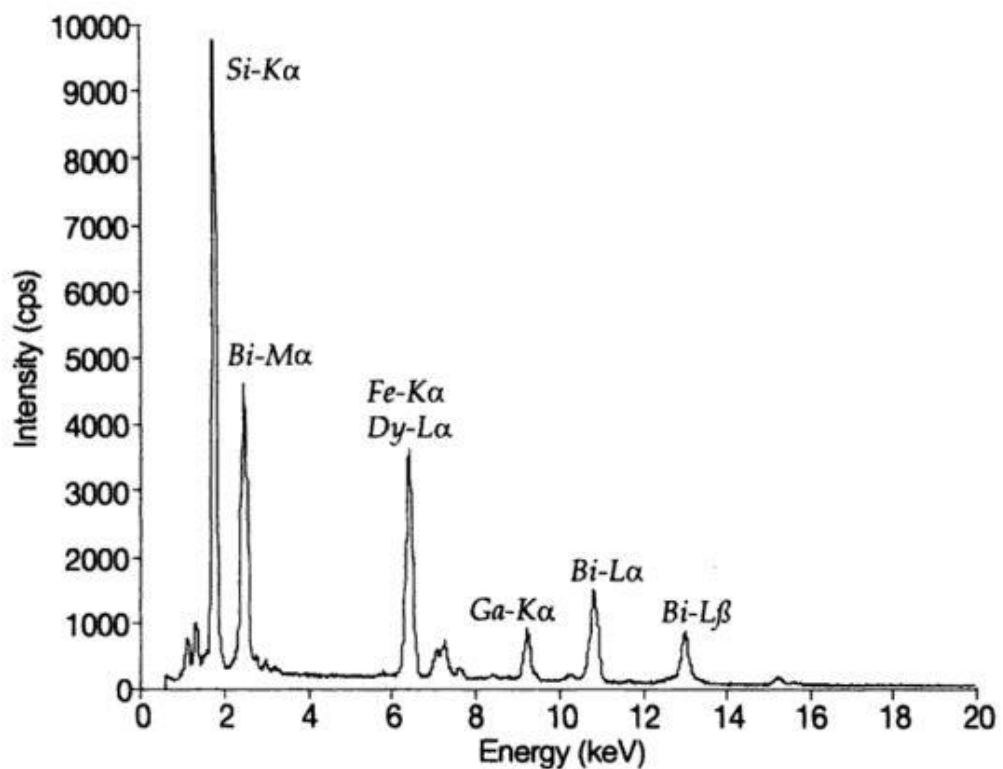
Figure A7.2: Standard EDS spectrum with x-axis representing the energy scale and y-axis indicating the number of photons per energy interval [282].

APPENDIX 8

Transmission Electron Microscopy (TEM)

Transmission electron microscope (TEM) is a very powerful tool for microstructural characterisation of materials. It uses a particle beam of high energy electrons (up to 400 kV accelerating voltage) to visualise specimens [283]. The electron beam behaves like a wavefront with wavelength way shorter than lightwaves, therefore generating a highly magnified image.

The operating principle of TEM is similar to the light microscope with the difference of usage of electrons instead of light. The TEM has three essential systems, namely the condenser system, image producing system and image recording system, which are displayed in Figure A8.1. In TEM, the electron gun emits electrons that travel through the vacuum tube inside the microscope. Upon entering the condenser system containing electromagnetic lenses, the electron beam is focused into a small, thin and coherent beam. This beam is controlled by the condenser aperture, in which the high angle electrons are eliminated to enhance the contrast. The beam then passes through the specimen and parts of it are transmitted depending on the thickness of the specimen [283]. The transmitted electrons enter the image producing system, where they are focused by the objective lens into an image on the fluorescent screen at the bottom of the microscope. The intermediate and projector lenses will produce either an image or a diffraction pattern on the final viewing medium, depending on the mode of operation.
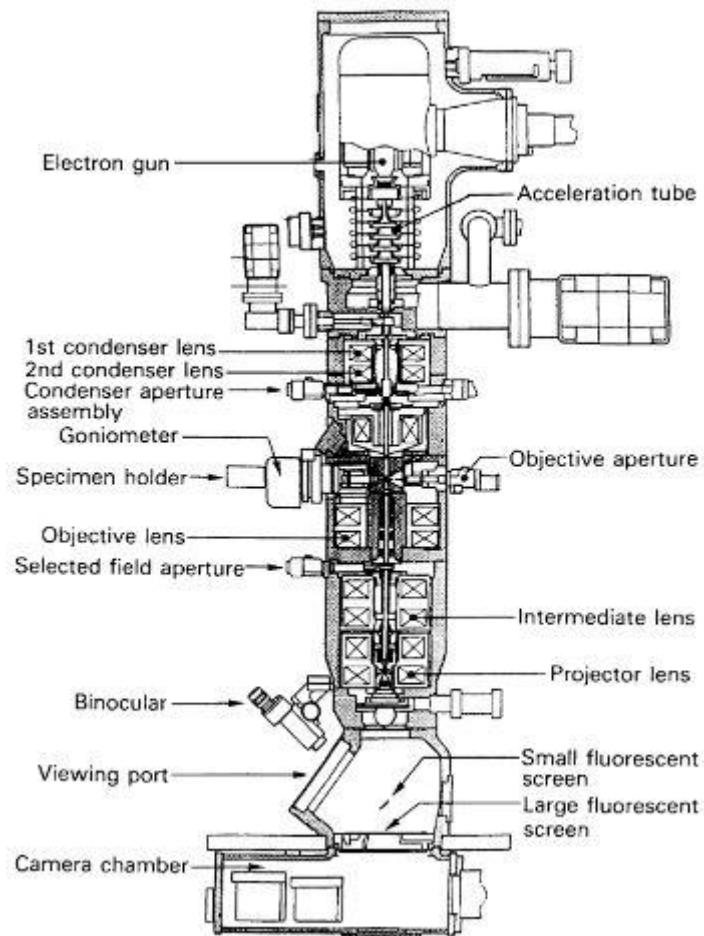
Figure A8.1: General layout of TEM describing the path of electron beam in it [284].

Generally, SEM and TEM are both employed in the characterisation of materials. The TEM projects electrons through specimen, which is generally thin enough for the transmission of electrons with minimum energy loss to produce a two-dimensional (2D) image. The brightness of the image formed is proportional to the number of electrons that are transmitted through the specimen. In comparison, SEM generates image through secondary and backscattered electrons, resulting in three-dimensional (3D) image. The basic difference in the working principle of SEM and TEM is shown in Figure A8.2A

and the resulting respective images are displayed in Figure A8.2B. It was observed in Figure A8.2B that SEM focuses on the surface features of the specimen while TEM reveals the internal details of the specimen [272].
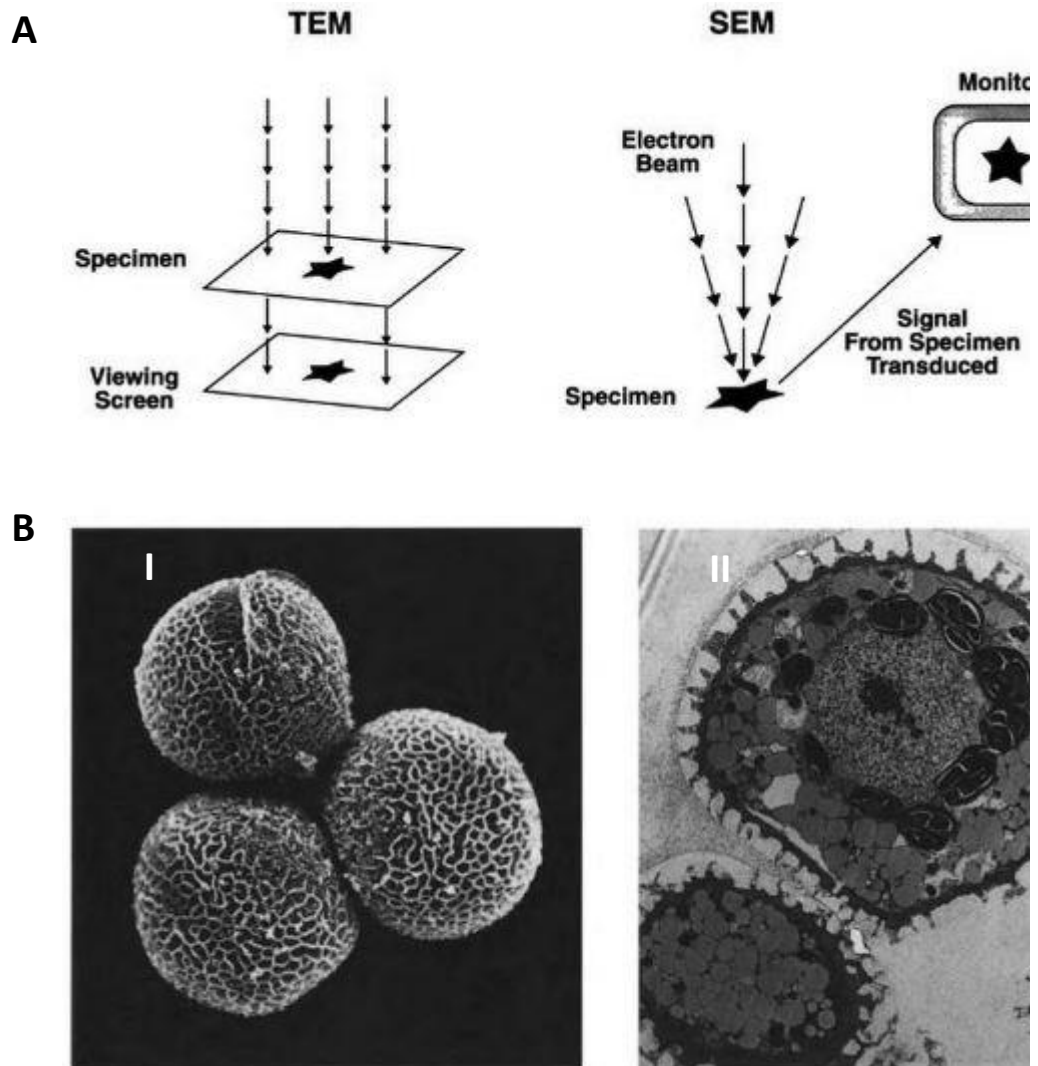
Figure A8.2: (A) Schematic diagram showing different working principles of TEM and SEM, where the electrons are transmitted in TEM and reflected in SEM. (B) Spores of the liverwort, *Pallavicinia*, are displayed as 3D image in (I) SEM and 2D image in (II) TEM [272].

APPENDIX 9

X-Ray Diffractometry (XRD)

X-ray diffractometry (XRD) is a powerful analytical technique employed for the characterisation of materials. It is a common technique to study the crystal structure and atomic spacing of material as it can provide structural information such as phases, crystal orientations, size, defects and many more [285]. XRD is a noncontact and non-destructive method, making it suitable for *in situ* studies. It can also be used determine the thickness and atomic arrangements of materials [286].

The working principle of XRD is based on constructive interference of monochromatic X-rays and a crystalline sample. In XRD, X-rays are generated by a cathode ray tube, which is filtered by foils or crystal monochrometers to produce monochromatic radiation needed for diffraction. These X-rays are then collimated to concentrate and direct towards the sample. The intensity of the reflected X-rays is recorded by the rotating sample and detector (Figure A9.1).
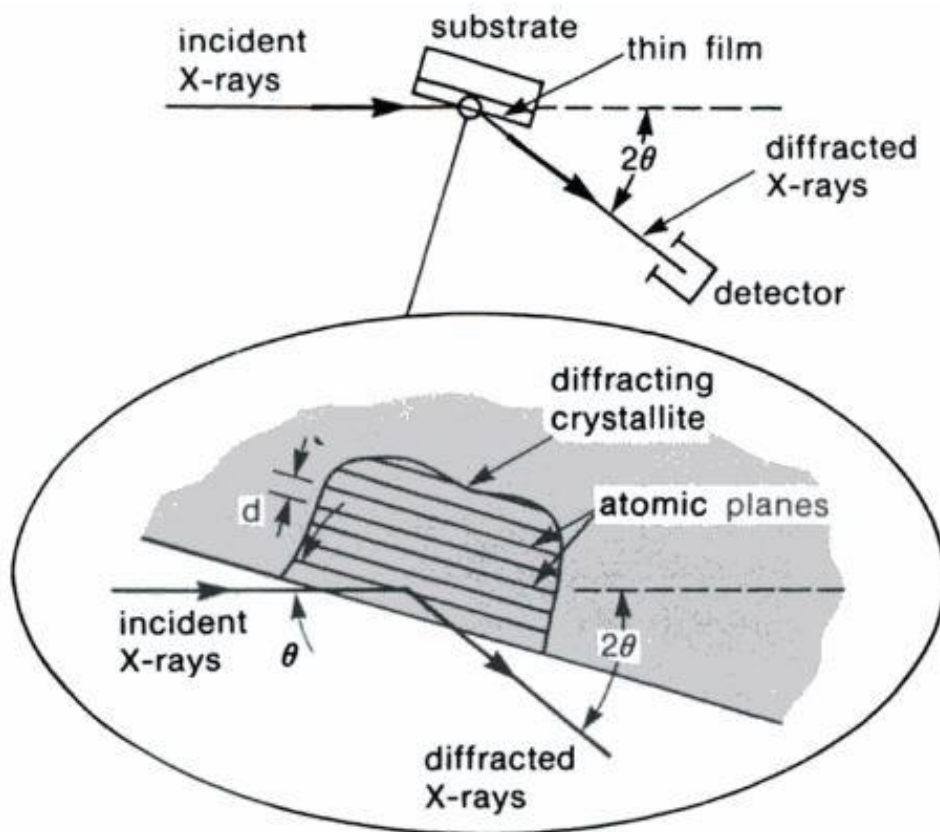
Figure A9.1: Schematic diagram of a X-ray diffractometer system displaying diffracted X-rays from substrate are recorded by detector at an angle of 2θ [286].

Bragg's law (Equation A9.1) is important to understand the concept of XRD as it relates the wavelength of electromagnetic radiation to the diffraction angle and the lattice spacing in a crystalline sample [285].

$$n\lambda = 2d \sin\theta$$
<div align="right">Equation A9.1</div>

where n is the order of reflection, λ is the wavelength of the X-rays, d is the characteristic interplanar spacing and θ is the diffraction angle.

In XRD, the sample is rotated to be at an angle θ with the collimated X-ray beam while the X-ray detector is mounted onto an arm to collect the

diffracted X-rays and rotates at an angle of 2θ [285]. These diffracted X-rays are recorded, processed and converted to a count rate by the X-ray detector. For typical powdered material, the data is collected at 2θ angles from 5° to 70°, where all possible diffraction directions of the lattice should be attained. The obtained diffraction peaks will be converted into d-spacings, and by comparing the d-spacings with the standard reference patterns, inorganic crystal structure database (ICSD), identification of the sample is achieved.

APPENDIX 10

Raman Spectroscopy

Raman spectroscopy is a branch of vibrational spectroscopy using inelastically scattered light to interrogate and identify the vibrational (phonon) states of molecules. It is a powerful tool that is capable of giving the precise vibrational energies of molecules, providing the unique fingerprint for chemical identification.

The working principle of Raman spectroscopy is based on measuring the frequency shift of inelastic scattered light from the sample when the photon from incident light strikes the molecule and produce a scattered photon. In Raman spectroscopy, sample is illuminated with a monochromatic laser beam. The monochromatic radiation interacts with the molecules of sample and two types of scattered light occur (Figure A10.1**Error! Reference source not found.**). In the case of scattered light at the same frequency, no energy change is being observed, and this is known as elastic or Rayleigh scattering. Only a small fraction of the scattered radiation will experience frequency change from the incident radiation, which is referred as inelastic or Raman scattering. In order to further distinguish the Raman scattering, the scattered light with higher frequency and lower energy is known as Stokes lines, while the scattered light with lower frequency and higher energy is termed as Anti-Stokes lines [287].
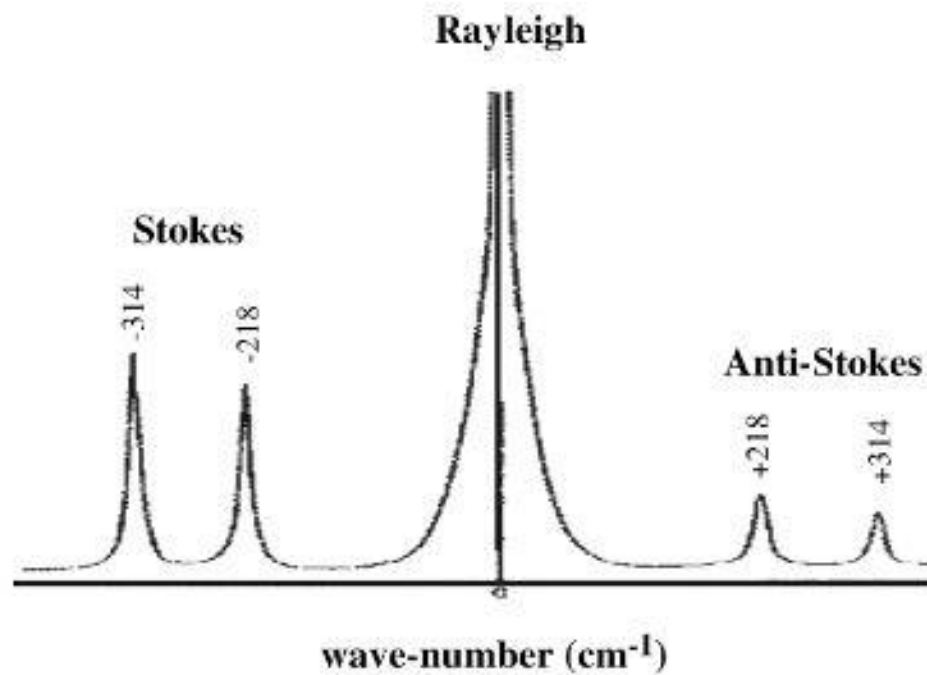
Figure A10.1: Illustration of a generic spectrum showing Rayleigh and

Raman bands [287].

The energy changes between the incident and scattered light is related to the vibrational energy spacing in the ground electronic state of the molecule. The shift in wavelength of the scattered light depends on the chemical composition of the sample, thereby enabling fingerprinting. A Raman spectrum is presented as an intensity versus wavelength shift. The intensity of Raman scattering is proportional to the magnitude of the change in the molecular polarisation [288].

References

1.   Staryszak, J., et al., *Usefulness of Ultrasound Examinations in the Diagnostics of Necrotizing Enterocolitis.* Polish Journal of Radiology, 2015. **80**: p. 1-9.

2.   Thevenot, D.R., et al., *Electrochemical Biosensors: Recommended Definitions and Classification.* Pure and Applied Chemistry, 1999. **71**(12): p. 2333–2348.

3.   Setford, S.J. and J.D. Newman, *Enzyme Biosensors*, in *Microbial Enzymes and Biotransformations*, J.L. Barredo, Editor. 2005, Humana Press Inc.: Totowa. p. 29-60.

4.   Holzinger, M., A.L. Goff, and S. Cosnier, *Nanomaterials for biosensing applications: a review.* Frontiers in Chemistry, 2014. **2**: p. 1-10.

5.   Novoselov, K.S., et al., *Electric field effect in atomically thin carbon films.* Science, 2004. **306**(5696): p. 666-669.

6.   Yang, W., et al., *Graphene in Supercapacitor Applications.* Current Opinion in Colloid & Interface Science, 2015. **20**(5–6): p. 416-428.

7.   Song, Y., et al., *Recent advances in electrochemical biosensors based on graphene two-dimensional nanomaterials.* Biosensors and Bioelectronics, 2016. **76**: p. 195-212.

8.   Machado, B.F. and P. Serp, *Graphene-based materials for catalysis.* Catalysis Science & Technology, 2012. **2**(1): p. 54-75.

9.   Wang, H. and X. Yuan, *Graphene-Based Devices for Hydrogen Storage*, in *Graphene-based Energy Devices*. 2015, Wiley-VCH Verlag GmbH & Co. KGaA. p. 295-306.

10.   Dong, X., et al., *Hybrid structure of zinc oxide nanorods and three dimensional graphene foam for supercapacitor and electrochemical sensor applications.* RSC Advances, 2012. **2**(10): p. 4364-4369.

11.   Peng, Y., J. Ji, and D. Chen, *Ultrasound assisted synthesis of ZnO/reduced graphene oxide composites with enhanced photocatalytic activity and anti-photocorrosion.* Applied Surface Science, 2015. **356**: p. 762-768.

12.   Li, H., et al., *In situ sol-gel synthesis of ultrafine ZnO nanocrystals anchored on graphene as anode material for lithium-ion batteries.* Ceramics International, 2016. **42**(10): p. 12371-12377.

13.   Moussa, H., et al., *ZnO rods/reduced graphene oxide composites prepared via a solvothermal reaction for efficient sunlight-driven photocatalysis.* Applied Catalysis B: Environmental, 2016. **185**: p. 11-21.

14.   Guo, Y., et al., *One-pot synthesis of graphene/zinc oxide by microwave irradiation with enhanced supercapacitor performance.* RSC Advances, 2016. **6**(23): p. 19394-19403.

15.   Zhang, Z., et al., *One-pot electrodeposition synthesis of ZnO/graphene composite and its use as binder-free electrode for supercapacitor.* Ceramics International, 2014.

16.   Clark, L.C. and C. Lyons, *ELECTRODE SYSTEMS FOR CONTINUOUS MONITORING IN CARDIOVASCULAR SURGERY.* Annals of the New York Academy of Sciences, 1962. **102**(1): p. 29-45.

17.   Lowe, C.R., *Biosensors.* Trends in Biotechnology, 1984. **2**(3): p. 59-65.

18.   Turner, A.P.F., *Biosensors: sense and sensibility.* Chemical Society Reviews, 2013. **42**(8): p. 3184-3196.

19.   Grieshaber, D., et al., *Electrochemical Biosensors - Sensor Principles and Architectures.* Sensors, 2008. **8**(3): p. 1400-1458.

20.   Koyun, A., E. Ahlatcioglu, and Y.K. Ipek, *Biosensors and Their Principles*, in *A Roadmap of Biomedical Engineers and Milestones*, S. Kara, Editor. 2012, InTech: Croatia. p. 115-142.

21.   Damborský, P., J. Švitel, and J. Katrlík, *Optical biosensors.* Essays in Biochemistry, 2016. **60**(1): p. 91-100.

22.   Spink, C. and I. Wadso, *Calorimetry as an analytical tool in biochemistry and biology.* Meth. Biochem. Anal., 1976. **23**: p. 1 - 159.

23.   Ramanathan, K. and B. Danielsson, *Principles and applications of thermal biosensors.* Biosensors and Bioelectronics, 2001. **16**(6): p. 417-423.

24.   Shantilatha, P., S. Varma, and C.K. Mitra, *Designing a Simple Biosensor*, in *Advances in Biosensors: Perspectives in Biosensors*, B.D. Malhotra and A.P.F. Turner, Editors. 2003, Elsevier Science B.V.: Amsterdam. p. 1-36.

25.   Srivastava, S.K., C.J.M. van Rijn, and M.A. Jongsma, *Biosensor-based detection of tuberculosis.* RSC Advances, 2016. **6**(22): p. 17759-17771.

26.   Sadeghi, S.J., *Amperometric Biosensors*, in *Encyclopedia of Biophysics*, G.C.K. Roberts, Editor. 2013, Springer Berlin Heidelberg: Berlin, Heidelberg. p. 61-67.

27.   Korotkaya, E.V., *Biosensors: Design, Classification, and Applications in the Food Industry.* Foods and Raw Materials, 2014. **2**(2): p. 161-171.

28.   Malhotra, B.D. and V. Saxena, *Electrochemical Biosensors*, in *Advances in Biosensors: Perspectives in Biosensors*, B.D. Malhotra and A. Turner, Editors. 2003, Elsevier Science B.V.: Amsterdam. p. 63-100.

29.   Monošík, R., M. Streďanský, and E. Šturdík, *Biosensors - classification, characterization and new trends.* Acta Chimica Slovaca, 2012. **5**(1): p. 109–120.

30.   Pohanka, M. and P. Skládal, *Electrochemical Biosensors - Principles and Applications.* Journal of applied biomedicine, 2008. **6**: p. 57-64.

31.   Mehrvar, M. and M. Abdi, *Recent Developments, Characteristics, and Potential Applications of Electrochemical Biosensors.* Analytical Sciences, 2004. **20**: p. 1113-1126.

32.   Standardization, I.O.f., *Nanotechnologies-vocabulary-part 1: Core Terms*. 2010.

33.   Soldano, C., A. Mahmood, and E. Dujardin, *Production, properties and potential of graphene.* Carbon, 2010. **48**(8): p. 2127-2150.

34.   Yazid, S.N.A.M., et al., *A Review of Glucose Biosensors Based on Graphene/Metal Oxide Nanomaterials.* Analytical LEtters, 2014. **47**(11): p. 1821-1834.

35.   Sharma, P., et al., *Metal Oxide-Graphene Nanocomposites: Synthesis to Applications*, in *Handbook of Research on Nanoscience, Nanotechnology, and Advanced Materials*, M. Bououdina and J.P. Davim, Editors. 2014, IGI Global: Hershey. p. 196-225.

36.   Paek, S.-M., E. Yoo, and I. Honma, *Enhanced Cyclic Performance and Lithium Storage Capacity of SnO2/Graphene Nanoporous Electrodes with Three-Dimensionally Delaminated Flexible Structure.* Nano Letters, 2009. **9**(1): p. 72-75.

37.   Yao, Y., et al., *Magnetic CoFe2O4–Graphene Hybrids: Facile Synthesis, Characterization, and Catalytic Properties.* Industrial & Engineering Chemistry Research, 2012. **51**(17): p. 6044-6051.

38.   Salamon, J., et al., *One-pot synthesis of magnetite nanorods/graphene composites and its catalytic activity toward electrochemical detection of dopamine.* Biosensors and Bioelectronics, 2015. **64**: p. 269-276.

39.   Vinothkannan, M., et al., *One-pot green synthesis of reduced graphene oxide (RGO)/Fe3O4 nanocomposites and its catalytic activity toward methylene blue*

dye degradation. Spectrochimica Acta Part A: Molecular and Biomolecular Spectroscopy, 2015. **136, Part B**: p. 256-264.

40. Wang, H., et al., *Facile synthesis of polypyrrole decorated reduced graphene oxide–Fe3O4 magnetic composites and its application for the Cr(VI) removal.* Chemical Engineering Journal, 2015. **262**: p. 597-606.

41. Li, W., et al., *One-pot route to synthesize SnO2-Reduced graphene oxide composites and their enhanced electrochemical performance as anodes in lithium-ion batteries.* Journal of Power Sources, 2015. **293**: p. 1024-1031.

42. Righini, G.C. and A. Chiappini, *Glass optical waveguides: a review of fabrication techniques.* Optical Engineering, 2014. **53**: p. 071819.

43. Lu, X., et al., *Low-temperature selective catalytic reduction of NOX with NH3 over cerium and manganese oxides supported on TiO2–graphene.* Chemical Engineering Journal, 2015. **260**: p. 776-784.

44. Morais, A., et al., *Enhanced photovoltaic performance of inverted hybrid bulk-heterojunction solar cells using TiO2/reduced graphene oxide films as electron transport layers.* Journal of Photonics for Energy, 2015. **5**(1): p. 057408-057408.

45. Fu, C., et al., *Scalable synthesis and superior performance of TiO2-reduced graphene oxide composite anode for sodium-ion batteries.* Ionics, 2016. **22**(4): p. 555-562.

46. Zou, L., et al., *Synergistic effect of titanium dioxide nanocrystal/reduced graphene oxide hybrid on enhancement of microbial electrocatalysis.* Journal of Power Sources, 2015. **276**: p. 208-214.

47. Lin, W.-D., et al., *Humidity sensing properties of novel graphene/TiO2 composites by sol–gel process.* Sensors and Actuators B: Chemical, 2015. **209**: p. 555-561.

48. Bu, I.Y.Y. and R. Huang, *One-pot synthesis of ZnO/reduced graphene oxide nanocomposite for supercapacitor applications.* Materials Science in Semiconductor Processing, 2015. **31**: p. 131-138.

49. He, H.Y., *Photoinduced superhydrophilicity and high photocatalytic activity of ZnO–reduced graphene oxide nanocomposite films for self-cleaning applications.* Materials Science in Semiconductor Processing, 2015. **31**: p. 200-208.

50. Gollu, S.R., et al., *Incorporation of silver and gold nanostructures for performance improvement in P3HT: PCBM inverted solar cell with rGO/ZnO nanocomposite as an electron transport layer.* Organic Electronics, 2016. **29**: p. 79-87.

51. Guo, L., et al., *Three-dimensional Fe3O4-graphene macroscopic composites for arsenic and arsenate removal.* Journal of Hazardous Materials, 2015. **298**: p. 28-35.

52. Wang, Z. and C.-J. Liu, *Preparation and application of iron oxide/graphene based composites for electrochemical energy storage and energy conversion devices: Current status and perspective.* Nano Energy, 2015. **11**: p. 277-293.

53. Azarang, M., et al., *One-pot sol-gel synthesis of reduced graphene oxide uniformly decorated zinc oxide nanoparticles in starch environment for highly efficient photodegradation of Methylene Blue.* RSC Advances, 2015. **5**(28): p. 21888-21896.

54. Halder, A., M. Zhang, and Q. Chi, *Electrocatalytic Applications of Graphene–Metal Oxide Nanohybrid Materials*, in *Advanced Catalytic Materials: Photocatalysis and Other Current Trends*, L.E. Norena and J.-A. Wang, Editors. 2016, InTech Open Access Publishers. p. 379-414.

55. Halder, A., M. Zhang, and Q. Chi, *Graphene-Metal Oxide Hybrid Nanostructured Materials for Electrocatalytic Sensing and Sustainable Energy Storage.* Reviews in Advanced Sciences and Engineering, 2016. **5**(1): p. 4-31.

56. Wu, H., et al., *Facile hydrothermal synthesis of TiO2 nanospindles-reduced graphene oxide composite with a enhanced photocatalytic activity.* Journal of Alloys and Compounds, 2015. **623**: p. 298-303.

57. Liu, C., et al., *Hydrothermal synthesis of N-doped TiO2 nanowires and N-doped graphene heterostructures with enhanced photocatalytic properties.* Journal of Alloys and Compounds, 2016. **656**: p. 24-32.

58. Li, W., X. Liu, and H. Li, *Hydrothermal synthesis of graphene/Fe3+-doped TiO2 nanowire composites with highly enhanced photocatalytic activity under visible light irradiation.* Journal of Materials Chemistry A, 2015. **3**(29): p. 15214-15224.

59. Wang, A., et al., *Facile hydrothermal synthesis and optical limiting properties of TiO2-reduced graphene oxide nanocomposites.* Carbon, 2015. **89**: p. 130-141.

60. Zhang, W., et al., *Hydrothermal synthesis and photoelectrochemical performance enhancement of TiO2/graphene composite in photo-generated cathodic protection.* Applied Surface Science, 2016. **382**: p. 128-134.

61. Luo, L., et al., *Hydrothermal synthesis of fluorinated anatase TiO2/reduced graphene oxide nanocomposites and their photocatalytic degradation of bisphenol A.* Applied Surface Science, 2015. **353**: p. 469-479.

62. Aleksandrzak, M., et al., *Effect of graphene thickness on photocatalytic activity of TiO2-graphene nanocomposites.* Applied Surface Science, 2015. **331**: p. 193-199.

63. Tao, H., et al., *Enhanced photoactivity of graphene/titanium dioxide nanotubes for removal of Acetaminophen.* Applied Surface Science, 2015. **324**(0): p. 258-264.

64. Calza, P., et al., *Photocatalytic transformation of the antipsychotic drug risperidone in aqueous media on reduced graphene oxide—TiO2 composites.* Applied Catalysis B: Environmental, 2016. **183**: p. 96-106.

65. Kumar, R., et al., *Hydrothermal synthesis of a uniformly dispersed hybrid graphene-TiO2 nanostructure for optical and enhanced electrochemical applications.* RSC Advances, 2015. **5**(10): p. 7112-7120.

66. Rong, X., et al., *Preparation, characterization and photocatalytic application of TiO2—graphene photocatalyst under visible light irradiation.* Ceramics International, 2015. **41**(2, Part A): p. 2502-2511.

67. Zhen, M., et al., *TiO2-B nanorods on reduced graphene oxide as anode materials for Li ion batteries.* Chemical Communications, 2015. **51**(3): p. 507-510.

68. Zhao, F., et al., *A three-dimensional graphene-TiO2 nanotube nanocomposite with exceptional photocatalytic activity for dye degradation.* Applied Surface Science, 2015. **351**: p. 303-308.

69. Xiu, Z., et al., *Graphene-bonded and -encapsulated mesoporous TiO2 microspheres as a high-performance anode material for lithium ion batteries.* Journal of Power Sources, 2015. **287**: p. 334-340.

70. Sun, M., et al., *One-step in situ synthesis of graphene—TiO2 nanorod hybrid composites with enhanced photocatalytic activity.* Materials Research Bulletin, 2015. **61**: p. 280-286.

71.   Zhen, M., et al., *Synthesis of Mesoporous Wall-Structured TiO2 on Reduced Graphene Oxide Nanosheets with High Rate Performance for Lithium-Ion Batteries.* Chemistry – A European Journal, 2015. **21**(14): p. 5317-5322.

72.   Roso, M., et al., *Graphene/TiO2 based photo-catalysts on nanostructured membranes as a potential active filter media for methanol gas-phase degradation.* Applied Catalysis B: Environmental, 2015. **176–177**: p. 225-232.

73.   Han, W., et al., *Graphene-supported flocculent-like TiO2 nanostructures for enhanced photoelectrochemical activity and photodegradation performance.* Ceramics International, 2015. **41**(6): p. 7471-7477.

74.   Wang, Y., et al., *Synthesis of flower-like TiO2 microsphere/graphene composite for removal of organic dye from water.* Materials & Design, 2016. **99**: p. 378-388.

75.   Cao, M., et al., *Photocatalytic degradation of tetrabromobisphenol A by a magnetically separable graphene–TiO2 composite photocatalyst: Mechanism and intermediates analysis.* Chemical Engineering Journal, 2015. **264**: p. 113-124.

76.   Qu, A., et al., *High quantum yield graphene quantum dots decorated TiO2 nanotubes for enhancing photocatalytic activity.* Applied Surface Science, 2016. **375**: p. 230-241.

77.   Feng, X., et al., *TiO2 loaded on graphene nanosheet as reinforcer and its effect on the thermal behaviors of poly(vinyl chloride) composites.* Chemical Engineering Journal, 2015. **260**: p. 524-531.

78.   Safarpour, M., et al., *Development of a novel high flux and fouling-resistant thin film composite nanofiltration membrane by embedding reduced graphene oxide/TiO2.* Separation and Purification Technology, 2015. **154**: p. 96-107.

79.   Liu, X., et al., *Growing TiO2 nanotubes on graphene nanoplatelets and applying the nanonanocomposite as scaffold of electrochemical tyrosinase biosensor.* Sensors and Actuators B: Chemical, 2015. **209**: p. 328-335.

80.   Xu, S., et al., *Preparation of ZnO flower/reduced graphene oxide composite with enhanced photocatalytic performance under sunlight.* Ceramics International, 2015. **41**(3, Part A): p. 4007-4013.

81.   Kavitha, M.K., et al., *Hydrothermal synthesis of ZnO decorated reduced graphene oxide: Understanding the mechanism of photocatalysis.* Journal of Environmental Chemical Engineering, 2015. **3**(2): p. 1194-1199.

82.   Li, X., et al., *3D graphene/ZnO nanorods composite networks as supercapacitor electrodes.* Journal of Alloys and Compounds, 2015. **620**: p. 31-37.

83.   Liu, X., J. Sun, and X. Zhang, *Novel 3D graphene aerogel–ZnO composites as efficient detection for NO2 at room temperature.* Sensors and Actuators B: Chemical, 2015. **211**: p. 220-226.

84.   Ding, J., et al., *Hydrothermal synthesis of zinc oxide-reduced graphene oxide nanocomposites for an electrochemical hydrazine sensor.* RSC Advances, 2015. **5**(29): p. 22935-22942.

85.   Chen, Y.-C., et al., *ZnO–graphene composites as practical photocatalysts for gaseous acetaldehyde degradation and electrolytic water oxidation.* Applied Catalysis A: General, 2015. **490**: p. 1-9.

86.   Zhang, L., et al., *ZnO-reduced graphene oxide nanocomposites as efficient photocatalysts for photocatalytic reduction of CO2.* Ceramics International, 2015. **41**(5, Part A): p. 6256-6262.

87.   Cai, R., et al., *3D graphene/ZnO composite with enhanced photocatalytic activity.* Materials & Design, 2016. **90**: p. 839-844.

88.   Men, X., et al., *Three-dimensional free-standing ZnO/graphene composite foam for photocurrent generation and photocatalytic activity.* Applied Catalysis B: Environmental, 2016. **187**: p. 367-374.

89.   Ge, C., et al., *Synthesis of a ZnO nanorod/CVD graphene composite for simultaneous sensing of dihydroxybenzene isomers.* Carbon, 2015. **95**: p. 1-9.

90.   Song, N., H. Fan, and H. Tian, *Reduced graphene oxide/ZnO nanohybrids: Metallic Zn powder induced one-step synthesis for enhanced photocurrent and photocatalytic response.* Applied Surface Science, 2015. **353**: p. 580-587.

91.   Fu, L., et al., *An Electrochemical Sensor Based on Reduced Graphene Oxide and ZnO Nanorods-Modified Glassy Carbon Electrode for Uric Acid Detection.* Arabian Journal for Science and Engineering, 2016. **41**(1): p. 135-141.

92.   Li, Z., et al., *A novel sensor for determination of dopamine in meat based on ZnO-decorated reduced graphene oxide composites.* Innovative Food Science & Emerging Technologies, 2015. **31**: p. 196-203.

93.   Cao, P., et al., *Facile hydrothermal synthesis of mesoporous nickel oxide/reduced graphene oxide composites for high performance electrochemical supercapacitor.* Electrochimica Acta, 2015. **157**: p. 359-368.

94.   Lu, P., et al., *Synthesis and characterization of nickel oxide hollow spheres–reduced graphene oxide–nafion composite and its biosensing for glucose.* Sensors and Actuators B: Chemical, 2015. **208**(0): p. 90-98.

95.   Rong, X., et al., *A facile hydrothermal synthesis, adsorption kinetics and isotherms to Congo Red azo-dye from aqueous solution of NiO/graphene nanosheets adsorbent.* Journal of Industrial and Engineering Chemistry, 2015. **26**: p. 354-363.

96.   Deng, P., et al., *Facile fabrication of graphene/nickel oxide composite with superior supercapacitance performance by using alcohols-reduced graphene as substrate.* Journal of Alloys and Compounds, 2015. **644**: p. 165-171.

97.   Guo, W.-H., et al., *Free-standing porous Manganese dioxide/graphene composite films for high performance supercapacitors.* Journal of Colloid and Interface Science, 2015. **437**: p. 304-310.

98.   Guo, M.-X., et al., *Hydrothermal synthesis and electrochemical performance of MnO2/graphene/polyester composite electrode materials for flexible supercapacitors.* Electrochimica Acta, 2016. **209**: p. 486-497.

99.   Wang, Y., et al., *A facile hydrothermal synthesis of MnO2 nanorod-reduced graphene oxide nanocomposites possessing excellent microwave absorption properties.* RSC Advances, 2015. **5**(108): p. 88979-88988.

100.   Sun, S., et al., *Fabrication of MnO2/nanoporous 3D graphene for supercapacitor electrodes.* Materials Letters, 2015. **145**: p. 141-144.

101.   Liu, Y., et al., *Layered-MnO2 Nanosheet Grown on Nitrogen-Doped Graphene Template as a Composite Cathode for Flexible Solid-State Asymmetric Supercapacitor.* ACS Applied Materials & Interfaces, 2016. **8**(8): p. 5251-5260.

102.   Wang, Y., et al., *2D/2D nano-hybrids of γ-MnO2 on reduced graphene oxide for catalytic ozonation and coupling peroxymonosulfate activation.* Journal of Hazardous Materials, 2016. **301**: p. 56-64.

103.   Mei, J. and L. Zhang, *Anchoring High-dispersed MnO2 Nanowires on Nitrogen Doped Graphene as Electrode Materials for Supercapacitors.* Electrochimica Acta, 2015. **173**: p. 338-344.

104.   Liu, Y., et al., *An amperometric glucose biosensor based on a MnO2/graphene composite modified electrode.* RSC Advances, 2016. **6**(22): p. 18654-18661.

105. Feng, X., et al., *MnO2/Graphene Nanocomposites for Nonenzymatic Electrochemical Detection of Hydrogen Peroxide.* Electroanalysis, 2015. **27**(2): p. 353-359.

106. Wu, Z.-L., et al., *MnO2/reduced graphene oxide nanoribbons: Facile hydrothermal preparation and their application in amperometric detection of hydrogen peroxide.* Sensors and Actuators B: Chemical, 2017. **239**: p. 544-552.

107. Ren, S., et al., *Hydrothermal synthesis of Fe2O3/polypyrrole/graphene oxide composites as highly efficient electrocatalysts for oxygen reduction reaction in alkaline electrolyte.* Electrochimica Acta, 2015. **178**: p. 179-189.

108. Yu, Z., et al., *Hydrothermal synthesis of Fe2O3/graphene nanocomposite for selective determination of ascorbic acid in the presence of uric acid.* Electrochimica Acta, 2015. **158**: p. 264-270.

109. Song, Z., et al., *Nano-iron oxide (Fe2O3)/three-dimensional graphene aerogel composite as supercapacitor electrode materials with extremely wide working potential window.* Materials Letters, 2015. **145**: p. 44-47.

110. Li, X., et al., *A bottom-up synthesis of [small alpha]-Fe2O3 nanoaggregates and their composites with graphene as high performance anodes in lithium-ion batteries.* Journal of Materials Chemistry A, 2015. **3**(5): p. 2158-2165.

111. Liu, H.D., et al., *Easy one-step hydrothermal synthesis of nitrogen-doped reduced graphene oxide/iron oxide hybrid as efficient supercapacitor material.* Journal of Solid State Electrochemistry, 2015. **19**(1): p. 135-144.

112. Gao, Y., et al., *One-step solvothermal synthesis of quasi-hexagonal Fe2O3 nanoplates/graphene composite as high performance electrode material for supercapacitor.* Electrochimica Acta, 2016. **191**: p. 275-283.

113. Wang, T., et al., *Synthesis of graphene/[small alpha]-Fe2O3 composites with excellent electromagnetic wave absorption properties.* RSC Advances, 2015. **5**(74): p. 60114-60120.

114. Zhang, H., et al., *Solvothermally induced [small alpha]-Fe2O3/graphene nanocomposites with ultrahigh capacitance and excellent rate capability for supercapacitors.* Journal of Materials Chemistry A, 2015. **3**(44): p. 22005-22011.

115. Quan, H., et al., *One-pot synthesis of α-Fe2O3 nanoplates-reduced graphene oxide composites for supercapacitor application.* Chemical Engineering Journal, 2016. **286**: p. 165-173.

116. Song, Z., et al., *Preparation and electrochemical properties of Fe2O3/reduced graphene oxide aerogel (Fe2O3/rGOA) composites for supercapacitors.* Journal of Alloys and Compounds, 2016. **685**: p. 355-363.

117. Zhang, D., et al., *Room-temperature high-performance acetone gas sensor based on hydrothermal synthesized SnO2-reduced graphene oxide hybrid composite.* RSC Advances, 2015. **5**(4): p. 3016-3022.

118. Zhang, J., et al., *Ultrafine SnO2 nanocrystals anchored graphene composites as anode material for lithium-ion batteries.* Materials Research Bulletin, 2015. **68**: p. 120-125.

119. Zhou, W., et al., *SnO2 nanocrystals anchored on N-doped graphene for high-performance lithium storage.* Chemical Communications, 2015. **51**(17): p. 3660-3662.

120. Sun, J., et al., *Fluorine-Doped SnO2@Graphene Porous Composite for High Capacity Lithium-Ion Batteries.* Chemistry of Materials, 2015. **27**(13): p. 4594-4603.

121. Pei, L., et al., *Ice-templated preparation and sodium storage of ultrasmall SnO2 nanoparticles embedded in three-dimensional graphene.* Nano Research, 2015. **8**(1): p. 184-192.

122. Zhang, D., J. Liu, and B. Xia, *Nitrogen Dioxide-Sensing Properties at Room Temperatureof Metal Oxide-Modified Graphene Composite via One-Step Hydrothermal Method.* Journal of Electronic Materials, 2016. **45**(8): p. 4324-4330.

123. Xie, X., et al., *A comparative investigation on the effects of nitrogen-doping into graphene on enhancing the electrochemical performance of SnO2/graphene for sodium-ion batteries.* Nanoscale, 2015. **7**(7): p. 3164-3172.

124. Zhang, D., et al., *Characterization of a hybrid composite of SnO2 nanocrystal-decorated reduced graphene oxide for ppm-level ethanol gas sensing application.* RSC Advances, 2015. **5**(24): p. 18666-18672.

125. Zhu, Y.G., et al., *Effects of Graphene Oxide Function Groups on SnO2/Graphene Nanocomposites for Lithium Storage Application.* Electrochimica Acta, 2015. **154**: p. 338-344.

126. Zhang, C., et al., *Electrochemical Sensor Based on Graphene-Supported Tin Oxide Nanoclusters for Nonenzymatic Detection of Hydrogen Peroxide.* Electrochimica Acta, 2016. **210**: p. 181-189.

127. Fu, L., et al., *A Novel Nonenzymatic Hydrogen Peroxide Electrochemical Sensor Based on SnO2-Reduced Graphene Oxide Nanocomposite.* Sensor Letters, 2015. **13**(1): p. 81-84.

128. Nurzulaikha, R., et al., *Graphene/SnO2 nanocomposite-modified electrode for electrochemical detection of dopamine.* Sensing and Bio-Sensing Research, 2015. **5**: p. 42-49.

129. Ren, Y., et al., *One step hydrothermal synthesis of Mn3O4/graphene composites with great electrochemical properties for lithium-ion batteries.* RSC Advances, 2015. **5**(73): p. 59208-59217.

130. Lee, H.-M., et al., *Direct and environmentally benign synthesis of manganese oxide/graphene composites from graphite for electrochemical capacitors.* Journal of Power Sources, 2015. **281**: p. 44-48.

131. Yang, S., et al., *Synthesis of Mn3O4 nanoparticles/nitrogen-doped graphene hybrid composite for nonenzymatic glucose sensor.* Sensors and Actuators B: Chemical, 2015. **221**: p. 172-178.

132. Dong, Y., et al., *Graphene/acid assisted facile synthesis of structure-tuned Fe3O4 and graphene composites as anode materials for lithium ion batteries.* Carbon, 2015. **86**: p. 310-317.

133. Zhou, S., et al., *Highly Hydrophobic, Compressible, and Magnetic Polystyrene/Fe3O4/Graphene Aerogel Composite for Oil–Water Separation.* Industrial & Engineering Chemistry Research, 2015. **54**(20): p. 5460-5467.

134. Zhu, K., et al., *Hierarchical Fe3O4 microsphere/reduced graphene oxide composites as a capable anode for lithium-ion batteries with remarkable cycling performance.* Journal of Alloys and Compounds, 2016. **675**: p. 399-406.

135. Zhang, W., et al., *Nafion covered core–shell structured Fe3O4@graphene nanospheres modified electrode for highly selective detection of dopamine.* Analytica Chimica Acta, 2015. **853**: p. 285-290.

136. Bagheri, H., et al., *Simultaneous and sensitive determination of melatonin and dopamine with Fe3O4 nanoparticle-decorated reduced graphene oxide modified electrode.* RSC Advances, 2015. **5**(28): p. 21659-21669.

137. Zhang, X., et al., *A novel porous CuO nanorod/rGO composite as a high stability anode material for lithium-ion batteries.* Ceramics International, 2016. **42**(1, Part B): p. 1833-1839.

138. Ezeigwe, E.R., et al., *One-step green synthesis of graphene/ZnO nanocomposites for electrochemical capacitors.* Ceramics International, 2015. **41**(1): p. 715-724.

139. Ezeigwe, E.R., et al., *Solvothermal synthesis of graphene–MnO2 nanocomposites and their electrochemical behavior.* Ceramics International, 2015. **41**(9, Part A): p. 11418-11427.

140. Liu, L., et al., *Superior cycle performance and high reversible capacity of SnO2/graphene composite as an anode material for lithium-ion batteries.* Scientific Reports, 2015. **5**: p. 9055.

141. El-Faham, A., et al., *Microwave irradiation: synthesis and characterization of α-ketoamide and bis (α-ketoamide) derivatives via the ring opening of N-acetylisatin.* Chemistry Central Journal, 2014. **8**(1): p. 27.

142. Sanghi, R., *Microwave irradiation.* Resonance, 2000. **5**(3): p. 77-81.

143. Liu, X., et al., *Fe2O3-reduced graphene oxide composites synthesized via microwave-assisted method for sodium ion batteries.* Electrochimica Acta, 2015. **166**: p. 12-16.

144. She, X., et al., *Microwave-assisted synthesis of Mn3O4 nanoparticles@reduced graphene oxide nanocomposites for high performance supercapacitors.* Materials Research Bulletin, 2015. **70**: p. 945-950.

145. Tian, Y., et al., *CuO nanoparticles on sulfur-doped graphene for nonenzymatic glucose sensing.* Electrochimica Acta, 2015. **156**: p. 244-251.

146. Odedairo, T., et al., *Nanosheets Co3O4 Interleaved with Graphene for Highly Efficient Oxygen Reduction.* ACS Applied Materials & Interfaces, 2015. **7**(38): p. 21373-21380.

147. Taylor, R.F., *Immobilization Methods*, in *Handbook of Chemical and Biological Sensors*, R.R. Taylor and J.S. Schultz, Editors. 1996, IOP Publishing Ltd: Bristol. p. 203-220.

148. Li, Y., et al., *A sandwich-type electrochemical immunosensor based on the biotin- streptavidin-biotin structure for detection of human immunoglobulin G.* Scientific Reports, 2016. **6**: p. 22694.

149. Zhang, W., et al., *Multifunctional glucose biosensors from Fe(3)O(4) nanoparticles modified chitosan/graphene nanocomposites.* Scientific Reports, 2015. **5**: p. 11129.

150. Georgakilas, V., et al., *Noncovalent Functionalization of Graphene and Graphene Oxide for Energy Materials, Biosensing, Catalytic, and Biomedical Applications.* Chemical Reviews, 2016. **116**(9): p. 5464-5519.

151. Zhang, C., et al., *Dual-function amperometric sensors based on poly(diallydimethylammoniun chloride)-functionalized reduced graphene oxide/manganese dioxide/gold nanoparticles nanocomposite.* Sensors and Actuators B: Chemical, 2016. **222**: p. 663-673.

152. Jahanbani, S. and A. Benvidi, *A novel electrochemical DNA biosensor based on a modified magnetic bar carbon paste electrode with Fe3O4NPs-reduced graphene oxide/PANHS nanocomposite.* Materials Science and Engineering: C, 2016. **68**: p. 1-8.

153. Guy, O.J. and K.-A.D. Walker, *Graphene Functionalization for Biosensor Applications*, in *Silicon Carbide Biotechnology: A Biocompatible Semiconductor for Advanced Biomedical Devices and Applications*, S.E. Saddow, Editor. 2016, Elsevier Inc.: Netherlands. p. 85-142.

154. Chen, W., et al., *Recent advances in electrochemical sensing for hydrogen peroxide: a review.* Analyst, 2012. **137**(1): p. 49-58.

155. Dong, S., et al., *High loading MnO2 nanowires on graphene paper: Facile electrochemical synthesis and use as flexible electrode for tracking hydrogen peroxide secretion in live cells.* Analytica Chimica Acta, 2015. **853**: p. 200-206.

156. Pan, Y., et al., *Hierarchical hybrid film of MnO2 nanoparticles/multi-walled fullerene nanotubes–graphene for highly selective sensing of hydrogen peroxide.* Talanta, 2015. **141**: p. 86-91.

157. Zeng, F., et al., *Facile construction of Mn3O4-MnO2 hetero-nanorods/graphene nanocomposite for highly sensitive electrochemical detection of hydrogen peroxide.* Electrochimica Acta, 2016. **196**: p. 587-596.

158. Low, S.S., et al., *One Step Green Preparation of Graphene/ZnO Nanocomposite for Electrochemical Sensing.* Journal of Nanoscience and Nanotechnology, 2016. **16**: p. 1-7.

159. Low, S.S., et al., *Facile hydrothermal growth graphene/ZnO nanocomposite for development of enhanced biosensor.* Analytica Chimica Acta, 2016. **903**: p. 131-141.

160. Karimi, M.A., et al., *A novel rapid synthesis of Fe2O3/graphene nanocomposite using ferrate(VI) and its application as a new kind of nanocomposite modified electrode as electrochemical sensor.* Materials Research Bulletin, 2015. **70**: p. 856-864.

161. Sharma, V. and S.M. Mobin, *Cytocompatible peroxidase mimic CuO:graphene nanosphere composite as colorimetric dual sensor for hydrogen peroxide and cholesterol with its logic gate implementation.* Sensors and Actuators B: Chemical, 2017. **240**: p. 338-348.

162. Moozarm Nia, P., et al., *Electrodeposition of copper oxide/polypyrrole/reduced graphene oxide as a nonenzymatic glucose biosensor.* Sensors and Actuators B: Chemical, 2015. **209**: p. 100-108.

163. Zhao, Y., X. Bo, and L. Guo, *Highly exposed copper oxide supported on three-dimensional porous reduced graphene oxide for non-enzymatic detection of glucose.* Electrochimica Acta, 2015. **176**: p. 1272-1279.

164. Muralikrishna, S., et al., *Non-Enzymatic Amperometric Determination of Glucose by CuO Nanobelt Graphene Composite Modified Glassy Carbon Electrode.* Journal of the Brazilian Chemical Society, 2015. **26**: p. 1632-1641.

165. Yan, X., et al., *Size-controlled synthesis of Cu2O nanoparticles on reduced graphene oxide sheets and their application as non-enzymatic glucose sensor materials.* Journal of Solid State Electrochemistry, 2015. **19**(10): p. 3195-3199.

166. Li, Z., et al., *A glassy carbon electrode modified with a composite consisting of reduced graphene oxide, zinc oxide and silver nanoparticles in a chitosan matrix for studying the direct electron transfer of glucose oxidase and for enzymatic sensing of glucose.* Microchimica Acta, 2016. **183**(5): p. 1625-1632.

167. Jang, H.D., et al., *Synthesis of 3D Silver-Graphene-Titanium Dioxide Composite via Aerosol Spray Pyrolysis for Sensitive Glucose Biosensor.* Aerosol Science and Technology, 2015. **49**(7): p. 538-546.

168. Xie, Y.-L., et al., *Facile ultrasonic synthesis of graphene/SnO2 nanocomposite and its application to the simultaneous electrochemical determination of dopamine, ascorbic acid, and uric acid.* Journal of Electroanalytical Chemistry, 2015. **749**: p. 26-30.

169. Ma, H.-F., et al., *Electrochemical determination of dopamine using octahedral SnO2 nanocrystals bound to reduced graphene oxide nanosheets.* Microchimica Acta, 2015. **182**(11): p. 2001-2007.

170.   Liu, B., et al., *Electrochemical preparation of nickel and copper oxides-decorated graphene composite for simultaneous determination of dopamine, acetaminophen and tryptophan.* Talanta, 2016. **146**: p. 114-121.

171.   Lavanya, N., et al., *Simultaneous electrochemical determination of epinephrine and uric acid in the presence of ascorbic acid using SnO2/graphene nanocomposite modified glassy carbon electrode.* Sensors and Actuators B: Chemical, 2015. **221**: p. 1412-1422.

172.   Zhang, X., Y.-C. Zhang, and L.-X. Ma, *One-pot facile fabrication of graphene-zinc oxide composite and its enhanced sensitivity for simultaneous electrochemical detection of ascorbic acid, dopamine and uric acid.* Sensors and Actuators B: Chemical, 2016. **227**: p. 488-496.

173.   Kumar, S., et al., *Graphene, carbon nanotubes, zinc oxide and gold as elite nanomaterials for fabrication of biosensors for healthcare.* Biosensors and Bioelectronics, 2015. **70**: p. 498-503.

174.   Yang, T., et al., *Shape-controllable ZnO nanostructures based on synchronously electrochemically reduced graphene oxide and their morphology-dependent electrochemical performance.* Electrochimica Acta, 2015. **182**: p. 1037-1045.

175.   Kuralay, F., et al., *Biosensing applications of titanium dioxide coated graphene modified disposable electrodes.* Talanta, 2016. **160**: p. 325-331.

176.   Ensafi, A.A., et al., *Selective and sensitive furazolidone biosensor based on DNA-modified TiO2-reduced graphene oxide.* Applied Surface Science, 2015. **356**: p. 301-307.

177.   Gao, H., et al., *Electrochemical DNA Biosensor Based on Graphene and TiO2 Nanorods Composite Film for the Detection of Transgenic Soybean Gene Sequence of MON89788.* Electroanalysis, 2012. **24**(12): p. 2283-2290.

178.   Zhang, W., L. Wang, and X. Zheng, *Indicator-free electrochemical genosensing originated from the self-signal of poly-xanthurenic acid enhanced by Fe3O4/reduced graphene oxide.* Journal of Solid State Electrochemistry, 2014. **18**(9): p. 2367-2373.

179.   Chen, M., et al., *A sensitive electrochemical DNA biosensor based on three-dimensional nitrogen-doped graphene and Fe3O4 nanoparticles.* Sensors and Actuators B: Chemical, 2017. **239**: p. 421-429.

180.   Prasannakumar, S., et al., *Non-enzymatic Reduction of Hydrogen Peroxide Sensor Based on (Polyaniline-polystyrene Sulphonate) - Carboxylated Graphene Modified Graphite Electrode.* Portugaliae Electrochemica Acta, 2012. **30**(6): p. 371-383.

181.   Maji, S.K., et al., *Immobilizing Gold Nanoparticles in Mesoporous Silica Covered Reduced Graphene Oxide: A Hybrid Material for Cancer Cell Detection through Hydrogen Peroxide Sensing.* ACS Applied Materials & Interfaces, 2014. **6**(16): p. 13648-13656.

182.   Mori, I., et al., *Selective and sensitive fluorometric determinations of cobalt(II) and hydrogen peroxide with fluorescein-hydrazide.* Talanta, 1998. **47**(3): p. 631-637.

183.   Belousov, V.V., et al., *Genetically encoded fluorescent indicator for intracellular hydrogen peroxide.* Nat Meth, 2006. **3**(4): p. 281-286.

184.   Xie, L., Y. Xu, and X. Cao, *Hydrogen peroxide biosensor based on hemoglobin immobilized at graphene, flower-like zinc oxide, and gold nanoparticles nanocomposite modified glassy carbon electrode.* Colloids and Surfaces B: Biointerfaces, 2013. **107**: p. 245-250.

185. Lei, W., et al., *Detection of Hydrogen Peroxide in River Water via a Microplate Luminescence Assay with Time-Resolved ("Gated") Detection.* Microchimica Acta, 2003. **143**(4): p. 269-274.

186. Matsubara, C., N. Kawamoto, and K. Takamura, *Oxo[5,10,15,20-tetra(4-pyridyl)porphyrinato]titanium(IV): An Ultra-high Sensitivity Spectrophotometric Reagent for Hydrogen Peroxide.* Analyst, 1992. **117**: p. 1781 - 1784.

187. Klassen, N.V., D. Marchington, and H.C.E. McGowan, *H2O2 Determination by the I3- Method and by KMnO4 Titration.* Analytical Chemistry, 1994. **66**(18): p. 2921-2925.

188. Jia, J., et al., *A Method to Construct a Third-Generation Horseradish Peroxidase Biosensor: Self-Assembling Gold Nanoparticles to Three-Dimensional Sol–Gel Network.* Analytical Chemistry, 2002. **74**(9): p. 2217-2223.

189. Zhou, J., N.S. Xu, and Z.L. Wang, *Dissolving behavior and stability of ZnO wires in biofluids: A study on biodegradability and biocompatibility of ZnO nanostructures.* Advanced Materials, 2006. **18**(18): p. 2432-2435.

190. Yang, Y. and T. Liu, *Fabrication and characterization of graphene oxide/zinc oxide nanorods hybrid.* Applied Surface Science, 2011. **257**(21): p. 8950-8954.

191. Fan, H., et al., *ZnO–graphene composite for photocatalytic degradation of methylene blue dye.* Catalysis Communications, 2012. **29**: p. 29-34.

192. Wu, J., et al., *Solvothermal synthesis and characterization of sandwich-like graphene/ZnO nanocomposites.* Applied Surface Science, 2010. **256**(9): p. 2826-2830.

193. Song, W.-T., et al., *Graphene decorated with ZnO nanocrystals with improved electrochemical properties prepared by a facile In Situ hydrothermal route.* International Journal of Electrochemical Science, 2012. **7**(3): p. 2164-2174.

194. Kavitha, T., et al., *Glucose sensing, photocatalytic and antibacterial properties of graphene–ZnO nanoparticle hybrids.* Carbon, 2012. **50**(8): p. 2994-3000.

195. Palanisamy, S., S.-M. Chen, and R. Sarawathi, *A novel nonenzymatic hydrogen peroxide sensor based on reduced graphene oxide/ZnO composite modified electrode.* Sensors and Actuators B: Chemical, 2012. **166–167**: p. 372-377.

196. Zacharia, R., H. Ulbricht, and T. Hertel, *Interlayer cohesive energy of graphite from thermal desorption of polyaromatic hydrocarbons.* Physical Review B, 2004. **69**(15): p. 155406\1-155406\7.

197. Chen, W. and L. Yan, *Preparation of graphene by a low-temperature thermal reduction at atmosphere pressure.* Nanoscale, 2010. **2**(4): p. 559-563.

198. Chia, J.S.Y., et al., *A novel one step synthesis of graphene via sonochemical-assisted solvent exfoliation approach for electrochemical sensing application.* Chemical Engineering Journal, 2014. **249**: p. 270-278.

199. Chan, Y.Y., et al., *Enzyme-linked amperometric electrochemical genosensor assay for the detection of PCR amplicons on a streptavidin-treated screen-printed carbon electrode.* Analytical Chemistry, 2008. **80**(8): p. 2774-2779.

200. Yang, S., et al., *Graphene-Based Nanosheets with a Sandwich Structure.* Angewandte Chemie International Edition, 2010. **49**(28): p. 4795-4799.

201. Gayathri, S., et al., *Synthesis of ZnO decorated graphene nanocomposite for enhanced photocatalytic properties.* Journal of Applied Physics, 2014. **115**(17): p. 173504.

202. Ishikawa, Y., N. Aoki, and H. Ohshima, *Colloidal stability of aqueous polymeric dispersions: Effect of water insoluble excipients.* Colloids and Surfaces B: Biointerfaces, 2005. **45**(1): p. 35-41.

203.   Meyer, J.C., et al., *The structure of suspended graphene sheets.* Nature, 2007. **446**(7131): p. 60-63.

204.   Cui, X., et al., *Liquid-phase exfoliation, functionalization and applications of graphene.* Nanoscale, 2011. **3**(5): p. 2118-2126.

205.   Yi, M., et al., *A mixed-solvent strategy for facile and green preparation of graphene by liquid-phase exfoliation of graphite.* Journal of Nanoparticle Research, 2012. **14**(8): p. 1-9.

206.   Hansen, C.M., *Hansen Solubility Parameters: A User's Handbook*. 2nd ed. 2007, FL, USA: CRC Press.

207.   Florescu, M. and C.M. A. Brett, *Development and evaluation of electrochemical glucose enzyme biosensors based on carbon film electrodes.* Talanta, 2005. **65**(2): p. 306-312.

208.   Ting, S.W., et al., *Direct electrochemistry of catalase immobilized at electrochemically reduced graphene oxide modified electrode for amperometric H2O2 biosensor.* International Journal of Electrochemical Science, 2011. **6**(10): p. 4438-4453.

209.   Bu, I.Y.Y., *Highly conductive and transparent reduced graphene oxide/aluminium doped zinc oxide nanocomposite for the next generation solar cell applications.* Optical Materials, 2013. **36**(2): p. 299-303.

210.   Lu, T., et al., *Electrochemical behaviors of graphene–ZnO and graphene–SnO2 composite films for supercapacitors.* Electrochimica Acta, 2010. **55**(13): p. 4170-4173.

211.   Wu, C., et al., *A novel chemical route to prepare ZnO nanoparticles.* Materials Letters, 2006. **60**(15): p. 1828-1832.

212.   Li, W.-J., et al., *Growth mechanism and growth habit of oxide crystals.* Journal of Crystal Growth, 1999. **203**(1–2): p. 186-196.

213.   Ferrari, A.C. and D.M. Basko, *Raman spectroscopy as a versatile tool for studying the properties of graphene.* Nat. Nano., 2013. **8**(4): p. 235-246.

214.   Zeng, H., et al., *Synthesis, optical and electrochemical properties of ZnO nanowires/graphene oxide heterostructures.* Nanoscale Research Letters, 2013. **8**(1): p. 133.

215.   Cuscó, R., et al., *Temperature dependence of Raman scattering in ZnO* Physical Review B, 2007. **75**(16): p. 165202.

216.   Song, M.-J., S. Hwang, and D. Whang, *Amperometric hydrogen peroxide biosensor based on a modified gold electrode with silver nanowires.* Journal of Applied Electrochemistry, 2010. **40**(12): p. 2099-2105.

217.   Anjalidevi, C., V. Dharuman, and J. Shankara Narayanan, *Non enzymatic hydrogen peroxide detection at ruthenium oxide–gold nano particle–Nafion modified electrode.* Sensors and Actuators B: Chemical, 2013. **182**(0): p. 256-263.

218.   Bard, A.J. and L.R. Faulkner, *Potential Sweep Methods*, in *Electrochemical Methods: Fundamentals and Applications*. 2001, John Wiley & Sons, Inc.: New York. p. 226-232.

219.   He, X., et al., *Building Ag nanoparticle 3D catalyst via Na2Ti3O7 nanowires for the detection of hydrogen peroxide.* Sensors and Actuators B: Chemical, 2010. **144**(1): p. 289-294.

220.   Wang, L. and E. Wang, *A novel hydrogen peroxide sensor based on horseradish peroxidase immobilized on colloidal Au modified ITO electrode.* Electrochemistry Communications, 2004. **6**(2): p. 225-229.

221.   Liu, M., R. Liu, and W. Chen, *Graphene wrapped Cu2O nanocubes: Non-enzymatic electrochemical sensors for the detection of glucose and hydrogen*

peroxide with enhanced stability. Biosensors and Bioelectronics, 2013. **45**: p. 206-212.

222. Evans, S.A.G., et al., *Detection of Hydrogen Peroxide at Mesoporous Platinum Microelectrodes.* Analytical Chemistry, 2002. **74**(6): p. 1322-1326.

223. Shrestha, S.S., et al., *Estimating the Burden of 2009 Pandemic Influenza A (H1N1) in the United States (April 2009–April 2010).* Clinical Infectious Diseases, 2011. **52**(suppl 1): p. S75-S82.

224. Krejcova, L., et al., *Electrochemical sensors and biosensors for Influenza detection.* International Journal of Electrochemical Science, 2012. **7**(11): p. 10779-10801.

225. (WHO), W.H.O., *Cumulative number of confirmed human cases for avian influenza A (H5N1) reported to WHO, 2003-2015*. 2015.

226. Gao, R., et al., *Human infection with a novel Avian-origin Influenza A (H7N9) virus.* New England Journal of Medicine, 2013. **368**(20): p. 1888-1897.

227. Kim, Y.K., et al., *Detection of H3N2 canine influenza virus using a Quartz Crystal Microbalance.* Journal of Virological Methods, 2014. **208**: p. 16-20.

228. Chia, J.S.Y., et al., *A bio-electrochemical sensing platform for glucose based on irreversible, non-covalent pi–pi functionalization of graphene produced via a novel, green synthesis method.* Sensors and Actuators B: Chemical, 2015. **210**(0): p. 558-565.

229. Lei, Y., et al., *Incorporating fluorescent quantum dots into water-soluble polymer.* Journal of Luminescence, 2008. **128**(3): p. 277-281.

230. Everaerts, F., et al., *Biomechanical properties of carbodiimide crosslinked collagen: Influence of the formation of ester crosslinks.* Journal of Biomedical Materials Research Part A, 2008. **85A**(2): p. 547-555.

231. Karachevtsev, V.A., et al., *Noncovalent Interaction of Single-Walled Carbon Nanotubes with 1-Pyrenebutanoic Acid Succinimide Ester and Glucoseoxidase.* Journal of Physical Chemistry C, 2011. **115**: p. 21072-21082.

232. Xu, H., et al., *Multiplex biomarker analysis biosensor for detection of hepatitis B virus.* Bio-Medical Materials and Engineering, 2015. **26**(s1): p. S2091-S2100.

233. Weber, P., et al., *Structural origins of high-affinity biotin binding to streptavidin.* Science, 1989. **243**(4887): p. 85-88.

234. Burry, R.W., *Labels for Antibodies*, in *Immunocytochemistry: A Practical Guide for Biomedical Research*. 2010, Springer Science+Business Media, LLC: New York. p. 55-65.

235. McInnes, J.L.S., R. H., *Preparation and Detection of Nonradioactive Nucleic Acid and Oligonucleotide Probes*, in *Nucleic Acid Probes*, R.H. Symons, Editor. 2000, CRC Press, Inc.: Florida. p. 33 - 81.

236. Randles, J.W. and M.J.B. Rodriguez, *Coconut Cadang-Cadang viroid*, in *Viroids*, A. Hadidi, et al., Editors. 2003, CSIRO Publishing: Victoria. p. 233 - 241.

237. Vadamalai, G., et al., *Variants of Coconut cadang-cadang viroid isolated from an African oil palm (Elaies guineensis Jacq.) in Malaysia.* Arch. Virol., 2006. **151**: p. 1447 - 1456.

238. Vadamalai, G., et al., *Detection of Coconut cadang-cadang viroid sequences in oil and coconut palm by ribonuclease protection assay.* Ann. Appl. Biol., 2009. **154**: p. 117 - 125.

239. Singal, S., et al., *Electroactive graphene-multi-walled carbon nanotube hybrid supported impedimetric immunosensor for the detection of human cardiac troponin-I.* RSC Advances, 2015. **5**(92): p. 74994-75003.

240. Zhang, W., et al., *Conductive architecture of Fe2O3 microspheres/self-doped polyaniline nanofibers on carbon ionic liquid electrode for impedance sensing of DNA hybridization.* Biosensors and Bioelectronics, 2009. **25**(2): p. 428-434.

241. Luo, L.-q., et al., *Label-free electrochemical impedance genosensor based on 1-aminopyrene/graphene hybrids.* Nanoscale, 2013. **5**(13): p. 5833-5840.

242. Wu, P., S.-i. Nakano, and N. Sugimoto, *Temperature dependence of thermodynamic properties for DNA/DNA and RNA/DNA duplex formation.* European Journal of Biochemistry, 2002. **269**(12): p. 2821-2830.

243. Li, A., et al., *Electrochemical impedance detection of DNA hybridization based on dendrimer modified electrode.* Biosensors and Bioelectronics, 2007. **22**(8): p. 1716-1722.

244. Yang, J., et al., *A DNA electrochemical sensor based on nanogold-modified poly-2,6-pyridinedicarboxylic acid film and detection of PAT gene fragment.* Analytical Biochemistry, 2007. **365**(1): p. 24-30.

245. Peng, H.-P., et al., *Label-free electrochemical DNA biosensor for rapid detection of mutidrug resistance gene based on Au nanoparticles/toluidine blue–graphene oxide nanocomposites.* Sensors and Actuators B: Chemical, 2015. **207, Part A**: p. 269-276.

246. Zhang, Y., et al., *A novel graphene-DNA biosensor for selective detection of mercury ions.* Biosensors and Bioelectronics, 2013. **48**: p. 180-187.

247. Tak, M., V. Gupta, and M. Tomar, *A ZnO-CNT nanocomposite based electrochemical DNA biosensor for meningitis detection.* RSC Advances, 2016. **6**(80): p. 76214-76222.

248. Jarczewska, M., Ł. Górski, and E. Malinowska, *Application of DNA aptamers as sensing layers for electrochemical detection of potassium ions.* Sensors and Actuators B: Chemical, 2016. **226**: p. 37-43.

249. Zhang, X., et al., *Application of graphene–pyrenebutyric acid nanocomposite as probe oligonucleotide immobilization platform in a DNA biosensor.* Materials Science and Engineering: C, 2013. **33**(7): p. 3851-3857.

250. Hu, Y., et al., *Decorated graphene sheets for label-free DNA impedance biosensing.* Biomaterials, 2012. **33**(4): p. 1097-1106.

251. Bard, A.J. and L.R. Faulkner, *Introduction and Overview of Electrode Processes*, in *Electrochemical Methods: Fundamentals and Applications*. 2001, John Wiley & Sons, Inc.: New York. p. 1-43.

252. Rusling, J.F. and S.L. Suib, *Characterizing Materials with Cyclic Voltammetry.* Advanced Materials, 1994. **6**(12): p. 922-930.

253. Grosser, D.K., *Cyclic Voltammetry - Simulation and Analysis of Reaction Mechanisms*. 1st ed. 1993, New York: Wiley-VCH. 154.

254. Gouws, S., *Voltammetric Characterization Methods for the PEM Evaluation of Catalysts*, in *Electrolysis*, J.L. Kleperis, Vladimir, Editor. 2012, InTech Open Access Publisher.

255. Evans, D.H., et al., *Cyclic voltammetry.* Journal of Chemical Education, 1983. **60**(4): p. 290.

256. Zhao, F., R.C.T. Slade, and J.R. Varcoe, *Techniques for the study and development of microbial fuel cells: an electrochemical perspective.* Chemical Society Reviews, 2009. **38**(7): p. 1926-1939.

257. Mazloum-Ardakani, M., et al., *Voltammetric Determination of Dopamine at the Surface of TiO2 Nanoparticles Modified Carbon Paste Electrode.* International Journal of Electrochemical Science, 2010. **5**: p. 147-157.

258.   Haddad, P.R. and P.E. Jackson, *Electrochemical Detection (Amperometry, Voltammetry and Coulometry)*, in *Ion Chromatography: Principles and Applications*. 1990, Elsevier Science B.V.: Amsterdam. p. 291-322.

259.   Thomas, F.G. and G. Henze, *Techniques*, in *Introduction to Voltammetric Analysis: Theory and Practice*. 2001, CSIRO Collingwood. p. 126-143.

260.   Wojciechowski, M., et al., *Multichannel Electrochemical Detection System for Quantitative Monitoring of PCR Amplification.* Clinical Chemistry, 1999. **45**(9): p. 1690-1693.

261.   Henkens, R. and C. Bonaventura, *Electrochemical Biosensors for Measurement of Genetic Biomarkers of Cancer*, in *Biosensors and Molecular Technologies for Cancer Diagnostics*, K.E. Herold and A. Rasooly, Editors. 2012, Taylor & Francis Group, LLC: Boca Raton. p. 591-608.

262.   Randviir, E.P. and C.E. Banks, *Electrochemical impedance spectroscopy: an overview of bioanalytical applications.* Analytical Methods, 2013. **5**(5): p. 1098-1115.

263.   Katz, E. and I. Willner, *Probing Biomolecular Interactions at Conductive and Semiconductive Surfaces by Impedance Spectroscopy: Routes to Impedimetric Immunosensors, DNA-Sensors, and Enzyme Biosensors.* Electroanalysis, 2003. **15**(11): p. 913-947.

264.   Lasia, A., *Electrochemical Impedance Spectroscopy and its Applications*. 2014, New York: Springer Science+Business Media.

265.   Moisel, M., M.A.F.L. de Mele, and W.D. Müller, *Biomaterial Interface Investigated by Electrochemical Impedance Spectroscopy.* Advanced Engineering Materials, 2008. **10**(10): p. B33-B46.

266.   Suni, I.I., *Impedance methods for electrochemical sensors using nanomaterials.* TrAC Trends in Analytical Chemistry, 2008. **27**(7): p. 604-611.

267.   Lien, T.T.N., et al., *Development of Label-Free Impedimetric Hcg-Immunosensor Using Screen-Printed Electrode.* J. Biosens. Bioelectron., 2011. **2**(3): p. 2-7.

268.   Wang, J., *Controlled-Potential Techniques*, in *Analytical Electrochemistry*. 2006, John Wiley & Sons, Inc.: New Jersey. p. 67-114.

269.   Monk, P.M.S., *Analysis by Dynamic Measurement, A: Systems under Diffusion Control*, in *Fundamentals of Electro-Analytical Chemistry*. 2001, John Wiley & Sons Ltd: Chichester. p. 131-194.

270.   Compton, R.G. and C.E. Banks, *Voltammetry for Electroanalysis*, in *Understanding Voltammetry*. 2011, Imperial College Press: Danvers. p. 347-366.

271.   Goldstein, J.I., H. Yakowitz, and D.E. Newbury, *Introduction*, in *Practical Scanning Electron Microscopy: Electron and Ion Microprobe Analysis*, J.I. Goldstein and H. Yakowitz, Editors. 1975, Plenum Press: New York. p. 1-19.

272.   Bozzola, J.J. and L.D. Russell, *The Past, Present and Future of Electron Microscopy*, in *Electron Microscopy: Principles and Techniques for Biologists*. 1999, Jones and Bartlett Publishers, Inc.: Massachusetts.

273.   Vernon-Parry, K.D., *Scanning electron microscopy: an introduction.* III-Vs Review, 2000. **13**(4): p. 40-44.

274.   Lyman, C.E., et al., *Basic SEM Imaging*, in *Scanning Electron Microscopy, X-Ray Microanalysis, and Analytical Electron Microscopy - A Laboratory Workbook*. 1990, Plenum Press: New York. p. 3-7.

275.   Krinsley, D.H.P., Kenneth, J.S. Boggs, and N.K. Tovey, *The nature of backscattered scanning electron images*, in *Backscattered Scanning Electron*

Microscopy and Image Analysis of Sediments and Sedimentary Rocks. 1998, Cambridge University Press: Cambridge. p. 4-24.

276. Khursheed, A., *Conventional SEM Design*, in *Scanning Electron Microscope Optics and Spectrometers*. 2011, World Scientific Publishing Co. Pte. Ltd.: Singapore. p. 1-70.

277. Reed, S.J.B., *Instrumentation*, in *Electron Microprobe Analysis and Scanning Electron Microscopy in Geology*. 2005, Cambridge University Press: Cambridge. p. 21-36.

278. Kodigala, S.R., *The Role of Characterization Techniques in the Thin Film Analysis*, in *Thin Film Solar Cells from Earth Abundant Materials: Growth and Characterizaton of $Cu_2ZnSn(SSe)_4$ Thin Films and Their Solar Cells*. 2014, Elsevier Inc.: London. p. 67-140.

279. Vanderlinde, W., *Energy Dispersive X-ray Analysis*, in *Microelectronics Failure Analysis: Desk Reference*, T.E.D.F.A.S.D.R. Committee, Editor. 2004, ASM International: Ohio. p. 628-639.

280. Loehman, R.E., *Energy-Dispersive X-Ray Spectroscopy (EDS)*, in *Characterization of Ceramics*, C.R.E. Brundle, Charles A. Jr., Editor. 2010, Momentum Press, LLC: New York. p. 253 - 288.

281. Haschke, M., *Main Components of X-ray Spectrometers*, in *Laboratory Micro-X-Ray Fluorescence Spectroscopy: Instrumentation and Applications*. 2014, Springer International Publishing Switzerland: New York. p. 19 - 118.

282. Brundle, C.R., C.A. Evans, and S. Wilson, *Electron Beam Instruments*, in *Encyclopedia of Materials Characterization: Surfaces, Interfaces, Thin Films*. 1992, Butterworth-Heinemann: Stoneham. p. 117-192.

283. Reimer, L. and H. Kohl, *Transmission Electron Microscopy: Physics of Image Formation*. 2008, New York: Springer Science + Business Media, LLC.

284. Fultz, B. and J.M. Howe, *The TEM and Its Optics*, in *Transmission Electron Microscopy and Diffractometry of Materials*. 2013, Springer-Verlag Berlin Heidelberg: New York. p. 59-115.

285. Bunaciu, A.A., E.g. Udriştioiu, and H.Y. Aboul-Enein, *X-Ray Diffraction: Instrumentation and Applications.* Critical Reviews in Analytical Chemistry, 2015. **45**(4): p. 289-299.

286. Brundle, C.R., C.A. Evans, and S. Wilson, *Structure Determination by Diffraction and Scattering*, in *Encyclopedia of Materials Characterization: Surfaces, Interfaces, Thin Films*. 1992, Butterworth-Heinemann: Stoneham. p. 193-278.

287. Amer, M.S., *Raman Spectroscopy: the Diagnostic Tool*, in *Raman Spectroscopy, Fullerenes and Nanotechnology*. 2010, RSC Publishing: Cambridge. p. 43-80.

288. Rostron, P., S. Gaber, and D. Gaber, *Raman Spectroscopy, Review.* International Journal of Engineering and Technical Research (IJETR), 2016. **6**(1): p. 50-64.